Path-integral and Coarse-graining Strategies for Complex Molecular Phenomena

Thesis by
Michael Anthony Webb

In Partial Fulfillment of the Requirements for the
degree of
Doctor of Philosophy

CALIFORNIA INSTITUTE OF TECHNOLOGY
Pasadena, California

2016
Defended May 27, 2016

Michael Anthony Webb
ORCID: 0000-0002-7420-4474

To My Parents

ACKNOWLEDGEMENTS

Success in academic research, as in life, is not accomplished alone. Over the course of my graduate career, I have benefitted immensely from the mentorship, friendship, and support of a great number of people, for which I am incredibly grateful.

At the forefront of this list is my advisor, Professor Thomas F. Miller III, to whom I cannot express enough gratitude for all the resources and opportunities he has given me. His encouragement, honesty, and guidance has been invaluable to my growth as a researcher and scientific thinker. Patient, compassionate, brilliant, and enthusiastic–I could not have asked for a better advisor and mentor.

I am also grateful to members of my thesis committee: Professor John Brady, Professor John Eiler, and Professor Zhen-Gang Wang. Since my first year at Caltech, I have learned a great deal through their classes, scientific discussions, and thought-provoking questions. They provide different models of excellence from which I will continue to learn, and their support and advice are among the greatest privileges of Caltech.

My research has also been aided by a number of wonderful collaborators, without whom much of my work would not exist. I thank the entire DMREF team: Professor Thomas Miller, Professor Zhen-Gang Wang, Professor Geoff Coates, Professor Nitash Balsara, Dr. Brett Savoie, Dr. Umi Yamamoto, Dr. Yuki Jung, Danielle Pesko, Ksenia Timachova, and Qi Zheng. I am particularly indebted to my fellow Caltech theory contingent, Brett and Umi, for their tireless effort and depth of knowledge. It was a pleasure to be involved with and learn from such an innovative and collaborative group of people. I also thank Professor John Eiler, Professor Alex Sessions, Adam Subhas, Dr. Alison Piasecki, and Paul Magyar for numerous helpful discussions over the years– as a chemical engineer by training, I never imagined thinking about isotope ratios in hyraxes, and yet I did.

I am also thankful for the friendship and support of the entire Miller group. I feel lucky to have joined the group at a time to see so much success from those who came before me and to watch the growth of those who came after; I am continually impressed by the quality of individuals who come through the door of 132 Noyes. The list grows too long to recount contributions for each of you, but to Bin, Nick, Artur, Jason, Josh, Taylor, Connie, Michiel, Joonho, Mark, Lila, Alex, Brooke, Sebastian, Nandini, Kuba, Frank, Fran, Brett, Eric, Reid, Ralph, Feizhi–thank you

all for everything, from your knowledge to your humor. I needed it.

I thank the entire CCE administrative staff. In particular, I want to highlight Priscilla Boon (without whom the Miller group could not function) and Kathy Bubash for all their administrative knowledge and support. Additionally, I acknowledge members of the Caltech HPC staff–Naveed Near-Ansari, Zailo Leite, and Gary Waters–who answered countless questions and resolved many issues, enabling me to focus more on performing research and less on compiling.

I am grateful to the Resnick Sustainability Institute at Caltech for supporting me as a Resnick fellow. They supported me not only through fellowship but also through promotion of my work, providing numerous unique opportunities, and connecting me to a large group of talented, motivated individuals. Neil Fromer and Heidi Rusina are at the heart of these activities, and I am very appreciative of their efforts.

I thank my friends at Caltech and my fellow ChE class–Carolyn, Cris, Joel, Josh, Mark, Mu, Peter, Ryan, and Renee. You provided both levity and support when needed, and I am proud to have shared so many Saturdays in libraries.

Throughout my life, my family have been an enduring source of love and encouragement; I was never told no or that I could not, and all that I have done and become I owe to their support and ongoing devotion. I am also lucky and thankful to have the support of Harvey, Lori, and Tyler who have done much more than just accept me into their own family.

Finally, I thank my wife, Allison, for your love, understanding, and sacrifice, and for all the little things too. I am forever grateful to continue on this journey with you.

ABSTRACT

Molecular simulation provides a powerful tool for connecting molecular-level processes to physical observables. However, the facility to make those connections relies upon the application and development of theoretical methods that permit appropriate descriptions of the systems or processes to be studied. In this thesis, we utilize molecular simulation to study and predict two phenomena with very different theoretical challenges, beginning with (1) lithium-ion transport behavior in polymers and following with (2) equilibrium isotope effects with relevance to position-specific and clumped isotope studies. In the case of ion transport in polymers, there is motivation to use molecular simulation to provide guidance in polymer electrolyte design, but the length and timescales relevant for ion diffusion in polymers preclude the use of direct molecular dynamics simulation to compute ion diffusivities in more than a handful of candidate systems. In the case of equilibrium isotope effects, the thermodynamic driving forces for isotopic fractionation are often fundamentally quantum mechanical in nature, and the high precision of experimental instruments demands correspondingly accurate theoretical approaches. Herein, we describe respectively coarse-graining and path-integral strategies to address outstanding questions in these two subject areas.

TABLE OF CONTENTS

LIST OF ILLUSTRATIONS

LIST OF TABLES

Chapter 1

INTRODUCTION

> Given for one instant an intelligence which could comprehend all the forces by which nature is animated and the respective situation of the beings who compose it - an intelligence sufficiently vast to submit these data to analysis - it would embrace in the same formula the movements of the greatest bodies of the universe and those of the lightest atoms, nothing would be uncertain and the future, as the past, would be present to its eyes.
>
> ---
>
> *Philosophical Essays on Probability*
> *Pierre-Simon Laplace, 1814*

Over the last few decades, molecular simulation–in its many forms–has become one of the most important tools to understand simple and complex physical phenomena, and its use is now pervasive in all branches of physical sciences and engineering.[1,2] To a large extent, its significance is derived as a computational realization of statistical mechanics. And through the *intelligence* that is modern computation, we are able to connect molecular-level processes to physical observables, predicting static and dynamic system properties from microscopic descriptions and interactions. Of course, in practice, there are many challenges to making these connections that depend on the problem or system of interest. In some cases, the pertinent length and timescales may not be accessible via standard simulation approaches, such as for protein aggregation.[3] In others, there may be strict demands on the requisite accuracy for describing a system, such as for the electronic properties of perovskites for solar cell applications.[4] These and related problems require the ingenuity to apply, develop, and/or combine theoretical methods that make their study practically realizable and useful.

In this thesis, we utilize molecular simulation to study and predict (1) lithium-ion transport behavior in polymers and (2) equilibrium isotope effects with relevance to atmospheric, geochemical, and biological processes. In the first case, the essential questions are how the mechanisms underlying ion transport in polymers affect

ionic conductivity and how this information might be used to design new polymer electrolyte materials. In the second case, the essential questions are how the arrangement of isotopes within a molecule influences their equilibrium abundances in nature and how different theoretical models correctly predict these abundances. Obtaining answers to these questions essentially reduces to using theory and simulation to bridge the gap from microscopic to macroscopic realms. Nevertheless, these clearly represent two problems with challenges that necessitate different theoretical approaches befitting the research objectives. Thus, this thesis is laid out in two parts–each briefly described below.

In Part I, we focus on the application of molecular dynamics simulations and coarse-grained models to study ion transport in polymer electrolytes.

Solid polymer electrolytes (SPEs) are attractive alternatives to liquid electrolytes that are typically used in secondary* lithium-ion batteries. SPEs are largely non-flammable, have good mechanical properties, offer easy processibility, and are adaptable to a variety of form factors.[5–10] The base performance of an SPE is in part controlled by its ionic conductivity, which in turn depends on the diffusivity of lithium ions within the polymer host.[11] However, even state-of-the art SPEs exhibit conductivities (and lithium-ion diffusivities) that are too low for many applications.[12]

The guiding principles behind the studies included in this part are that the design of improved SPEs would be facilitated by (1) a better, general understanding of lithium-ion transport in SPEs and (2) computational tools that enable efficient characterization of ion transport in diverse sets of polymers. Whereas extensive experimental[7,12–26] and theoretical[27–38] characterization has been performed on SPEs based on poly(ethylene oxide) (PEO), little is known regarding the mechanisms of ion transport in other polymer classes, and attempts to design polymers based on heuristic knowledge of PEO have been mostly unsuccessful. Therefore, we emphasize understanding ion transport in polymers other than PEO and developing analysis strategies that do not overly rely on specific mechanistic knowledge of any one polymer.

Our study begins in Chapter 2 with a combined experimental and theoretical investigation of lithium-ion transport mechanisms in a systematic series of polyester-based polymer electrolytes. The trends in conductivity between simulation and experiment agree well but cannot be explained based on canonical interpretations of lithium-ion transport in polymers. We therefore propose a new paradigm for understanding the

*rechargeable

trends in conductivity using the notion of solvation-site connectivity–the degree that solvation sites in the polymer are proximate and accessible–as an essential aspect of ion transport that has been largely neglected in the literature.

In Chapter 3, we demonstrate an experimental manifestation of the effects of solvation-site connectivity using a systematic set of polyethers. After accounting for confounding factors, such as relative differences in the glass-transition temperature, we compute an experimental quantity that strongly correlates with simulation-derived metrics of the solvation-site connectivity. This correlation is shown to hold across various temperatures and salt concentrations, even though the simulation metrics depend only on properties of the neat polymer melt. Based on this correlation, we generate an equation that can be used to predict the conductivity as a function of temperature and concentration for this class of polyethers.

In Chapter 4, we leverage the insights developed from earlier mechanistic studies and analysis to propose a new, general coarse-grained model for ion transport in polymer electrolytes. The model treats ion diffusion in terms of hopping transitions on a fluctuating lattice and utilizes inputs from short-timescale trajectories to obtain system-specific parameters. This chemically specific dynamic bond percolation (CS-DBP) model provides a general framework for characterizing long-timescale diffusivity of ions that also reflects the underlying chemistry of the polymer. We show that the CS-DBP model provides semi-quantitative predictions of lithium-ion diffusivity for a range of polymers at a small fraction of the cost of long-timescale molecular dynamics trajectories, illustrating its potential as a tool for the computational screening of polymer electrolytes.

In Chapter 5, we then provide a brief discussion regarding the application of the CS-DBP model for high-throughput screening of polymer electrolytes. Key challenges are also discussed.

In Part II, we focus on the application of path-integral methods to predict equilibrium enrichment of isotopologues[†] in the context of position-specific and clumped isotope studies.

Stable isotope analyses are used both to characterize materials and to understand environmental, geochemical, astrochemical, or biological processes.[39] Most stable isotope analysis centers on the abundance of heavy isotopes to light isotopes, such as comparing oxygen-18 to oxygen-16 to reconstruct past ocean temperatures,[40]

[†]Molecular species that differ in their isotopic composition and/or arrangement

deuterium to hydrogen to source petroleum hydrocarbons,[41] or carbon-13 to carbon-12 to report on the dietary habits of animals.[42] However, precise measurements on the ordering of isotopes within a molecule are becoming increasingly possible and attractive means to provide direct information or constraints on the origins, sources, and histories of natural materials.[43–54]

Two factors that influence the ordering of isotopes within a molecule, and thus the relative enrichment of isotopologues, are the thermodynamic driving forces for heavy isotopes to occupy particular positions and for multiple heavy isotopes to aggregate to nearby positions within a molecule.[55–57] Theoretical quantification of these effects can aid in understanding the formation of isotopologues and their abundances in nature;[39,55,58–62] theory may also serve very practical roles in establishing absolute reference frames for experimental measurements,[55] confirming laboratory protocols, or identifying new targets for stable isotope analysis. The motivation behind the studies here is that the widely used Urey model[63,64] may become an unreliable or ill-suited complement to experimental efforts as analytical instrumentation improves and more complex systems are studied. In contrast, path-integral methods could provide a rigorous and scalable methodology for stable isotope studies.

We begin in Chapter 6 by explicitly comparing Urey model and path-integral Monte Carlo approaches to computing the enrichment of select isotopologues of CO_2, N_2O, methane, and propane. The path-integral calculations are converged to the same level of precision as the best precisions of analytical instrumentation and provide reliable benchmarks for future studies. In addition, these results show that the Urey-model approaches often rely on a nontrivial cancellation of errors in their computation of equilibrium constants for isotope-exchange reactions, leading to experimentally resolvable errors in apparent equilibrium temperatures of up to 35 K for the isotopologues considered. In contrast, the use of path-integral methods neither relies on any cancellation of errors nor requires any a priori assumptions about the relative importance of effects such as anharmonicity and rovibrational coupling.

In Chapter 7, we employ path-integral calculations to quantify ^{13}C-^{13}C, ^{13}C-D, and D-^{12}C-D clumping effects in five isotope-exchange reactions involving doubly-substituted isotopologues of ethane. The calculations make use of a new, high-quality potential energy surface as well as a recently developed path-integral estimator for isotopic fractionation. These calculations are used to quantify the strength

of isotopic clumping in the various isotopologues. Furthermore, comparison between the path-integral results and those of the Urey model illustrates an ambiguity in the latter when dealing with isotopologues with distinct rotameric states that may obfuscate its application in more complex systems.

References

(1) Tuckerman, M. E., *Statistical Mechanics: Theory and Molecular Simulation (Oxford Graduate Texts)*; Oxford University Press, USA: 2010.

(2) Frenkel, D.; Smit, B., *Understanding molecular simulation : from algorithms to applications*, 2nd ed.; Academic Press: 2002.

(3) Ding, F.; Dokholyan, N. V. *Proc. Natl. Acad. Sci. U.S.A.* **2008**, *105*, 19696–19701.

(4) Umari, P.; Mosconi, E.; De Angelis, F. *Scientific Reports* **2014**, *4*.

(5) Van Gool, W.; Division, N. A. T. O. S. A., *Fast ion transport in solids: Solid state batteries and devices. Proceedings of the NATO sponsored Advanced Study Institute on Fast Ion Transport in Solids, Solid State Batteries and Devices, Belgirate, Italy, 5-15 September 1972*; North Holland Pub. Co.: 1973.

(6) Armand, M. *Solid State Ion.* **1983**, *9–10, Part 2*, 745 –754.

(7) Alloin, F; Sanchez, J. Y.; Armand, M *J. Electrochem. Soc* **1994**, *141*, 1915–1920.

(8) Tarascon, J.; Armand, M *Nature* **2001**, *414*, 359–367.

(9) Meyer, W. H. *Adv. Mater.* **1998**, *10*, 439–448.

(10) Jr., D. T. H.; Balsara, N. P. *Annual Review of Materials Research* **2013**, *43*, 503–525.

(11) Balsara, N. P.; Newman, J. *J. Electrochem. Soc* **2015**, *162*, A2720–A2722.

(12) Buriez, O; Han, Y.; Hou, J; Kerr, J.; Qiao, J; Sloop, S.; Tian, M.; Wang, S. *J. Power Sources* **2000**, *89*, 149–155.

(13) Croce, F.; Appetecchi, G. B.; Persi, L.; Scrosati, B. *Nature* **1998**, *394*, 456–458.

(14) Croce, F; Persi, L; Scrosati, B; Serraino-Fiory, F; Plichta, E; Hendrickson, M. *Electrochim. Acta* **2001**, *46*, 2457 –2461.

(15) Johansson, P.; Ratner, M. A.; Shriver, D. F. *J. Phys. Chem. B* **2001**, *105*, 9016–9021.

(16) Nishimoto, A.; Watanabe, M.; Ikeda, Y.; Kohjiya, S. *Electrochim. Acta* **1998**, *43*, 1177 –1184.

(17) Watanabe, M.; Hirakimoto, T.; Mutoh, S.; Nishimoto, A. *Solid State Ion.* **2002**, *148*, 399 –404.

(18) Matoba, Y.; Ikeda, Y.; Kohjiya, S. *Solid State Ion.* **2002**, *147*, 403 –409.

(19) Khurana, R.; Schaefer, J. L.; Archer, L. A.; Coates, G. W. *J. Am. Chem. Soc.* **2014**, *136*, 7395–7402.

(20) Andrieu, X; Fauvarque, J. F.; Goux, A; Hamaide, T; Mhamdi, R; Vicedo, T *Electrochim. Acta* **1995**, *40*, 2295–2299.

(21) Deng, Y. L.; Ding, J. F.; Y U, G; Mobbs, R. H.; Heatley, F; Price, C; Booth, C *Polymer* **1992**, *33*, 1959–1962.

(22) Florjanczyk, Z; Krawiec, W; Wieczorek, W; Przyluski, J *Angewandte Makromolekulare Chemie* **1991**, *187*, 19–32.

(23) Ikeda, Y; Masui, H; Matoba, Y *J. Appl. Polym. Sci* **2005**, *95*, 178–184.

(24) Schroers, M; Kokil, A; Weder, C *J. Appl. Polym. Sci* **2004**, *93*, 2883–2888.

(25) Wolfenson, A.; Torresi, R.; Bonagamba, T.; DePaoli, M.; Panepucci, H *J. Phys. Chem. B* **1997**, *101*, 3469–3473.

(26) Barteau, K. P.; Wolffs, M.; Lynd, N. A.; Fredrickson, G. H.; Kramer, E. J.; Hawker, C. J. *Macromolecules* **2013**, *46*, 8988–8994.

(27) Müller-Plathe, F; Vangunsteren, W. *J. Chem. Phys.* **1995**, *103*, 4745–4756.

(28) Neyertz, S; Brown, D *J. Chem. Phys.* **1996**, *104*, 3797–3809.

(29) Duan, Y.; Halley, J.; Curtiss, L; Redfern, P *J. Chem. Phys.* **2005**, *122*.

(30) Siqueira, L. J. A.; Ribeiro, M. C. C. *J. Chem. Phys.* **2006**, *125*.

(31) Borodin, O; Smith, G. *Macromolecules* **2006**, *39*, 1620–1629.

(32) Karo, J.; Brandell, D. *Solid State Ion.* **2009**, *180*, 1272–1284.

(33) Wu, H.; Wick, C. D. *Macromolecules* **2010**, *43*, 3502–3510.

(34) Brandell, D.; Priimaegi, P.; Kasemaegi, H.; Aabloo, A. *Electrochim. Acta* **2011**, *57*, 228–236.

(35) Lin, K.-J.; Maranas, J. K. *Phys. Chem. Chem. Phys.* **2013**, *15*, 16143–16151.

(36) Hanson, B.; Pryamitsyn, V.; Ganesan, V. *ACS Macro Lett.* **2013**, *2*, 1001–1005.

(37) Lin, K.-J.; Maranas, J. K. *Phys. Rev. E* **2013**, *88*, 052602.

(38) Mogurampelly, S.; Ganesan, V. *Macromolecules* **2015**, *48*, 2773–2786.

(39) Wolfsberg, M.; Hook, W. A.; Paneth, P.; Rebelo, L. P. N., *Isotope Effects in the Chemical, Geological and Bio Sciences*; Springer Netherlands.

(40) Epstein, S; Buchsbaum, R; Lowenstam, H.; Urey, H. *Geological Society of America Bulletin* **1953**, *64*, 1315–1325.

(41) Schoell, M *Org Geochem.* **1984**, *6*, 645 –663.

(42) DeNiro, M. J.; Epstein, S. *Geochim. Cosmochim. Acta* **1978**, *42*, 495–506.

(43) Eiler, J. M. In *Annual Review of Earth and Planetary Sciences, Vol. 41*, Jeanloz, R, Ed.; Annual Review of Earth and Planetary Sciences, Vol. 41, 2013, 411–441.

(44) Mroz, E. J. *Chemosphere* **1993**, *26*, 45–53.

(45) Conny, J.; Currie, L. *Atmospheric Environment* **1996**, *30*, 621–638.

(46) Eiler, J. M.; Schauble, E *Geochim. Cosmochim. Acta* **2004**, *68*, 4767–4777.

(47) Oba, Y.; Naraoka, H. *Rapid Commun. Mass Spectrom.* **2006**, *20*, 3649–3653.

(48) Mohn, J; Tuzson, B; Manninen, A; Yoshida, N; Toyoda, S; Brand, W. A.; Emmenegger, L *Atmospheric Measurement Techniques* **2012**, *5*, 1601–1609.

(49) Yoshida, N; Vasilev, M; Ghosh, P; Abe, O; Yamada, K; Morimoto, M *Rapid Commun. Mass Spectrom.* **2013**, *27*, 207–215.

(50) Tsuji, K; Teshima, H; Sasada, H; Yoshida, N *Spectrochimica Acta Part A-Molecular and Biomolecular Spectroscopy* **2012**, *98*, 43–46.

(51) Koester, J. R.; Well, R; Tuzson, B; Bol, R; Dittert, K; Giesemann, A; Emmenegger, L; Manninen, A; Cardenas, L; Mohn, J *Rapid Commun. Mass Spectrom.* **2013**, *27*, 216–222.

(52) Eiler, J. M.; Clog, M.; Magyar, P.; Piasecki, A.; Sessions, A.; Stolper, D.; Deerberg, M.; Schlueter, H.-J.; Schwieters, J. *Int. J. Mass spectrom.* **2013**, *335*, 45 –56.

(53) Stolper, D.; Sessions, A.; Ferreira, A.; Neto, E. S.; Schimmelmann, A.; Shusta, S.; Valentine, D.; Eiler, J. *Geochim. Cosmochim. Acta* **2014**, *126*, 169 –191.

(54) Ono, S.; Wang, D. T.; Gruen, D. S.; Lollar, B. S.; Zahniser, M. S.; McManus, B. J.; Nelson, D. D. *Anal. Chem.* **2014**, *86*, 6487–6494.

(55) Wang, Z. G.; Schauble, E. A.; Eiler, J. M. *Geochim. Cosmochim. Acta* **2004**, *68*, 4779–4797.

(56) Eiler, J. M. *Earth. Planet. Sci. Lett.* **2007**, *262*, 309–327.

(57) Eiler, J. M.; Bergquist, B.; Bourg, I.; Cartigny, P.; Farquhar, J.; Gagnon, A.; Guo, W.; Halevy, I.; Hofmann, A.; Larson, T. E.; Levin, N.; Schauble, E. A.; Stolper, D. *Chem. Geol.* **2014**, *372*, 119 –143.

(58) Ma, Q; Wu, S; Tang, Y *Geochim. Cosmochim. Acta* **2008**, *72*, 5446–5456.

(59) Schauble, E. A.; Ghosh, P; Eiler, J. M. *Geochim. Cosmochim. Acta* **2006**, *70*, 2510–2529.

(60) Guo, W.; Mosenfelder, J. L.; Goddard III, W. A.; Eiler, J. M. *Geochim. Cosmochim. Acta* **2009**, *73*, 7203–7225.

(61) Hill, P. S.; Tripati, A. K.; Schauble, E. A. *Geochim. Cosmochim. Acta* **2014**, *125*, 610–652.

(62) Tripati, A. K.; Hill, P. S.; Eagle, R. A.; Mosenfelder, J. L.; Tang, J.; Schauble, E. A.; Eiler, J. M.; Zeebe, R. E.; Uchikawa, J.; Coplen, T. B.; Ries, J. B.; Henry, D. *Geochim. Cosmochim. Acta* **2015**, *166*, 344–371.

(63) Urey, H. *J. Chem. Soc.* **1947**, 562–581.

(64) Bigeleisen, J; Mayer, M. *J. Chem. Phys.* **1947**, *15*, 261–267.

Part I

Ion Transport in Polymer Electrolytes

Chapter 2

SYSTEMATIC COMPUTATIONAL AND EXPERIMENTAL INVESTIGATION OF LITHIUM-ION TRANSPORT MECHANISMS IN POLYESTER-BASED POLYMER ELECTROLYTES

Understanding the mechanisms of lithium-ion transport in polymers is crucial for the rational design of polymer electrolytes. Although lithium-ion transport in poly(ethylene oxide) (PEO) has been extensively studied both experimentally and theoretically, mechanistic knowledge is generally lacking for polymers with other chemistries and architectures.

In this chapter, we combine modular synthesis, electrochemical characterization, and molecular simulation to investigate lithium-ion transport in a new family of polyester-based polymers and in PEO. Theoretical predictions of glass-transition temperatures and ionic conductivities in the polymers agree well with experimental measurements. Interestingly, both the experiments and simulations indicate that the ionic conductivity of PEO, relative to the polyesters, is far higher than would be expected from its relative glass-transition temperature. The simulations reveal that diffusion of the lithium cations in the polyesters proceeds via a different mechanism than in PEO, and analysis of the distribution of available cation solvation sites in the various polymers provides a novel and intuitive way to explain the experimentally observed ionic conductivities. This work provides a platform for the evaluation and prediction of ionic conductivities in polymer electrolyte materials.

The experimental synthesis featured in this chapter was performed by Dr. Yuki Jung under the direction of Prof. Geoffrey W. Coates at Cornell University, and the preparation and characterization of the polymer electrolytes was performed by Ms. Danielle M. Pesko under the direction of Prof. Nitash P. Balsara at the University of California, Berkeley. Data and content in this chapter have been published as M.A. Webb, Y. Jung, D.M. Pesko, U. Yamamoto, G.W. Coates, N.P. Balsara, Z.-G. Wang, T.F. Miller III. “A Systematic Computational and Experimental Investigation of Lithium-ion Transport Mechanisms in Polyester-based Polymer Electrolytes.” *ACS Cent. Sci.*, **1**, 198-205 (2015).

2.1 Introduction

Solvent-free, solid polymeric electrolytes[1] (SPEs) are of interest for the development of safe, stable, and cost-effective battery technologies. Candidate SPEs typically require both a strong coordinating affinity for the conducting cation and also a suitable distance between coordinating centers.[2,3] Consequently, poly(ethylene oxide) (PEO) and PEO-based polymers have been extensively characterized, although ambient temperature ionic conductivities in such polymers are not satisfactory for many practical applications.[4,5]

Significant theoretical evidence suggests that ion transport in polymers is intrinsically coupled to polymer motion.[6–15] In particular, numerous theoretical studies of ion transport in PEO-based SPEs have shown that lithium cations are typically coordinated by four to seven oxygen atoms (from one or two independent chains) and diffuse via three principal mechanisms: inter-chain hopping, intra-chain hopping, and co-diffusion with short polymer chains (<10,000 g/mol). Efforts to improve lithium-ion conductivity in PEO-based polymers have thus mainly focused on disrupting polymer crystallinity and lowering the glass-transition temperature T_g, such as through the use of plasticizing additives;[16–18] cross-linked, comb, or graft polymer architectures;[19–23] incorporation of comonomers into the PEO backbone;[24–31] and polymer blends.[32,33] Despite these efforts, ionic conductivities in state-of-the-art, PEO-based SPEs remain limited at ambient temperatures.[22]

Non-PEO-based polymer architectures provide new opportunities for enhancing ionic conductivity by altering ion-polymer and polymer-polymer interactions and are thus of interest for the design of next-generation SPEs. Ionic conductivity characteristics have been experimentally investigated in several novel polymers that include polyesters, polyphosphazenes, polyamines, polysilanes, polysiloxanes, and polycarbonates.[34–40] However, few theoretical studies on the mechanisms of ion transport in such polymers have been performed, and it is not known to what extent the transport mechanisms present in PEO are shared in other polymer architectures. The design of new SPEs requires an improved understanding of the mechanisms that facilitate lithium-ion transport in polymers and the identification of new polymer architectures that efficiently realize these mechanisms.

Here, experimental synthesis and electrochemical characterization are combined with long-timescale molecular dynamics (MD) simulations to investigate lithium-ion transport in six new SPEs. Figure 2.1 illustrates a schematic overview of this approach. Modular synthesis produces six polyesters that have either of two back-

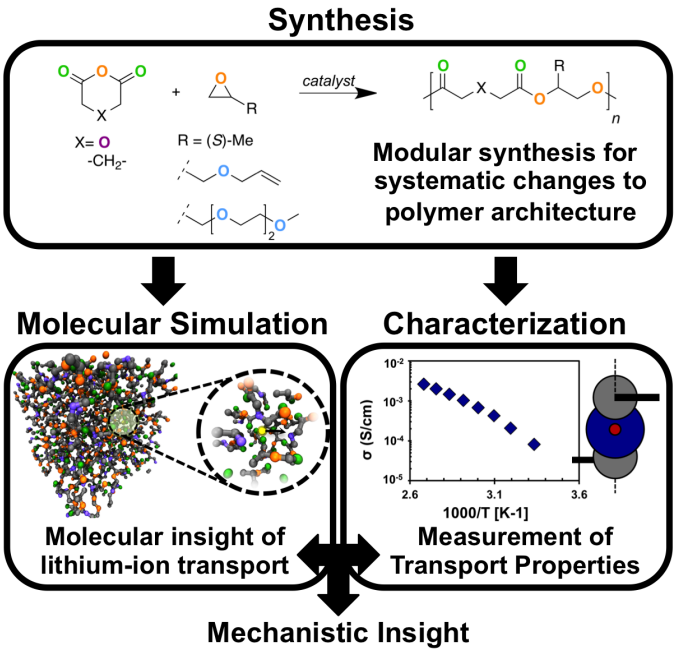

Figure 2.1: A schematic overview of the study.

bone motifs and one of three side chains (Figure 2.1, top). These polymers are then characterized using both simulation and experiment (Figure 2.1, middle), which demonstrates the effect of polymer composition and architecture on ionic conductivity (Figure 2.1, bottom). By comparing experimental observables with the corresponding quantities from simulation, we identify the primary trends regarding polymer architecture and conductivity. Agreement between simulation and experiment then provides a connection between macroscopic properties and molecular-level processes, which enables a detailed theoretical analysis of the molecular processes that give rise to the observed trends. This complementary approach provides a better understanding of ion transport in novel polymer electrolytes than would be obtained from either an independent experimental or theoretical study.

2.2 Polymer Structures

Six aliphatic polyesters with two different backbone motifs and three different side chains are studied (Figure 2.2). The repeat unit for each is an ester with a pendant side chain. For ease of reference, the polymers are indexed by number according to the side chain and by letter according to the backbone motif. Polymers are indexed as type-1 for a methyl side chain, type-2 for an allyl side chain, and type-3 for an ethylene-oxide oligomer ($n = 2$) side chain. The backbone motifs are indexed as type-a for polymers with a methylene between the two carbonyl groups and type-b

for polymers with an oxygen between the two carbonyl groups. Comparison between type-a and type-b polymers probes the effect of adding a binding site for the lithium cation in the backbone. Similarly, comparison of type-1, -2, and -3 polymers probes the effect of including additional binding sites in the side chain.

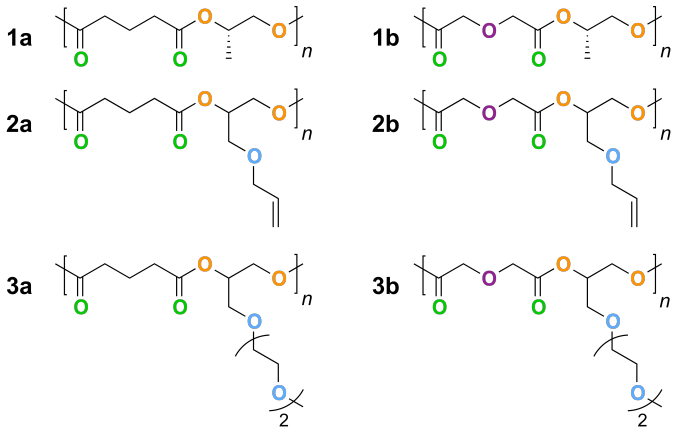

Figure 2.2: Repeat units for polyesters. Oxygen atoms are colored according to type: double-bonded carbonyl oxygens are green, ester oxygens are orange, ether oxygens in the backbone are purple, and ether oxygens in side chains are blue.

2.3 Methods

Table 2.1: Summary of polymer properties.

	Simulation				Experiment		
	M_n (kDa)	[a] N_c	T_g (°C)	[b] r	$\langle M_n \rangle$ (kDa)	PDI	T_g (°C)
1a	2.54	11	35	0.0062	8.8	1.90	−29
1b	2.57	11	47	0.0062	8.0	1.72	12
2a	2.45	12	37	0.0077	10.4	2.00	−44
2b	2.47	12	49	0.0077	8.9	1.45	−15
3a	2.57	11	39	0.0103	4.2	1.30	−48
3b	2.59	11	41	0.0103	6.1	1.77	−26
PEO	2.38	12	2	0.0139	[c] 5	*n/a*	−60

[a] Number of polymer chains

[b] Number of lithium cations per nine polymer backbone atoms

[c] The measurements for T_g and conductivity in PEO employ molecular weights of 4.6 kD and 5.0 kDa, respectively

2.3.a Synthesis

The polyesters are synthesized using the transition metal-catalyzed alternating copolymerization of epoxides and cyclic anhydrides.[41–43] The polyester backbone structure is varied by copolymerizing glutaric anhydride (type-a) or diglycolic an-

hydride (type-b) with *S*-propylene oxide (type-1), allyl glycidyl ether (type-2), or 2-((2-(2-methoxyethoxy) ethoxy) methyl) oxirane (type-3) as shown in Figure 2.1 (top). Table 2.1 provides the number-averaged molecular weight $\langle M_n \rangle$ and polydispersity index (PDI) for each polymer; the polymers in this study exhibit molecular weights that are sufficiently high to expect that variation in $\langle M_n \rangle$ among the considered samples leads to only minor effects on conductivity and T_g.[44,45]

2.3.b Simulation

All MD simulations employ a united-atom force field, with bonding parameters taken from CHARMM[46] and all other parameters taken from the TraPPE-UA force field;[47–50] compatible lithium-ion parameters are obtained from previous simulation studies.[51] All simulations are performed using the LAMMPS simulation package[52] with GPU acceleration.[53,54] The equations of motion are evolved using the velocity-Verlet integrator with a 1 fs timestep. Particle-particle-mesh Ewald summation is used to compute all non-bonded interactions beyond a 14 Å cutoff. The Nosé-Hoover thermostat (100 fs relaxation) is used for all NVT simulations, and the Nosé-Hoover barostat (1000 fs relaxation) is used for all NPT simulations. Results in the dilute-ion limit are obtained from simulations of a single lithium cation diffusing in the polymer.

2.3.c Characterization

For each polymer, T_g measurements of the neat polymer are made using differential scanning calorimetry. Polymer electrolytes are then prepared by mixing neat polymer sample with lithium bis(trifluoromethanesulfonyl) imide (LiTFSI) salt and anhydrous N-methyl-2-pyrrolidone (NMP) in an argon glovebox until dissolution at 90 °C and drying under vacuum at 90 °C to remove excess NMP. Ionic conductivities of the polymer electrolytes are determined from ac impedance spectroscopy.

2.4 Results

2.4.a Ionic Conductivities

Using both simulation and experiment, we examine the ionic conductivities of each polymer in the dilute-ion limit, which minimizes complications associated with ion pairing and aggregation.

Figures 2.3(a-c) present MD simulation results for the mean square-displacement (MSD) of the lithium cation at 363 K. The slopes of the MSDs on a log-log scale are less than unity, indicating that the transport is not yet in the fully diffusive regime

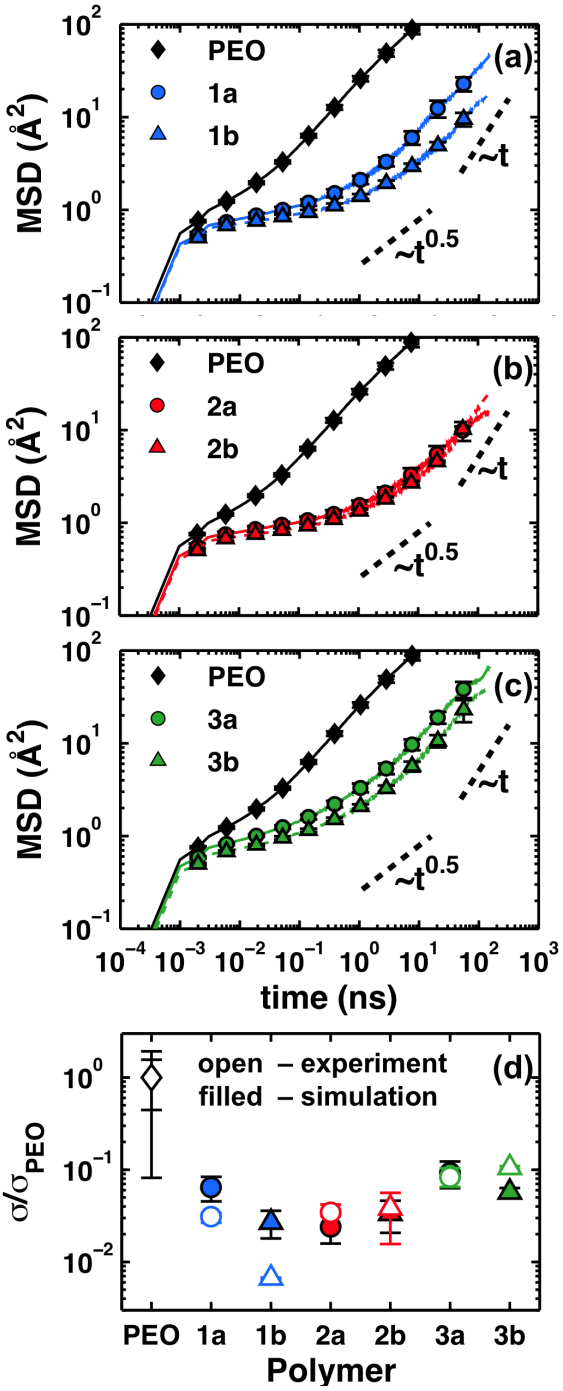

Figure 2.3: Ion transport properties in the dilute-ion limit at 363 K. Lithium-ion mean square-displacement (MSD) from MD simulations in PEO and the (a) type-1 polymers, (b) type-2 polymers, and (c) type-3 polymers. The data for PEO are reproduced in each panel. (d) A comparison of experimental and simulated ionic conductivities; both sets of data are normalized by the corresponding conductivity in PEO. The error bars in (a)-(c) report the standard error of the mean obtained from block-averaging four 500 ns trajectories for each polymer; error bars in (d) report the sample standard deviation.

even after 150 ns. Comparison of polymers 1a and 1b (Figure 2.3a) reveals that lithium-ion diffusion is slowed by the presence of the ether oxygen on the backbone. However, this effect is largely mitigated by the presence of side chains with oxygen atoms, as seen by comparing polymer 2a and 2b (Figure 2.3b), and likewise for polymer 3a and 3b (Figure 2.3c). Comparison of polymer 3a and 1b shows that the differences in polymer architecture considered here at most affect the lithium-ion diffusion by a factor of about 3.75. In contrast, the rate of lithium-ion transport is at least an order-of-magnitude faster in PEO than in any of the polyesters. In particular, the relative span of the sub-diffusive regime, which is the near-plateau region in the MSD plots, reveals that the lithium cation is restricted to its local solvation environment for substantially longer times in the polyesters compared to PEO.

For comparison with experiment, the MSD results in Figure 2.3(a-c) are used to compute approximate lithium-ion conductivities using the Nernst-Einstein equation[55] and the apparent lithium-ion diffusivity[6] evaluated at 150 ns. Figure 2.3d compares these results with experimental dilute ionic conductivities at the same temperature and effective concentration as the simulations (Table 2.1).

Figure 2.3d reveals good agreement between dilute-ion conductivities obtained using experiment and those obtained from MD simulations. This correlation for the relative ordering of conductivities suggests that the lithium-ion dynamics are mechanistically similar between simulation and experiment. However, the dilute-ion conductivities obtained from simulation are systematically lower than the corresponding experimental measurements; for example, the conductivity for PEO obtained from simulation is $(9 \pm 4) \times 10^{-6}$ compared to $(2 \pm 1) \times 10^{-4}$ S/cm. This is possibly due to the fact that the MD conductivity results reflect only contributions from the lithium cation whereas the experimental measurements include both cation and anion contributions; of course, it is also possibly due to inaccuracies of the employed MD force field. Furthermore, the molecular weights of the polymer chains are smaller in the simulations than in the experimental samples, though we do not expect this difference to have a substantial effect on conductivity based on our knowledge of the molecular weight-dependence on polymer electrolyte conductivity.[44,45] Polymer 1b is the only qualitative outlier in the correlation between experimental and simulation results. This is likely due to the fact that polymer 1b is notably more solid in experiment, whereas this is not the case for the MD simulations. Even so, the experimental conductivities are all within a factor of three and an order-of-magnitude

smaller than PEO. Thus, both experimental and simulation results indicate that the effect of varying polymer architecture in the polyesters is somewhat minor compared to the mechanistic advantage that apparently exists for PEO. In the next section, we investigate how differences in T_g affect the conductivity in these polymers.

2.4.b Correlating T_g with Conductivity

Figure 2.4a and Table 2.1 provide both experimental and simulated values of T_g, which is often used as a proxy for the segmental mobility of polymer chains.[2,56] Figure 2.4a illustrates that the experimental and simulation data are qualitatively similar by plotting the data relative to the glass-transition temperature for PEO, $T_{g,PEO}$. Consistently, T_g is lower for type-a polymers relative to type-b polymers, which suggests that adding a polar ether oxygen between the two carbonyls decreases segmental mobility. The experimental data also show a weak but consistent side-chain dependence. Namely, increasing side-chain length (type-1 < type-2 < type-3) leads to a slight reduction in T_g, possibly due to a plasticizing effect by the side chains or simply because the flexible side chains constitute a larger volume fraction of the polymer;[2,22,57] this particular trend is not as evident in the simulated T_g data.

For the experimental data, Figure 2.4b reveals the degree of correlation between ionic conductivity and T_g by plotting the dilute-ion conductivities (on a logarithmic scale) against $1000(T - T_g)^{-1}$. This analysis is similar to a typical Vogel-Fulcher-Tammann ionic conductivity plot,[2,58] except that a range of polymers (and thus a range of T_g) is examined at a fixed temperature rather than the conductivity of a given polymer over a range of temperatures. The dashed line is the linear fit of the data for the polyesters only. Although there is an overall tendency for polymers with lower T_g to have higher ionic conductivities, the correlation is not well-characterized by a single line. In particular, the figure shows strikingly that PEO exhibits anomalously high conductivity among this set of polymers when only the effects associated with changes in T_g (i.e., polymer segmental mobility) are considered. We emphasize that the corresponding analysis performed using the simulation data yields identical conclusions. In the following section, we demonstrate that this apparent anomaly in the conductivity of PEO can be understood if the connectivity of lithium-ion solvation sites is additionally considered.

2.4.c Lithium-ion Coordination Dynamics

Using the results from the MD simulations, we now investigate the mechanistic features of lithium-ion solvation and diffusion in the various polymer electrolytes to

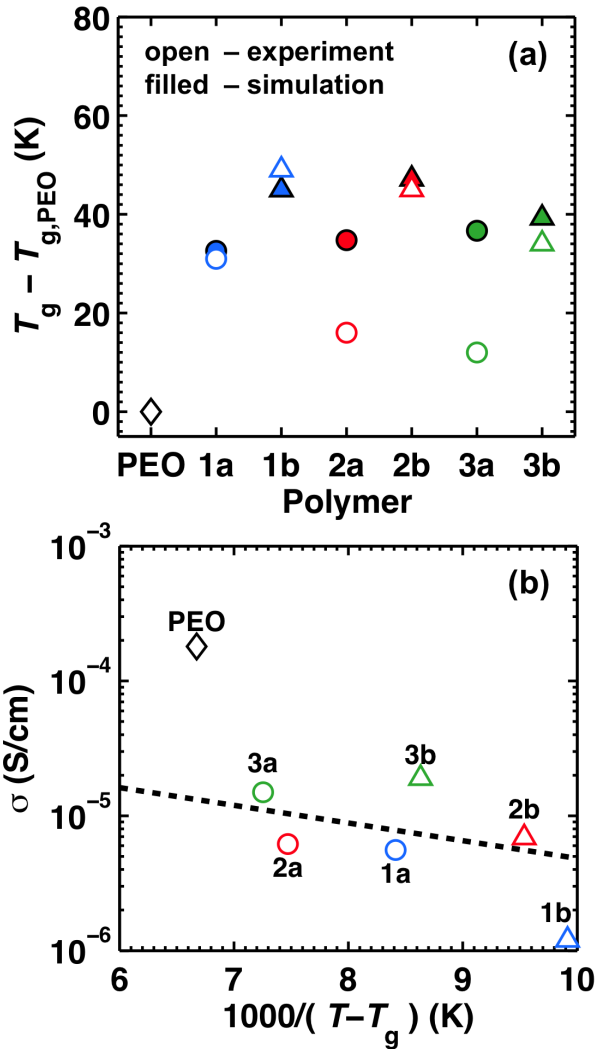

Figure 2.4: (a) T_g obtained via experiment using DSC (open symbols) and via MD using simulated dilatometry (filled symbols). (b) Correlation between dilute-ion conductivity and the inverse temperature difference from T_g at $T = 363$ K (experimental measurements). The dashed line indicates the linear fit of the data for the polyesters.

better understand the anomalously high conductivity of PEO.

Figure 2.5 presents an analysis of the lithium-ion coordination environments that are observed in the MD simulations. Representative MD snapshots of common lithium-ion coordination environments are shown in Figure 2.5a for each polymer. It is well-known from previous MD studies that lithium cations are coordinated by one or two contiguous chain segments in PEO;[6,7] examples of both of these binding motifs are shown at the top of Figure 2.5a. Interestingly, PEO is the only polymer among those studied here for which the lithium cation is frequently solvated by a single contiguous chain segment. This is surprising, given that the backbone

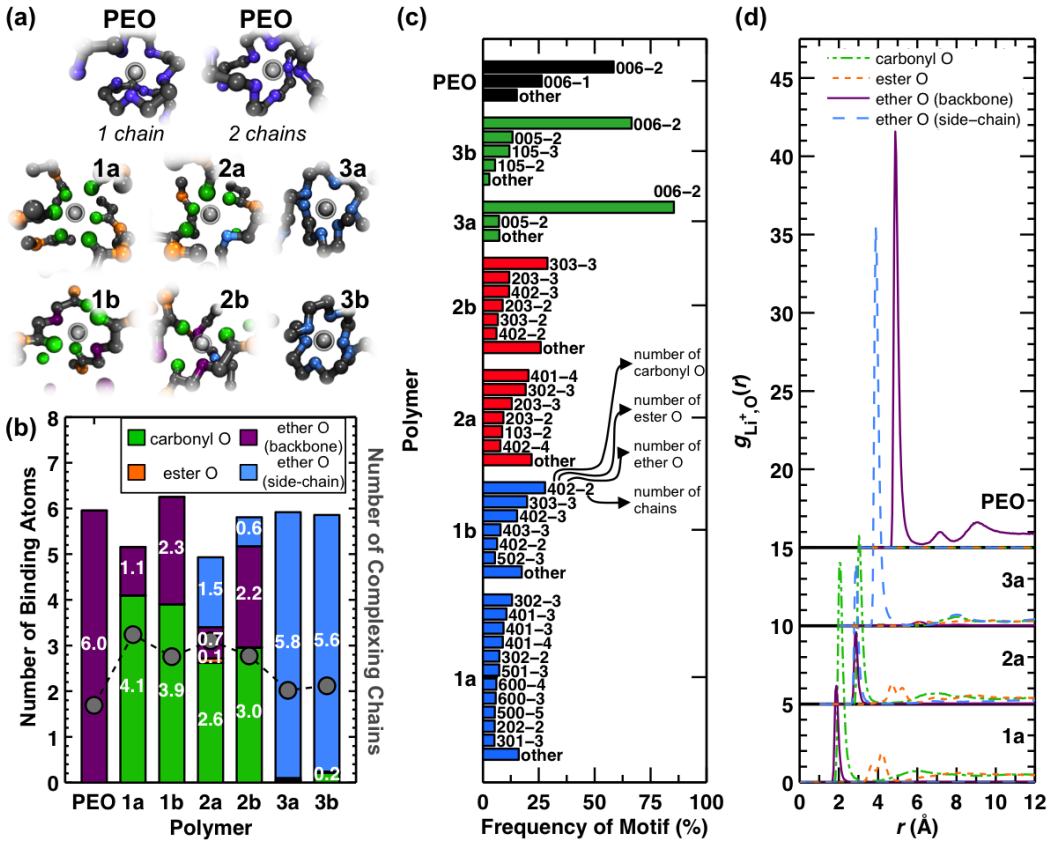

Figure 2.5: Analysis of lithium-ion coordination data from MD simulations at 363 K. (a) Representative snapshots of lithium-ion binding motifs observed in the MD simulations. The lithium cation is shown in silver, carbon atoms are black, and the oxygen atoms are colored according to the scheme in Figures 2.2 and 2.6b. (b) The average number of oxygen atoms (left y-axis) and polymer chains (right y-axis) in the first solvation shell of the lithium cation. Vertical bars report the number of different oxygen types; markers report the number of coordinating chains in the solvation shell. Note that backbone ether contributions to the type-a polymers arise due to interactions with the terminal groups of the polymer chains. (c) Frequency of occurrence for lithium-ion binding motifs, where the binding motifs are according to the number of each oxygen type and the number of coordinating chains. The first three numbers refer to the number of carbonyl, ester, and ether oxygen atoms, respectively; the number following the dash refers to the number of different contiguous polymer chain segments (i.e., 402-2 indicates a motif with four carbonyl oxygens, zero ester oxygens, and two ether oxygens from two different chains). Only binding motifs that constitute more than 5% of the ensemble are explicitly listed; the remainder are included in ?other.? (d) Cation-oxygen radial distribution functions $g_(\mathrm{Li}^+,\mathrm{O})(r)$ for different oxygen types in the type-a polymers and in PEO. The $g_(\mathrm{Li}^+,\mathrm{O})(r)$ for each oxygen type is normalized with respect to the total oxygen number density in the polymer. Following the dataset for polymer 1a, each subsequent dataset is shifted vertically (by five units) and horizontally (by 1 Å) for clarity. All statistical properties are calculated from snapshots taken at 100-ps intervals during the MD trajectory. A threshold distance of 3.25 Å from the lithium cation is used to identify constituents of the first lithium-ion solvation shell.

composition for the type-b polymers is similar to PEO. Figure 2.5a also reveals that the ester oxygens on the backbone are not typically present in the lithium-ion solvation shell for any of the polyesters. Comparison of the type-1, -2, and -3 polymers reveals that the side chain can drastically alter how the lithium cation is solvated by the polymer chain. For type-1 polymers, the side chain has no affinity for the lithium cation, and the cation predominantly coordinates with carbonyl oxygens on the polymer backbone. For type-2 and -3 polymers, oxygen atoms on the side chain do interact with the lithium cation. In fact, type-3 polymers coordinate lithium cations entirely with the PEO-like side chains.

To provide a more quantitative view of the lithium-ion solvation environments, Figure 2.5b shows the average composition of the lithium-ion coordination environment in each polymer. Interestingly, the statistics for the type-3 polymers are nearly identical to each other and similar to those of PEO. There is also marked similarity between the PEO snapshot with two coordinating chains and the snapshots for the type-3 polymers in Figure 2.5a. Whereas PEO coordinates the lithium cation with one or two chains, two to four polymer chains typically coordinate the lithium cation in the polyesters. Compared to the other polyesters, the type-3 polymers require fewer chains to coordinate the lithium cation, likely due to the coordinating ability of the PEO-like side chains. Additionally, a comparison of polymer 1a with 1b, and likewise for polymer 2a with 2b, indicates that fewer chains participate in lithium-ion coordination when polymers have an additional oxygen atom in the backbone. It is worth noting that the only ether contribution for the type-a polymers is due to the terminal groups of the polymer chain. However, additional simulations reveal that this is a minor effect.

To elucidate the compositional differences in the lithium-ion coordination environment for each polymer, Figure 2.5c presents the frequency with which different lithium-ion binding motifs are observed in the simulations. The binding motifs are identified by the number of each type of oxygen in the lithium-ion solvation shell and by the number of chains that participate in lithium-ion coordination. An array of binding motifs is observed in the type-1 and -2 polymers. In contrast, only one or two binding motifs are observed for polymers 3a, 3b, and also PEO. These results reveal a trend in which lithium cations that coordinate with more polymer chains also have more diversity in the observed binding motifs. It is interesting that the major binding motif for both the type-3 polymers and PEO is 006-2, or six ether oxygen atoms from two different polymer chains, even though PEO exhibits

substantially higher conductivity. These results indicate that the composition of the first lithium-ion solvation shell does not fully explain the trends in Figure 2.3d.

To characterize the lithium-ion solvation environment beyond the first lithium-ion solvation shell, Figure 2.5d presents pair radial distribution functions (RDFs) for the lithium cation and each type of oxygen atom in the type-a polymers and in PEO. Figure 2.5d reveals that the types of oxygen atoms that are present in the first peak, which is the lithium-ion solvation shell as discussed for Figures 2.5(a-c), are absent or depleted in the second peak. For the type-1 and -2 polymers, the first peak, which occurs at approximately 2 Å, has only backbone contributions from carbonyl and ether oxygens; the second peak, which occurs at 4-4.5 Å, is mostly comprised of ester oxygens. For type-3 polymers, side-chain ether oxygens are found in the first peak but not in the second. This difference in composition between the first and second solvation shells suggests one reason for the faster lithium-ion diffusion in PEO. Namely, diffusion events in which the lithium cation escapes from its existing coordination environment to a neighboring environment are more likely to occur in PEO because the composition of atoms in the second solvation shell is similar to the first. Consequently, a binding motif comprised of atoms in the first solvation shell is roughly equal in free energy to a binding motif that has some atoms in the first solvation shell exchanged for atoms in the second. In contrast, for the polyesters, atoms in the second peak are not typically represented in the binding motifs enumerated in Figure 2.5c, which indicates that binding motifs with those atoms are energetically less favorable.

To understand how these differences in lithium-ion solvation affect the conductivity, Figure 2.6 illustrates the displacement and coordination environment of the lithium cation in a long MD simulation for PEO and for polymer 3b. Figures 2.6(a,b) illustrate changes in lithium-ion coordination environment by tracking the indices of oxygen atoms that are within 3.25 Å of the lithium cation. In particular, each oxygen atom in the system is labeled sequentially, starting at one end of a polymer chain and continuing to the end of that chain before proceeding to the next; the oxygen atoms are consecutively labeled from 1-648 for PEO and from 1-759 for polymer 3b. What appear as solid lines in the figure are actually formed from the markers of contiguous oxygen indices, as seen in the inset; thicker lines typically consist of five or six markers, and thinner lines typically consist of three markers. Figures 2.7(c,d) show changes in the lithium-ion position by tracking the net displacement of the lithium cation from its initial position.

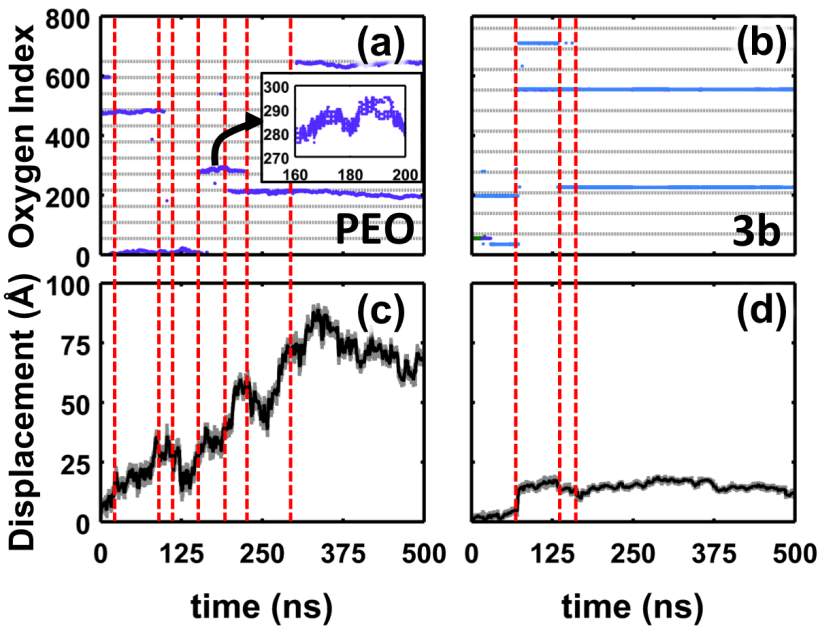

Figure 2.6: Analysis of changes in lithium-ion coordination with changes in lithium-ion position. Lithium-ion coordination environment for (a) PEO and (b) polymer 3b (markers denote coordination with oxygen for at least half of a 100-ps interval). The horizontal gray lines demarcate separate polymer chains. The inset in (a) illustrates the coordination over a 40 ns segment in the trajectory. Lithium-ion displacement from initial position in (c) PEO and (d) polymer 3b. The gray curve indicates the instantaneous displacement from the initial position, and black curve indicates the rolling average over 100-ps intervals. Vertical, red lines highlight inter-chain hopping events.

From Figures 2.6(a,b), it is clear that one characteristic of PEO is that the lines fluctuate and drift during the simulation, whereas the lines for polymer 3b are comparatively static. This drift in oxygen indices is a signature of intra-chain hopping of the lithium cation to adjacent monomers along the polymer backbone. Notably, PEO is the only polymer studied that illustrates this behavior. Intra-chain hopping events are not observed in the type-3 polymers because the lithium cation is localized to the side chains. Similarly, the lithium cation is localized between the two carbonyl groups on the backbone for the type-1 and -2 polymers, which also do not exhibit significant intra-chain hopping events. Because intra-chain hopping is not a viable mechanism in the polyesters, lithium cations are limited to diffusion via inter-chain hopping events and co-diffusion with the polymer chains. Changes in coordination that correspond to inter-chain hopping events are highlighted by the vertical, red dashed lines in Figure 2.6. Figures 2.2(c,d) illustrate that significant lithium-ion displacements often coincide with these events. However, the lithium cation in polymer 3b is limited to local fluctuations during time intervals between

inter-chain hopping events. It is evident that inter-chain hopping is a rare event that occurs on the 100-nanosecond timescale, even in PEO. Thus, the presence of intra-chain hopping in PEO is the primary reason for the faster lithium-ion diffusion compared to the polyesters.

To illustrate why these mechanistic differences arise, Figure 2.7a shows viable cation solvation sites in polymer 3a, 3b, and PEO, which are obtained from snapshots of the corresponding MD simulations for each polymer. Here, viable solvation sites are considered to be arrangements of atoms in the polymer that are consistent with common binding motifs found in Figure 2.5c; for the polymers in Figure 2.7a, sites are defined as the centroid of a set of five or more ether oxygen atoms if each oxygen is also within 3.7 Å of that centroid. Sites are connected in the figure if they are closer than 3 Å to provide a qualitative understanding of available hopping events. It is clear that far fewer viable solvation sites are identified in the type-3 polymers than for PEO; similarly sparse networks characterize the type-1 and -2 polymers. In contrast to the isolated clusters in the polyesters, PEO features a well-connected network of viable solvation sites by virtue of the compositional overlap between first and second solvation shells for the lithium cation (Figure 2.5d).

To quantify the degree to which the various polymers exhibit connected networks of solvation sites, Figure 2.7b provides the density of 3 Å connections between solvation sites, termed the connectivity, for each polymer. It is evident that the connectivity for PEO is an order-of-magnitude greater than any of the polyesters. The similarity between Figure 2.7b and Figure 2.3d is striking, indicating a strong relationship between connectivity and lithium-ion conductivity. The concept of connectivity provides an intuitive and potentially powerful explanation for the efficiency of the intra-chain hopping mechanism in PEO. In an intra-chain hopping event, the lithium cation effectively migrates up or down one polymer chain by exchanging a small number of solvating oxygen atoms. Here, this process is represented as a transition along an edge in the solvation-site network. Unlike the polymer architecture of the polyesters, the topology of PEO facilitates these transitions among solvation sites.

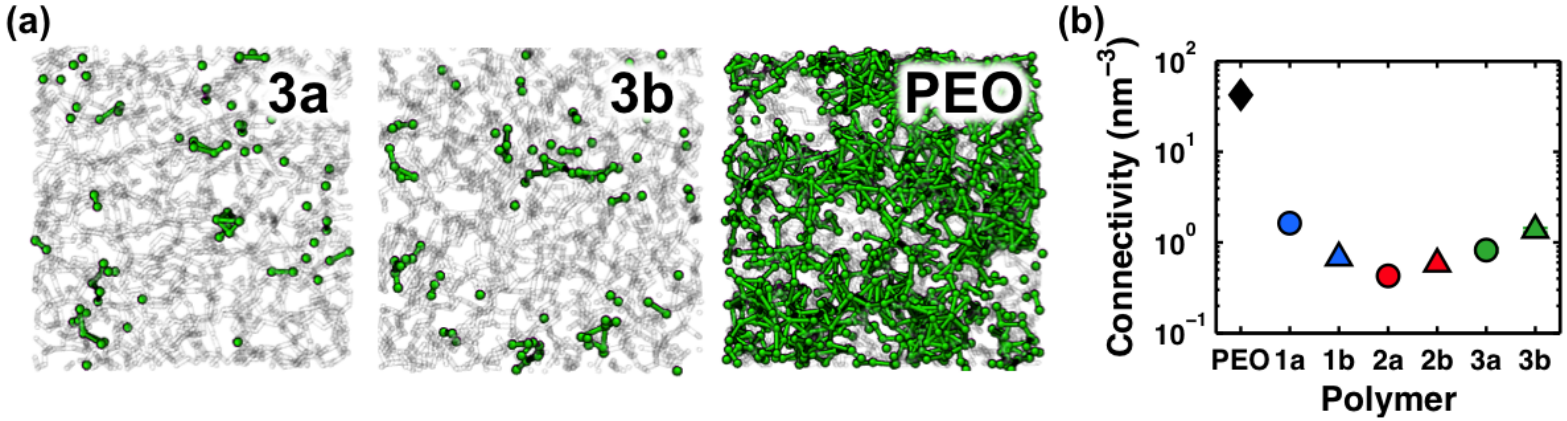

Figure 2.7: Analysis of lithium-ion solvation sites. (a) Viable solvation sites (green spheres) in representative configurations of polymer 3a, polymer 3b, and PEO. Sites connected by lines if they are within 3 Å to illustrate the relative connectivity. The polymer configuration is shown in the transparent representation. (b) The connectivity density of lithium-ion solvation-site networks for each polymer. Reported data are obtained from averaging over sixteen MD trajectory snapshots.

2.5 Conclusions

This study combines experimental and theoretical approaches to investigate the mechanisms of lithium-ion transport in six new polyester-based polymer electrolytes, as well as PEO. The modifications to polymer architecture considered are shown to significantly alter the lithium-ion solvation environment and effectively change whether the lithium-ion transport is side-chain- or backbone-mediated. These changes affect the ionic conductivity by a factor of three. In contrast, the ionic conductivities of the polyesters are about an order-of-magnitude lower than in PEO (Figure 2.3d). Because the glass-transition temperature of PEO is only modestly lower than that of some of the polyesters, the observed trends with ionic conductivity are not adequately explained on the basis of polymer segmental mobility (Figure 2.4b).

To understand the anomalous diffusivity of PEO, the MD simulations are employed to perform an extensive analysis of the lithium-ion solvation and diffusion mechanisms in the various polymers. We find that PEO is the only polymer studied that frequently coordinates a lithium cation with a single chain or exhibits significant intra-chain hopping of the lithium cations. This is primarily because the first and second lithium-ion solvation shells differ significantly in composition for all of the polyesters (Figure 2.5d). Lithium-ion diffusion in the polyesters thus relies upon inter-chain hopping events, which occur infrequently on the 100-nanosecond timescale, and co-diffusion with the polymer chains, which is intrinsically slow (Figure 2.6).

This analysis reveals that the anomalously high conductivity of PEO (Figure 2.3d) can be easily understood in terms of a description of lithium-ion diffusion based on the density and proximity of viable solvation sites (Figure 2.7a). Whereas PEO features a well-connected network of viable solvation sites, the polyesters have isolated clusters of sites that hinder efficient lithium-ion conduction. A simple metric of connectivity predicts an order-of-magnitude higher conductivity for PEO than the polyesters (Figure 2.7b). Knowledge of the solvation structure, including attributes of the second solvation shell, the connectivity between solvation sites, and the number of chains involved in the coordination appears to provide a powerful tool for the design of future SPEs.

References

(1) Fenton, D; Parker, J; Wright, P *Polymer* **1973**, *14*, 589–589.

(2) Gray, F., *Solid Polymer Electrolytes: Fundamentals and Technological Applications*; Wiley: 1991.

(3) Shriver, D; Papke, B; Ratner, M; Dupon, R; Wong, T; Brodwin, M *Solid State Ion.* **1981**, *5*, 83–88.

(4) Meyer, W. H. *Adv. Mater.* **1998**, *10*, 439–448.

(5) Tarascon, J.; Armand, M *Nature* **2001**, *414*, 359–367.

(6) Borodin, O; Smith, G. *Macromolecules* **2006**, *39*, 1620–1629.

(7) Müller-Plathe, F; Vangunsteren, W. *J. Chem. Phys.* **1995**, *103*, 4745–4756.

(8) Neyertz, S; Brown, D *J. Chem. Phys.* **1996**, *104*, 3797–3809.

(9) Siqueira, L.; Ribeiro, M. *J. Chem. Phys.* **2005**, *122*.

(10) Siqueira, L. J. A.; Ribeiro, M. C. C. *J. Chem. Phys.* **2006**, *125*.

(11) Diddens, D.; Heuer, A.; Borodin, O. *Macromolecules* **2010**, *43*, 2028–2036.

(12) Duan, Y.; Halley, J.; Curtiss, L; Redfern, P *J. Chem. Phys.* **2005**, *122*.

(13) Karo, J.; Brandell, D. *Solid State Ion.* **2009**, *180*, 1272–1284.

(14) Brandell, D.; Priimaegi, P.; Kasemaegi, H.; Aabloo, A. *Electrochim. Acta* **2011**, *57*, 228–236.

(15) Borodin, O; Douglas, R; Smith, G. A.; Trouw, F; Petrucci, S *J. Phys. Chem. B* **2003**, *107*, 6813–6823.

(16) Croce, F.; Appetecchi, G. B.; Persi, L.; Scrosati, B. *Nature* **1998**, *394*, 456–458.

(17) Croce, F; Persi, L; Scrosati, B; Serraino-Fiory, F; Plichta, E; Hendrickson, M. *Electrochim. Acta* **2001**, *46*, 2457 –2461.

(18) Johansson, P.; Ratner, M. A.; Shriver, D. F. *J. Phys. Chem. B* **2001**, *105*, 9016–9021.

(19) Nishimoto, A.; Watanabe, M.; Ikeda, Y.; Kohjiya, S. *Electrochim. Acta* **1998**, *43*, 1177 –1184.

(20) Watanabe, M.; Hirakimoto, T.; Mutoh, S.; Nishimoto, A. *Solid State Ion.* **2002**, *148*, 399 –404.

(21) Matoba, Y.; Ikeda, Y.; Kohjiya, S. *Solid State Ion.* **2002**, *147*, 403 –409.

(22) Buriez, O; Han, Y.; Hou, J; Kerr, J.; Qiao, J; Sloop, S.; Tian, M.; Wang, S. *J. Power Sources* **2000**, *89*, 149–155.

(23) Khurana, R.; Schaefer, J. L.; Archer, L. A.; Coates, G. W. *J. Am. Chem. Soc.* **2014**, *136*, 7395–7402.

(24) Alloin, F; Sanchez, J. Y.; Armand, M *J. Electrochem. Soc* **1994**, *141*, 1915–1920.

(25) Andrieu, X; Fauvarque, J. F.; Goux, A; Hamaide, T; Mhamdi, R; Vicedo, T *Electrochim. Acta* **1995**, *40*, 2295–2299.

(26) Deng, Y. L.; Ding, J. F.; Y U, G; Mobbs, R. H.; Heatley, F; Price, C; Booth, C *Polymer* **1992**, *33*, 1959–1962.

(27) Florjanczyk, Z; Krawiec, W; Wieczorek, W; Przyluski, J *Angewandte Makromolekulare Chemie* **1991**, *187*, 19–32.

(28) Ikeda, Y; Masui, H; Matoba, Y *J. Appl. Polym. Sci* **2005**, *95*, 178–184.

(29) Schroers, M; Kokil, A; Weder, C *J. Appl. Polym. Sci* **2004**, *93*, 2883–2888.

(30) Wolfenson, A.; Torresi, R.; Bonagamba, T.; DePaoli, M.; Panepucci, H *J. Phys. Chem. B* **1997**, *101*, 3469–3473.

(31) Barteau, K. P.; Wolffs, M.; Lynd, N. A.; Fredrickson, G. H.; Kramer, E. J.; Hawker, C. J. *Macromolecules* **2013**, *46*, 8988–8994.

(32) Nithya, H.; Selvasekarapandian, S.; Kumar, D. A.; Sakunthala, A.; Hema, M.; Christopherselvin, P.; Kawamura, J.; Baskaran, R.; Sanjeeviraja, C. *Mater. Chem. Phys.* **2011**, *126*, 404–408.

(33) Tanaka, R; Sakurai, M; Sekiguchi, H; Mori, H; Murayama, T; Ooyama, T *Electrochim. Acta* **2001**, *46*, 1709–1715.

(34) Watanabe, M.; Rikukawa, M.; Sanui, K.; Ogata, N.; Kato, H.; Kobayashi, T.; Ohtaki, Z. *Macromolecules* **1984**, *17*, 2902–2908.

(35) Blonsky, P. M.; Shriver, D. F.; Austin, P; Allcock, H. R. *Solid State Ion.* **1986**, *18-9*, 258–264.

(36) Harris, C. S.; Shriver, D. F.; Ratner, M. A. *Macromolecules* **1986**, *19*, 987–989.

(37) Lee, Y. C.; Ratner, M. A.; Shriver, D. F. *Solid State Ion.* **2001**, *138*, 273–276.

(38) Zhang, Z.; Jin, J.; Bautista, F; Lyons, L.; Shariatzadeh, N; Sherlock, D; Amine, K; West, R *Solid State Ion.* **2004**, *170*, 233 –238.

(39) Tominaga, Y; Shimomura, T; Nakamura, M *Polymer* **2010**, *51*, 4295–4298.

(40) Nakamura, M.; Tominaga, Y. *Electrochim. Acta* **2011**, *57*, 36–39.

(41) Jeske, R. C.; DiCiccio, A. M.; Coates, G. W. *J. Am. Chem. Soc* **2007**, *129*, 11330–+.

(42) DiCiccio, A. M.; Coates, G. W. *J. Am. Chem. Soc* **2011**, *133*, 10724–10727.

(43) Longo, J. M.; DiCiccio, A. M.; Coates, G. W. *J. Am. Chem. Soc* **2014**, *136*, 15897–15900.

(44) Maitra, A.; Heuer, A. *Phys. Rev. Lett.* **2007**, *98*.

(45) Teran, A. A.; Tang, M. H.; Mullin, S. A.; Balsara, N. P. *Solid State Ion.* **2011**, *203*, 18–21.

(46) Vanommeslaeghe, K.; Hatcher, E.; Acharya, C.; Kundu, S.; Zhong, S.; Shim, J.; Darian, E.; Guvench, O.; Lopes, P.; Vorobyov, I.; Mackerell, A. D. *J. Comput. Chem.* **2010**, *31*, 671–690.

(47) Martin, M. G.; Siepmann, J. I. *J. Phys. Chem. B* **1999**, *103*, 4508–4517.

(48) Wick, C. D.; Martin, M. G.; Siepmann, J. I. *J. Phys. Chem. B* **2000**, *104*, 8008–8016.

(49) Stubbs, J. M.; Potoff, J. J.; Siepmann, J. I. *J. Phys. Chem. B* **2004**, *108*, 17596–17605.

(50) Kamath, G.; Robinson, J.; Potoff, J. J. *FFE* **2006**, *240*, 46 –55.

(51) Wu, H.; Wick, C. D. *Macromolecules* **2010**, *43*, 3502–3510.

(52) Plimpton, S. *J. Comp. Phys.* **1995**, *117*, 1 –19.

(53) Brown, W. M.; Wang, P; Plimpton, S. J.; Tharrington, A. N. *Comput. Phys. Commun.* **2011**, *182*, 898–911.

(54) Brown, W. M.; Kohlmeyer, A.; Plimpton, S. J.; Tharrington, A. N. *Comput. Phys. Commun.* **2012**, *183*, 449–459.

(55) Newman, J. S.; Thomas-Alyea, K. E., *Electrochemical systems*, 3rd; Wiley-Interscience: Hoboken, N.J., 2004, xx, 647 p.

(56) Killis, A; Lenest, J. F.; Cheradame, H; Gandini, A *Makromolekulare Chemie-Macromolecular Chemistry and Physics* **1982**, *183*, 2835–2845.

(57) Blonsky, P. M.; Shriver, D. F.; Austin, P; Allcock, H. R. *J. Am. Chem. Soc* **1984**, *106*, 6854–6855.

(58) Videa, M; Xu, W; Geil, B; Marzke, R; Angell, C. A. *J. Electrochem. Soc* **2001**, *148*, A1352–A1356.

Chapter 3

RELATIONSHIP BETWEEN CONDUCTIVITY AND SOLVATION-SITE CONNECTIVITY IN ETHER-BASED POLYMER ELECTROLYTES

In Chapter 2, we found that the notion of solvation-site connectivity provided a powerful and intuitive explanation for the observed disparities in conductivity between PEO and a family of polyesters. Although the glass-transition temperature is known to play an important role in conductivity, this observation is historically unique, and the agreement between Figures 2.3d and 2.7b is suggestive of direct correlation between ionic conductivity and solvation-site connectivity. Nevertheless, that correlation was conflated with other effects and not systematically investigated.

In this chapter, we systematically investigate the correlation between conductivity, σ, and theoretical metrics for the solvation-site connectivity through combined experimental and computational analysis of ion transport in a set of linear polyethers synthesized via Acyclic Diene Metathesis (ADMET) polymerization. Here, the ADMET synthesis enables a tunable methodology to modulate the solvation-site connectivity by adding aliphatic linkers to a poly(ethylene oxide) (PEO) backbone; The addition of these aliphatic linkers lowers T_g and dilutes the polar groups; both factors influence ionic conductivity. To isolate these effects, a two-step normalization scheme is used. In the first step, Vogel-Fulcher-Tammann fits are used to calculate a temperature-dependent reduced conductivity, $\sigma_r(T - T_g)$, which is defined as the conductivity of the electrolyte of interest at a fixed value of $T - T_g$ and Li:O ratio. In the second step, we compute a dimensionless parameter f_{exp}, defined as the ratio of the reduced ionic mobility of the polymer electrolyte of interest to that of a reference polymer electrolyte (PEO). For the polymers studied, f_{exp} correlates well with oxygen mole fraction, x_O, and is, to a good approximation, independent of temperature and salt concentration. Molecular dynamics simulations are performed on neat polymers to quantify the occurrences of solvation motifs that are similar to those obtained in the vicinity of isolated lithium ions, and various theoretical metrics are reported for the solvation-site connectivity. We show that f_{exp} is a linear function of the simulation-derived connectivity metrics. From the relationship between σ_r and f_{exp}, a universal equation is proposed to predict the conductivity of ether-based polymer electrolytes at any salt concentration and temperature.

The experimental synthesis featured in this chapter was performed by Dr. Yuki Jung and Mr. Qi Zheng under the direction of Prof. Geoffrey W. Coates at Cornell University, and the preparation and characterization of the polymer electrolytes was performed by Ms. Danielle M. Pesko under the direction of Prof. Nitash P. Balsara at the University of California, Berkeley. Data and content in this chapter have been submitted for publication as D.M. Pesko,* M.A. Webb,* Y. Jung,* Q. Zheng, T.F. Miller III, G.W. Coates, N.P. Balsara. "The Relationship between Connectivity and Conductivity in Polymer Electrolytes."

3.1 Introduction

As the size and energy density of rechargeable lithium batteries continues to increase, the safety of the technology is of growing concern.[1,2] Solvent-free polymer electrolytes (SPEs) are of considerable interest as they offer improved thermal stabilities and reduced flammabilities compared to those of conventional organic solvent electrolytes.[3,4] The vast majority of research in the field of SPEs has focused on polyethers such as poly(ethylene oxide) (PEO),[5–8] which form stable complexes with alkali metal ions such as Li^+.[9–11] Amorphous mixtures of PEO and lithium salts exhibit reasonable ionic conductivities on the order of 10^{-3} S/cm at 90 °C.

Substantial effort has been directed towards improving the conductivity of PEO through the incorporation of nanoparticles,[12–15] plasticizers,[16–21] or a second polymer blended into the PEO matrix.[20,22,23] Alternative approaches involve altering the chemical structure of PEO by adding cross-links,[24–26] changing the monomer chemistry,[27–29] incorporating co-monomers into the PEO backbone,[30–32] and modifying the architecture of the polymer chain.[26,32–34] However, these materials have not resulted in significant improvement of electrolyte performance or commercial impact, due in part to limited understanding of the molecular mechanisms underpinning ion transport.

In Chapter 2 and supporting publications,[35,36] we identified that the addition of groups that do not interact with the lithium ion can dilute and alter the sites in which a lithium ion can be solvated, leading to overall reductions in ionic conductivity. The significantly higher conductivity of PEO relative to that of a set of polyesters was explained using the concept of solvation-site connectivity, quantified using molecular simulation by the number and proximity of solvation sites in the polymer matrix.[35] For a series of polyethers (also studied in Chapter 4), a low density of solvation sites resulted in slow rates of lithium-ion hopping.[36] The role of spacing

between coordinating centers has also been alluded to recently in the context of poly(ether-thioethers).[37]

Here, both experiments and simulations are used to quantify the relationship between conductivity and solvation-site connectivity in a set of polyethers in which ethylene oxide (EO) segments are regularly interrupted with carbon linkers of varying lengths (Figure 3.1). The polymers, labeled as C_xEO_y, are distinguished by x, the number of carbon atoms in the carbon linker, and y, the number of consecutive ethylene oxide (EO) monomers in the PEO segment. The conductivity of the C_xEO_y electrolytes can be calculated using the known conductivity of PEO electrolytes and a multiplicative correction factor that depends largely on oxygen mole fraction. The same correction factor applies to the entire set of electrolytes, irrespective of temperature and salt concentration. Simulations show that introducing carbon linkers of varying lengths and frequencies affects solvation-site connectivity, and the relationship between the experimentally determined correction factor and the connectivity is explored.

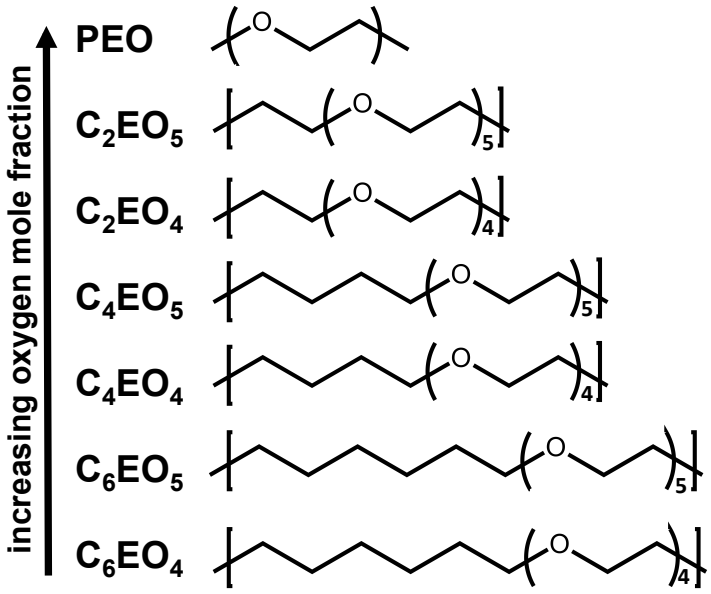

Figure 3.1: Structure of the C_xEO_y polyethers synthesized and characterized in this study. The naming convention specifies x, the length of the carbon linker, and y, the number of consecutive ethylene oxide units in each repeat unit.

3.2 Methodology

3.2.a Polymer Synthesis and Characterization

The polyethers shown in Figure 3.1 were synthesized via Acyclic Diene Metathesis (ADMET) polymerization,[31] followed by hydrogenation with Crabtree's catalysts

(Figure 3.2). The diene terminated monomers were synthesized in one step from the facile substitution reaction of the commercially available poly(ethylene glycol) (PEG) oligomers (tri-, or tetraethylene glycol) with allyl bromide and 5-bromo-1-pentene to yield the C_2EO_y and C_6EO_y monomers respectively. The C_4EO_y monomers were synthesized by mesylating PEG oligomers first and subsequently reacting with 3-butene-1-ol. This alternative procedure was used because the elimination reaction between PEG oligomers and 4-bromo-1-butene significantly lowered the yields of the desired product. The C_xEO_y monomers were then polymerized with Grubbs' first generation catalyst. The Grubbs' catalyst was used because of its high functional group tolerance and reduced propensity for olefin isomerization reactions.[38] The synthesized unsaturated polyethers were hydrogenated using Crabtree's catalyst to yield the saturated polyethers for this study.

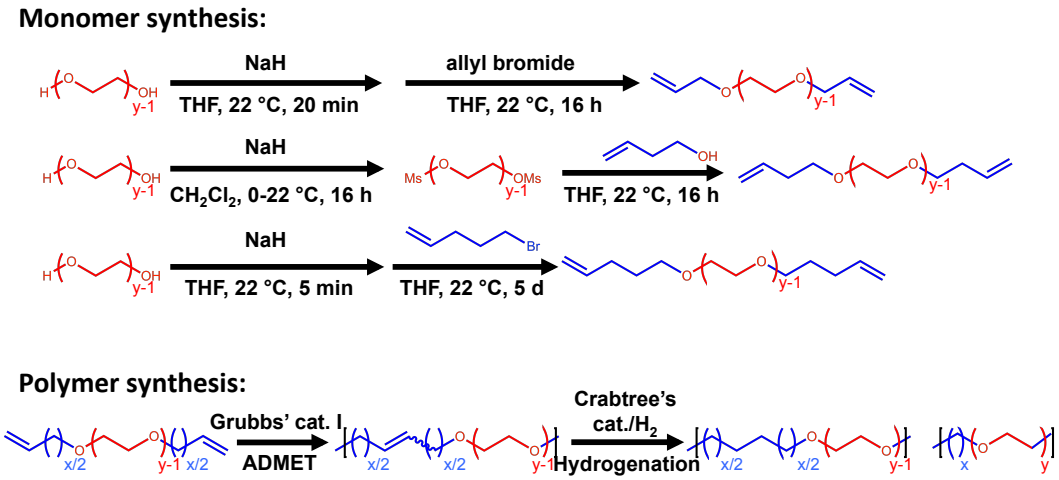

Figure 3.2: Synthesis of C_xEO_y monomers and polymers via Acyclic Diene Metathesis (ADMET) polymerization followed by hydrogenation.

The C_xEO_y polymers synthesized in this study are characterized with gel permeation chromatography (GPC) for the number-averaged molecular weight (M_n) and polydispersity index (Đ). Thermal properties of the C_xEO_y polymers are measured with differential scanning calorimetry. The results are summarized in Table 3.1, along with the properties of PEO, which was commercially purchased from Polymer Source. The M_n of the polymers range from 4.7 up to 19.0 kDa (Table 3.1), such that the ionic conductivities are expected to be independent of M_n.[39] The reactivity of the monomers showed some dependence on the number of carbons in the linker with the longest linker (C_6) yielding the polymer with highest M_n. This trend is consistent with the literature on ADMET polymerization of oxygen-containing dienes

using Schrock-type catalysts.[40,41] The glass transition temperatures, T_g, of C_2EO_5 (-72.8 °C) and C_2EO_5 (-67.0 °C) are lower than that of PEO (-60.0 °C) likely due to the increased chain flexibility of the carbon linkers. The level of crystallinity in the neat C_4EO_y and C_4EO_y precluded the observation of a T_g, but we expect that those values would decrease as the linker length increases. All of the C_xEO_y polyethers synthesized have a significantly lower T_m relative to PEO.

The mole fraction of oxygen, x_O, in each polymer is calculated using

$$x_O = \frac{\text{oxygen atoms in repeat unit}}{\text{total atoms in repeat unit}}, \tag{3.1}$$

where the number of atoms in the repeat unit excludes hydrogen atoms. Values for x_O for each polymer are shown in Table 3.1.

Table 3.1: Summary of polymer properties.

Polymer	M_n (kg/mol)	Đ	T_g (°C)	T_m (°C)	x_O
PEO[a]	5.0	1.1	−60.0	60.0	0.333
C_2EO_4	7.4	1.3	−72.8	−2.8	0.286
C_2EO_5	6.7	1.5	−67.0	−4.5, 9.0	0.294
C_4EO_4	4.7	1.4	n.d.[b]	13.4	0.250
C_4EO_5	7.1	1.6	n.d.[b]	8.0	0.263
C_6EO_4	12.9	1.8	n.d.[b]	24.7, 33.4	0.222
C_6EO_5	19.0	1.8	n.d.[b]	23.4	0.238

[a] T_g and conductivity measurements are performed on 4.6 kg/mol and 5.0 kg/mol PEO, respectively.

[b] No signature detected.

3.2.b Electrolyte Characterization

Electrolyte preparation took place inside an argon glovebox (MBraun) in order to maintain water and oxygen levels below 1 ppm and 10 ppm respectively. The polyethers synthesized in this study, along with PEO, are dried under vacuum at 90 °C for 12 h prior to entering the glovebox. Mixtures of polymer and lithium bis(trifluoromethanesulfonyl) imide (LiTFSI) salt (Novalyte) are dissolved in anhydrous dimethylformamide (DMF) and stirred at 90 °C for a minimum of 3 h to form a homogeneous solution. The DMF is then evaporated from the solution, and the polymer/salt mixture is transferred to the glovebox antechamber and dried under vacuum for 8 h at 90 °C to remove any excess solvent. Electrolytes are prepared at

varying salt concentrations, ranging from $r = 0.06$ to $r = 0.14$, where $r = n_{\mathrm{Li}}/n_{\mathrm{O}}$ is the molar ratio of lithium ions to oxygen atoms in the polymer.

Stainless steel symmetric cells are prepared for ionic conductivity measurements of electrolytes using ac impedance spectroscopy. Samples are made by pressing the polymer electrolyte into a 254 μm thick silicone spacer and sandwiching between two 200 μm stainless steel electrodes. With the exception of crystalline PEO, all electrolytes are in the form of highly viscous liquids and are soft enough to be pressed at room temperature. The silicone forms a good seal with stainless steel thereby preventing the electrolytes from leaking out of the cell during characterization. A micrometer is used to obtain the thickness of the electrolyte by measuring thickness of the cell and subtracting the thickness of the electrodes. Aluminum tabs are secured to the electrodes to serve as electrical contacts. The assembly is vacuum sealed in a laminated aluminum pouch material (Showa-Denko) before removing from the glovebox for electrochemical characterization.

All reported conductivity results are based on ac impedance spectroscopy performed with a Biologic VMP3 potentiostat which acquires complex impedance measurements for a frequency range of 1 Hz to 1 MHz at an amplitude of 80 mV. The low-frequency minimum on the Nyquist impedance plot is taken to be the electrolyte resistance, R, which is used along with electrolyte thickness, l, and electrolyte area, a, to calculate the electrolyte conductivity, σ, according to

$$\sigma = \frac{l}{aR_b}, \tag{3.2}$$

where $a = 3.175$ mm is the inner diameter of the spacer and l is taken to be the final thickness of the electrolyte, measured after conductivity measurements are completed. On average, the electrolyte thickness decreased 3.5% after annealing. The symmetric cells are disassembled to allow for visual inspection of the electrolyte. Any samples that exhibited bubbles or voids in the polymer are discarded from the set, as such defects would alter the electrolyte volume and produce inaccurate conductivity results. Fewer than 5% of samples prepared in this study exhibited such characteristics. The conductivity for each electrolyte is determined by averaging the results from three different samples, and the error bars signify the standard deviation of these measurements.

DSC experiments are performed on a TA Instruments DSC Q200 instrument to obtain the T_{g} and T_{m} of each electrolyte. DSC samples are prepared inside the glovebox, where aluminum pans are filled with 1-5 mg of electrolyte and hermeti-

cally sealed before removing from the glovebox. The following protocol is used for the temperature scan: heat to 110 °C at 20 °C/min, cool to -90 °C at 5 °C/min, heat to 110 °C at 20 °C/min. Values for T_g and T_m are obtained from the second heating scan. DSC measurements are repeatable within 1.0 °C.

3.2.c Molecular Dynamics Simulations

All MD simulations employ a united atom force field, with bonding parameters taken from CHARMM[42] and all other parameters taken from the TraPPE-UA force field;[43] compatible lithium ion parameters are obtained from a previous simulation study.[44] All simulations are performed using the LAMMPS simulation package[45] with GPU acceleration.[46,47] The equations of motion are evolved using the velocity-Verlet integrator with a 1 fs time step. Particle-particle-particle mesh Ewald summation[47] is used to compute all nonbonded interactions beyond a 14 Å cutoff. The Nosé-Hoover (100 fs relaxation) and Nosé-Hoover barostat (1000 fs relaxation) are used in all simulations to control the temperature and pressure.

Two sets of simulations are performed for the C_xEO_y polymers. For polymers with x = 2, 4, and 6 and y = 3-8, neat-polymer simulations are used to obtain polymer properties and solvation-site connectivity metrics. For polymers with x = 2 and y = 3-8, simulations of a single lithium cation diffusing in a polymer are used to investigate the lithium-ion solvation environment.

For the neat-polymer simulations, four independent copies of the simulation cell are generated for each polymer studied. Each copy consists of a single, long polymer chain (Mn 25000 g/mol) with an initial configuration generated via a self-avoiding random walk. For the ion-containing simulations, the same procedure is used, except that a single lithium cation is randomly placed in the simulation cell, and the total charge of the system is neutralized with a uniform background charge.[48] To generate starting configurations for MD production runs, the systems are equilibrated in five steps. In step 1, the initial configuration is relaxed for 10,000 steps with non-periodic boundary conditions using steepest descent energy minimization with the maximum atom displacement limited to 0.1 Å for any given step. In step 2, the system is annealed at 726.85 °C with periodic boundary conditions using 100,000 steps of Langevin dynamics with a 100 fs damping factor. In step 3, the simulation cell is adjusted at a constant rate over 500 ps at 226.85 °C to achieve a cubic simulation cell with a density of 1.0 g/cm3. In step 4, the system is annealed for 1.5 ns at 226.85 °C and 1 atm. In step 5, the system is equilibrated for 10 ns at 90 °C

and 1 atm.

Following equilibration, production runs of 10 ns for the neat-polymer simulations and of 150 ns for the ion-containing systems are performed at 90 °C and 1 atm.

3.3 Results

3.3.a Experimental Conductivity

The ionic conductivity, σ, of the C_xEO_y polyethers and PEO was measured as a function of temperature, T, in the range of 27-110 °C. Figure 3.3 shows the results at a fixed salt concentration, $r = 0.08$, which is in the vicinity where PEO conductivity is maximized.[5] Results from Figure 3.3 indicate that the σ of the C_xEO_y polyethers are within one order of magnitude of PEO at all temperatures. The relative ordering of the polymers does not change significantly as T is varied. We observe that at any given T, C_2EO_5 and PEO exhibit the highest σ, which are comparable within error. Of the polyethers synthesized in this study, C_2EO_5 has the shortest carbon linker (two) and the longest consecutive segment of ethylene oxide (EO) monomers (five); thus, C_2EO_5 has the largest mole fraction of oxygen, x_O (Table 3.1), of the C_xEO_y polymers. Similarly, C_6EO_4 has the lowest x_O and exhibits the lowest σ. As might be anticipated, results from Figure 3.3 suggest that there is a relationship between the x_O and σ.

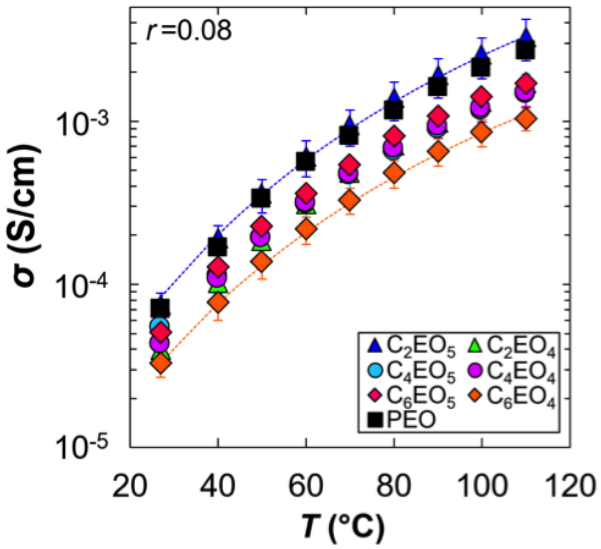

Figure 3.3: Conductivity, σ, with increasing temperature at r =0.08.

To further explore this relationship, Figure 3.4a shows σ of the C_xEO_y polyethers and PEO as a function of x_O at r =0.08 and 90 °C. The measured conductivities of the polymers are within a narrow range between 6.5×10^{-4} S/cm and 1.7×10^{-3} S/cm.

In some cases increasing the linker length increases σ (C_2EO_4 vs. C_4EO_4), while in other cases it decreases σ (C_2EO_5 vs. C_4EO_5). Similarly, an additional consecutive EO unit in the monomer may either increase σ (C_2EO_4 vs. C_6EO_4) or decrease σ (C_4EO_4 vs. C_4EO_5). The lack of clear trends in this data most likely results from two competing effects upon the addition of carbon linkers. Namely, the presence of the linkers dilutes the density of lithium-ion solvation sites (making hopping between sites less probable) but simultaneously changes the thermal properties of the polymer melt. Figure 3.4b shows the glass transition temperature, T_g, of the C_xEO_y and PEO electrolytes at a salt concentration of r =0.08. It is evident that decreasing x_O decreases T_g due to increased chain flexibility. It is generally accepted that more flexible chains promote ion transport due to rapid segmental motion.[49–51]

To decouple the effects of solvation site density and segmental motion, we calculate a reduced conductivity, σ_r. This approach has been used previously in analysis of experimental data from polymer electrolytes.[5,52,53] To calculate σ_r, we use a modified Vogel-Fulcher-Tammann (VFT) equation where the temperature is defined such that it is a fixed distance, T^*, above the measured T_g of the electrolyte,

$$\sigma_r(T^*) = A(T_g + T^*)^{-1/2} \exp\left(\frac{-E_a}{R(T_g + T^* - T_0)}\right), \tag{3.3}$$

where $T_0 = T_g - 50℃$ is the traditional VFT reference temperature. The two dotted curves in Figure 3.3 show VFT fits for C_2EO_5 and C_6EO_4 (other fits are omitted for clarity). These fits enable estimation of a pseudo-activation energy, E_a, and a prefactor, A. Figure 3.4c shows σ_r of the C_xEO_y polyethers and PEO as a function of x_O for T^* = 75 K. Once the contribution from T_g differences is corrected for, it becomes clear that the reduced conductivity is a monotonically increasing function of x_O. In other words, decreasing the linker length or the addition of an EO unit leads to an increase in σ_r. Since the VFT curves for the polymers are essentially parallel, the dependence of σ_r on x_O is qualitatively similar to that seen in Figure 3.4c at all values of $T - T_g$. All the electrolytes in Figure 3.4c have a fixed salt concentration of r =0.08; consequently, electrolytes with a lower x_O will typically have less salt per unit volume. Therefore, it is unclear whether the trend observed in Figure 3.4c is due to changes in molecular structure or simply results from changes in volumetric density of charge carriers in the electrolytes.

To isolate the effect of monomer structure on conductivity, we define an experimental connectivity, f_{exp}:

$$f_{exp} = \left(\frac{\sigma_r}{\sigma_{r,PEO}}\right)_{T^*} \frac{x_{O,PEO}}{x_O}. \tag{3.4}$$

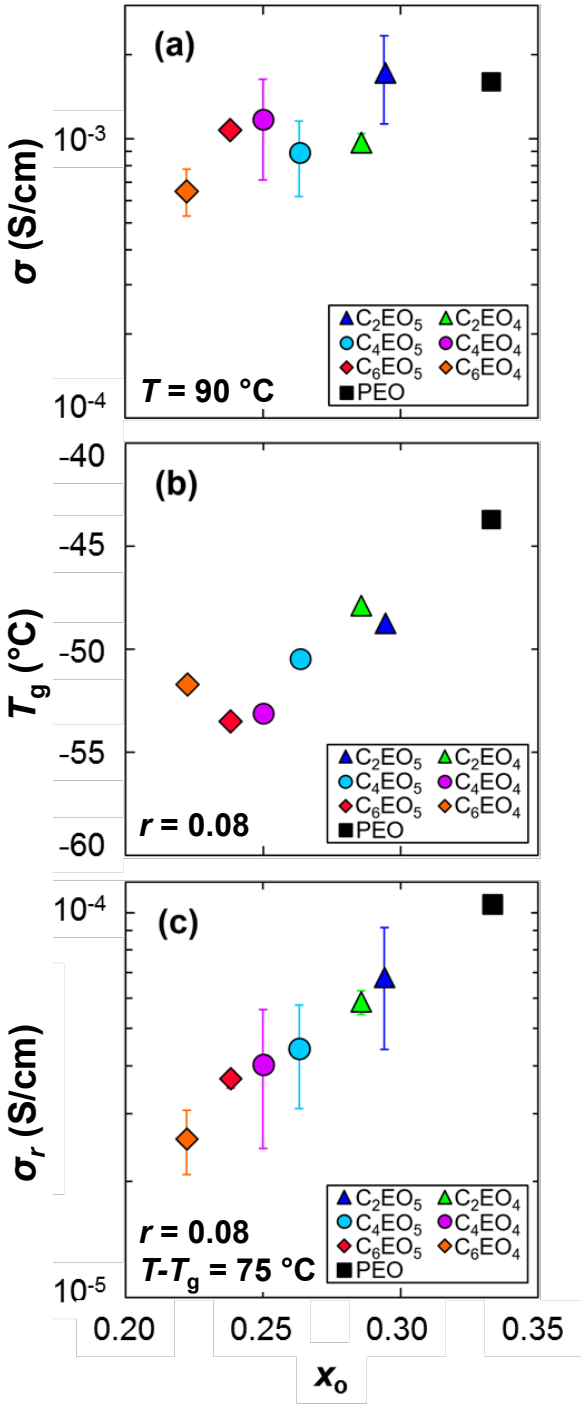

Figure 3.4: (a) Conductivity, σ, at 90 °C and (b) glass transition temperature, T_g, and (c) reduced conductivity, σ_r, with increasing mol fraction of oxygen atoms, x_O, on the polymer backbone. All data is collected at a salt concentration of r =0.08.

The ratio of $\sigma_r/\sigma_{r,\mathrm{PEO}}$ at a given r and $T^* = T - T_g$ quantifies the conductivity of a C_xEO_y electrolyte relative to that of PEO, correcting for the different T_g values of the

C_xEO_y electrolyte. The ratio of $x_{O,PEO}$ / x_O approximately corrects for differences in the volumetric density of salt. In Eq. (3.4), f_{exp} is somewhat analogous to the morphology factor used to describe the constraints on ion transport imposed by the geometry of the conducting phase in block copolymer systems.[54]

Figure 3.5 shows f_{exp} as a function of x_O. This plot shows that f_{exp} increases monotonically with increasing x_O. These effects are attributed to changes in the local environment of the lithium ion. As x_O is decreased, there are likely more carbon linker segments and fewer EO segments in the vicinity of each solvated lithium ion. Assuming the carbon linkers are ionically insulating, polymers with a lower x_O are expected to exhibit slower lithium-ion diffusion, as it takes longer for the ion to hop to an adjacent solvation site. Thus, f_{exp}, is an experimentally determined quantity that is expected to report on the proximity of lithium-ion solvation sites.

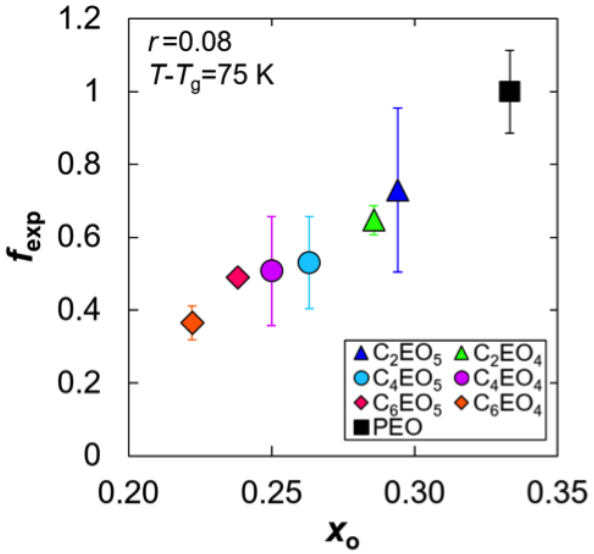

Figure 3.5: Experimental solvation-site connectivity, f_{exp}, with increasing x_O at r =0.08 and $T - T_g$=75 K.

In Figure 3.6a, f_{exp} as a function of x_O is calculated at r =0.08 and various reduced temperatures. The data for a salt concentration of r = 0.08 exhibit strong linear correlation with the equation,

$$f_{exp} = 5.39x_O - 0.86. \tag{3.5}$$

To investigate the behavior of f_{exp} across different salt concentrations, the analysis was repeated at different values of r, and the results for f_{exp} values are shown in Figure 3.6b. In Figure 3.6c, results are shown for f_{exp} at all values of r and $T - T_g$.

Although there is some scatter about the reference line in the figures, the data in Figure 3.6b and 6c are also largely consistent with Eq. (3.5).

Figure 3.6 provides justification for the normalization scheme employed in this chapter. Namely, Figure 3.6 demonstrates that when polymer electrolytes are compared using σ_r and differences in charge carrier concentration are factored out using x_O, ion transport is related to a parameter (fexp) that is largely independent of temperature and salt concentration. This supports the notion that f_{exp} is an intrinsic property of the neat polymer rather than a quantity that strongly depends on salt concentration.

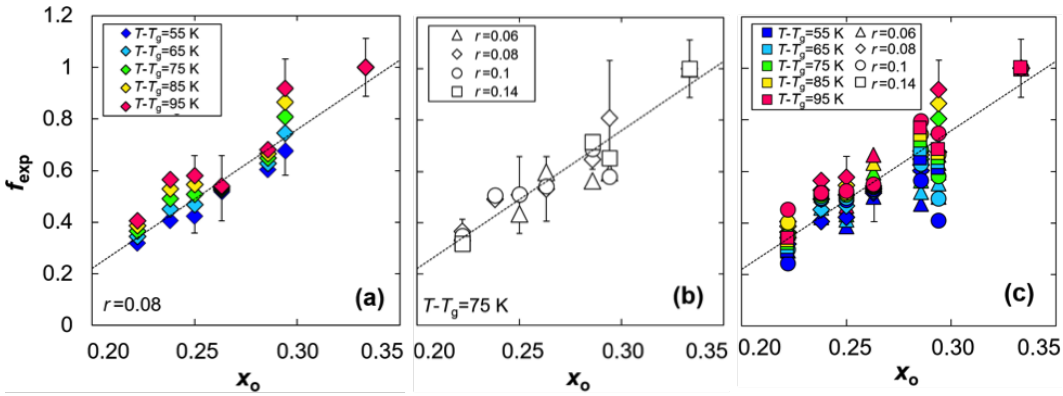

Figure 3.6: Experimental solvation-site connectivity, f_{exp}, with increasing x_O at varying (a) $T - T_g$, (b) r, and (c) $T - T_g$ and r. The green diamonds in (a) and (c) and the white diamonds in (b) show the data from Figure 3.5 with r =0.08 and $T - T_g$=75 K; error bars are only shown for this set of data. The dashed line is the same in all three figures and represents the best linear fit of the data in (c), given by Eq. 5. The correlation coefficients for the linear fits are 0.87, 0.90, and 0.85 for (a-c), respectively.

3.3.b Theoretical Solvation-site Connectivity

We now use MD simulations to further understand how varying the composition of the C_xEO_y polymers affects lithium-ion solvation and polymer properties, including the connectivity between possible lithium-ion solvation sites.

Figure 3.7 presents an analysis of the lithium-ion solvation environments observed during MD simulations of the C_2EO_y polymers in the presence of an isolated lithium ion. Representative snapshots of the lithium-ion solvation shell are shown in Figure 3.7a. In all cases, the lithium ion coordinates with one or two contiguous sequences of oxygen atoms, which is similar to coordination environments previously observed in PEO.[8,35,55] While complexation by a single contiguous sequence of oxygen atoms might be expected to be difficult in the presence of carbon linkers, the snapshots for C_2EO_3 and C_2EO_4 depict configurations for which the lithium cation indeed

coordinates with oxygen atoms separated by a linker. In general, the snapshots display strikingly similar solvation environments in terms of the number of coordinating oxygen atoms despite the changing frequency of the C_2 linker. This is confirmed in Figure 3.7b, which shows the lithium-oxygen cumulative distribution function (CDF), and in Figure 3.7c, which presents the frequency with which different lithium-ion binding motifs are observed in the simulations. Both Figure 3.7b and Figure 3.7c indicate that lithium ions in the C_2EO_y polymers are coordinated by five or six oxygen atoms, irrespective of the number consecutive EO units; similar findings are anticipated for the C_4 and C_6 linkers based on previous simulation studies.[35,36]

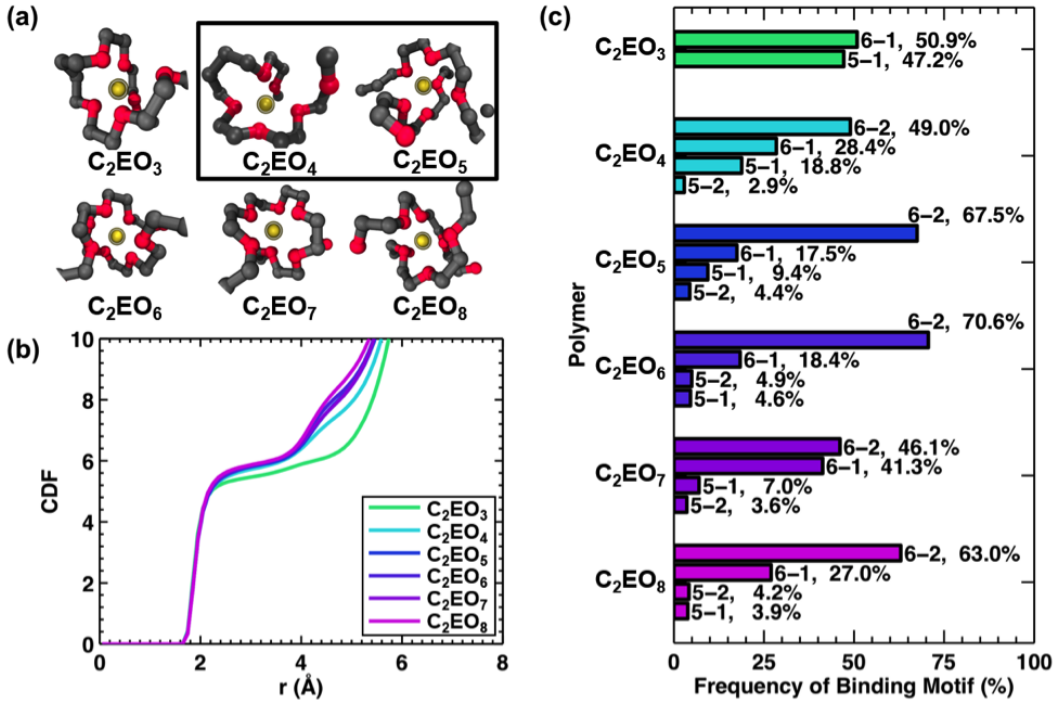

Figure 3.7: Analysis of the lithium-ion solvation environment for polymers with C_2 linkers between EO repeat units. (a) Simulation snapshots of representative lithium-ion solvation structures in polymers with different numbers of repeating EO units. The boxed snapshots correspond to polymers that have experimental data. (b) The cumulative number of oxygen atoms as a function of distance from the lithium ion, given by the lithium-oxygen cumulative distribution function (CDF). (c) Frequency of occurrence of observed lithium-ion binding motifs. The first number indicates the number of oxygen atoms that are within 3.25 Å of the lithium ion; the number after the dash refers to the number of different contiguous polymer chain segments.

We now focus on neat-polymer simulations, i.e., in the absence of the lithium ion, to examine how the addition of carbon linkers affects both the thermal properties of the polymer as well as the distribution of lithium-ion solvation sites. Figure 3.8

compares these two properties obtained for the expanded set of polymers (C_xEO_y for x = 2, 4, and 6 and y = 3-8). Figure 3.8a shows that the bulk modulus, B, at 90 °C for the polymers generally increases with increasing x_O. The polymers with C_2 linkers have larger bulk moduli than those with C_4 and C_6 linkers, and PEO (black square) possesses the largest bulk modulus among all the polymers characterized. These results are qualitatively consistent with the experimental observations in Figure 3.4b that the T_g of the electrolytes generally increases with x_O and decreases with increasing linker length.

In contrast to Figure 3.8a, Figure 3.8b shows that the average nearest-neighbor distance, $\langle r_{nn} \rangle$, between lithium-ion solvation sites generally decreases with increasing x_O. Here, a solvation site is defined at the centroid of a set of five or more oxygen atoms if each oxygen is also within 3.5 Å of the centroid; two sites are combined if the distance between their centroids is less than r_{min} = 1 Å. The figure shows that modifying the number of contiguous EO units and the length of the linker directly influences the number and proximity of solvation sites. Notably, PEO has the shortest average distance between neighboring lithium-ion solvation sites. Figure 3.8a and 3.8b combine to highlight a difficulty in designing polymers with enhanced cation diffusivity since increasing the number and proximity of lithium-ion solvation sites often increases polymer stiffness, in accordance with the experimental observations in Figure 3.4a.

Previous work introduced solvation-site connectivity as an intuitive means of explaining trends in conductivity.[35] To examine this effect for the C_xEO_y polymers, Figure 3.9 compares the distribution and proximity of solvation sites for PEO, which is the most conductive polymer in Figure 3.4c, and C_6EO_4, which is the least conductive. Figures 3.9a and 3.9d depict representative snapshots of the neat PEO and C_6EO_4 melts, respectively. Solvation sites in these snapshots are depicted as blue spheres in Figures 3.9b (PEO) and 3.9e (C_6EO_4). Figures 3.9c and 3.9f depict edges connecting the solvation sites within a cutoff distance, r_{cut} = 3 Å. Comparing Figure 3.9b and 3.9e reveals that introduction of the C_6 linker decreases the density of solvation sites in the polymer. Moreover, comparing Figure 3.8c and 3.8f illustrates that C_6EO_4 has far fewer edges than PEO. Because hopping among solvation sites is a primary mode of lithium-ion transport and hopping is typically limited to distances less than 3 Å,[8,35] having fewer edges between solvation sites is expected to reduce the overall rate of lithium-ion diffusion.

From Figures 3.6, 3.8b, and 3.9, it is clear that x_O plays an important role in both

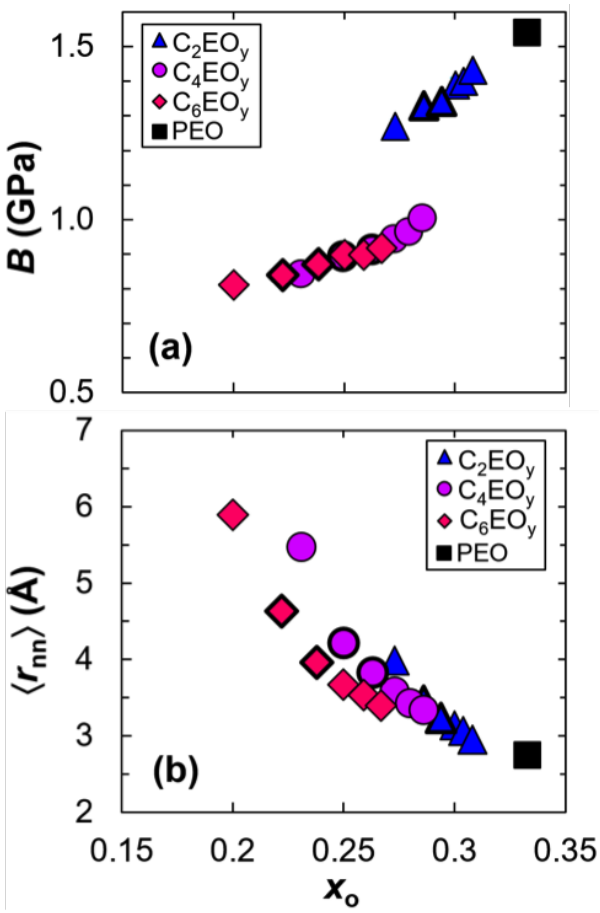

Figure 3.8: Variation of (a) the polymer bulk modulus, B, at 90 °C and (b) the average nearest-neighbor separation distance between solvation sites, $\langle r_{\mathrm{nn}} \rangle$, as a function of x_{O} for polymers with different linkers. In both (a) and (b), polymers with different linkers are denoted by different symbols. Markers with bold outlines indicate polymers that were also experimentally characterized.

the solvation-site connectivity as well as f_{exp}. To further establish the relationship between solvation-site connectivity and f_{exp}, we examine three possible metrics for characterizing the solvation-site connectivity from the simulations, including κ (the volumetric density of edges between solvation sites), λ (the linear density of edges projected along a given linear direction), and $\exp[-\langle r_{\mathrm{nn}} \rangle]$ (a proportionality to a characteristic hopping rate). Figure 3.10 provides a visual representation of these metrics for PEO. The first metric, κ (Figure 3.10a), is computed using

$$\kappa = \frac{1}{V} \sum_{i<j} H(r_{\mathrm{cut}} - r_{ij}), \tag{3.6}$$

where V is the volume of the simulation cell, the summations run over pairs of solvation sites in the simulation cell, and $H(r)$ is the typical Heaviside step function.

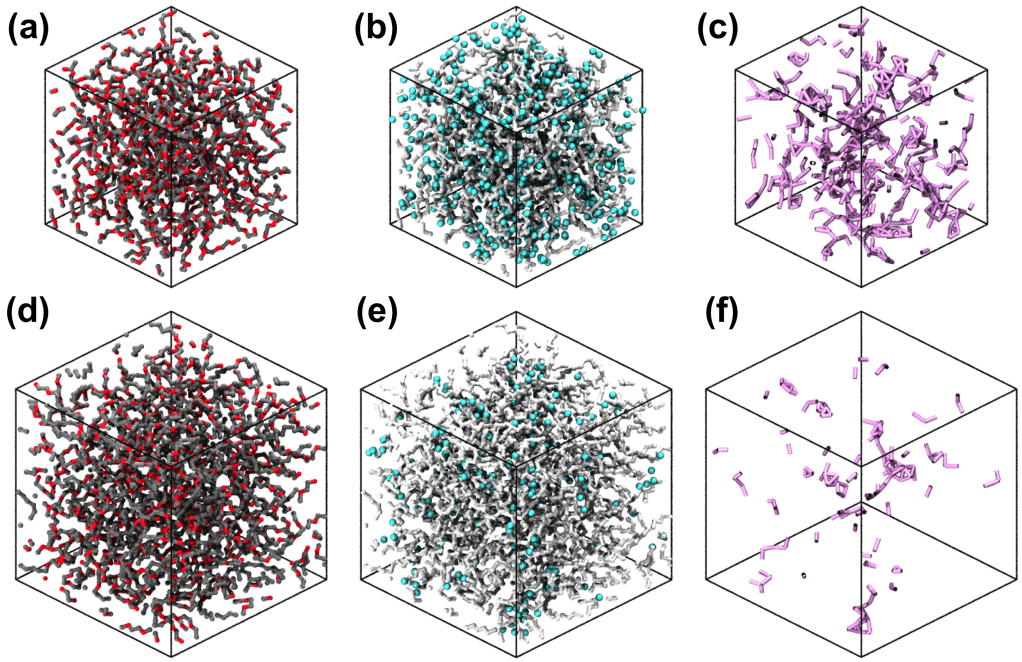

Figure 3.9: A comparison between simulation snapshots for (a-c) PEO and (d-f) C_6EO_4 showing (a, d) a representative configuration of the neat polymer melt; (b, e) possible lithium-ion solvation sites within the melt; and (c, f) edges less than 3 Å in length between the solvation sites in (b, e). In (a, d) carbon atoms are gray, and oxygen atoms are red. In (b, e), all polymer atoms are light gray while the solvation sites are depicted as blue spheres. In (c, f), edges between solvation sites are depicted as purple bonds while the polymer is not shown for clarity. The various simulation snapshots have the same size scale; the difference in size between the simulation box for PEO and that of C_6EO_4 is due to the latter having a larger number of atoms and a lower density.

Similarly, the second metric, λ (also shown in Figure 3.10a), is computed using

$$\lambda = \frac{1}{L_u} \sum_{i<j} H(r_{\text{cut}} - \sqrt{\mathbf{r}_{ij} \cdot \mathbf{u}}), \tag{3.7}$$

where Lu is the length of a given linear dimension in the simulation cell, u is a unit vector in the direction of that linear dimension, and $\sqrt{\mathbf{r}_{ij} \cdot \mathbf{u}}$ is the magnitude of the distance vector r_{ij} projected onto $\mathbf{u}$. The third metric, $\exp[-\langle r_{\text{nn}} \rangle]$ (Figure 3.10b), is expected to be proportional to a characteristic hopping rate between solvation sites separate by $\langle r_{\text{nn}} \rangle$, which is computed using

$$\langle r_{\text{nn}} \rangle = \frac{1}{N} \sum_{i} \min_{j>i} [r_{ij}], \tag{3.8}$$

where N denotes the number of solvation sites in the simulation cell. All three quantities are likely to increase if the number of sites increases or the distance between solvation sites decreases, and so each reasonably reports on the concept of connectivity.

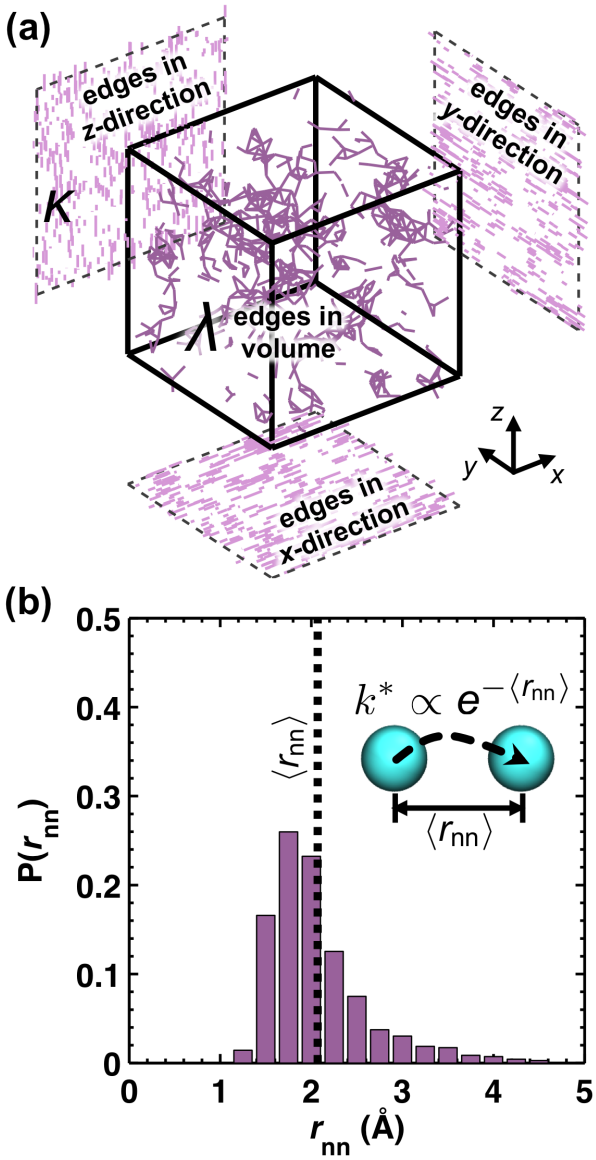

Figure 3.10: The relationship between connectivity metrics in PEO. (a) Edges between solvation sites in the simulation cell, which defines the volumetric edge density κ, and projections of the edges in the x-, y-, and z- directions, which define the linear edge density λ. (b) The distribution of nearest-neighbor separation distances, which defines the average nearest-neighbor separation distance, $\langle r_{nn} \rangle$, used to compute a characteristic hopping rate, $\exp[-\langle r_{nn} \rangle]$.

Figure 3.11 presents the dependence of all three metrics for characterizing the connectivity on x_O. All of the metrics, which are normalized with respect to PEO, increase with increasing x_O for a given linker. This is sensible because the number of consecutive EO units is increasing, making lithium-ion solvation sites more prevalent. It is interesting to note that polymers with C_6 linkers are characterized by higher connectivity than polymers with C_4 or C_2 linkers when the oxygen mole

fraction is comparable, up to x_O=0.27. This is likely because the C_6EO_y polymers require more contiguous EO units to achieve the same oxygen mole fractions as the polymers with shorter linkers.

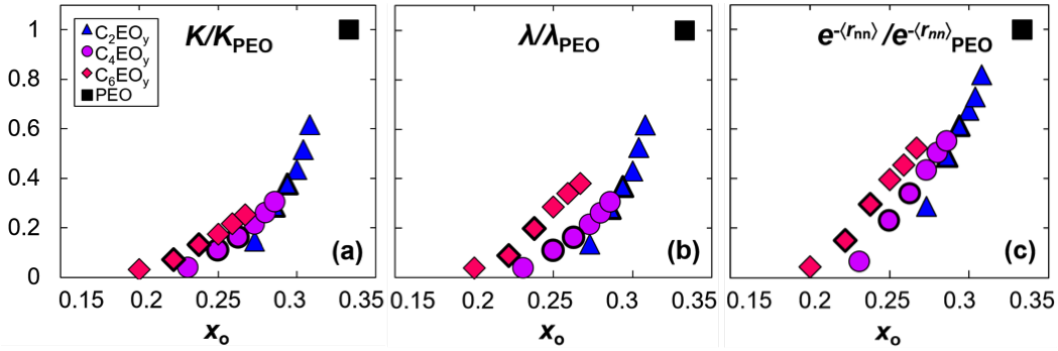

Figure 3.11: Analysis of simulated connectivity metrics as a function of x_O for polymers with different linkers, including (a) κ, the volumetric connectivity (number of edges between solvation sites per unit volume), (b) λ, the linear connectivity (number of edges between solvation sites per unit length), and (c) $\exp[-\langle r_{nn}\rangle]$, a characteristic distance-dependent proportionality for the lithium-ion hopping rate. Each metric is normalized by the corresponding value for PEO. In all panels, polymers with different linkers are denoted by different symbols. Markers with bold outlines indicate polymers that were also experimentally characterized.

3.3.c Comparison between Experiment and Simulation

Figure 3.12 directly examines the correlation between the experimentally calculated f_{exp} and the theoretically derived connectivity metrics. The linear fits shown in Figure 3.12a-c quantify the relationship between f_{exp} and connectivity. The relationships thus obtained are

$$f_{exp} = a_i + m_i C_i, \tag{3.9}$$

where C_i can be any of three connectivity metrics ($C_1 = \kappa/\kappa_{PEO}$, $C_2 = \lambda/\lambda_{PEO}$, $C_3 = \exp[-\langle r_{nn}\rangle]/\exp[-\langle r_{nn}\rangle_{PEO}]$). The fits give ($a_1 = 0.34$, $m_1 = 0.69$), ($a_2 = 0.31$, $m_2 = 0.72$), and ($a_3 = 0.30, m_3 = 0.71$). To a good approximation the relationship between f_{exp} and the connectivity metrics is linear with an intercept of 0.32 and a slope of 0.71 (average values of $a_i$and m_i, respectively). The behavior of the ether-based electrolytes in the low C_i limit remains an interesting open question. One expects that the lithium-ion diffusivity will tend to zero as C_i approaches zero, but how the anion and the mutual diffusion of the anion and cation are affected in this limit is not clear. While the data in Figure 3.12 extrapolates to a finite positive value (0.32) as C_i approaches 0, it is possible that the linear relationships in Figure 3.12 break down at $0 < C_i < 0.15$, perhaps due to a change in ion-hopping mechanism

in the low connectivity limit ($C_i < 0.15$) or due to the neglect of anion transport or ion-ion interactions in our simulations. Regardless, Figure 3.12 makes clear that f_{exp}, which is obtained from analysis of experimentally measured conductivities of a series of ether-based polymer electrolytes, is strongly correlated with the solvation-site connectivity that manifests in simulations of neat polymers. For other classes of polymers, we have found that the calculated solvation site connectivity does not necessarily correlate directly with x_O,[35] and we likewise do not expect that in general for f_{exp}; in this sense, the results in Figures 3.5 and 3.6 are likely a special feature of the class of polyethers considered here. Nonetheless, generally across polymers, we do expect a strong correlation between the experimental and calculated metrics of connectivity, as shown in Figure 3.12.

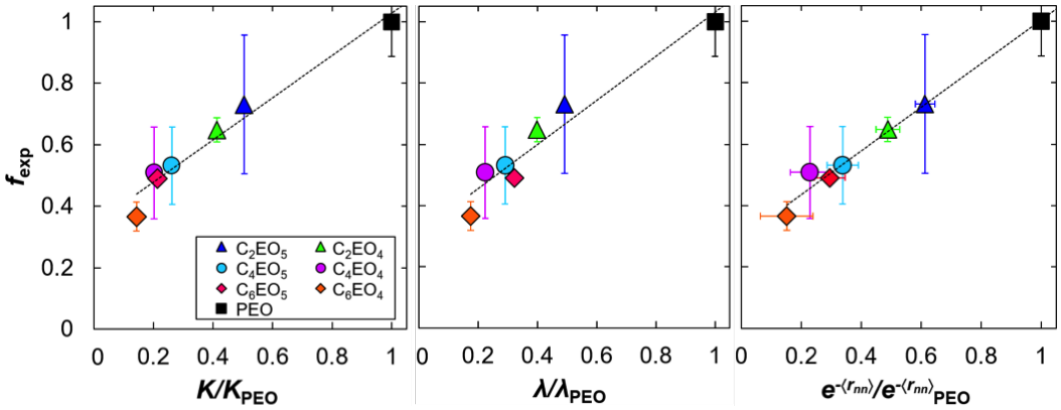

Figure 3.12: Correlation of experimental solvation-site connectivity, f_{exp}, and the theoretical connectivity metrics in Figure 3.11a-c. The dashed line shows the linear fit to the data. The correlation coefficients for the linear fits are 0.91, 0.89, and 0.98 for a-c, respectively.

3.4 Conclusions

The role of polymer segmental motion and the glass-transition temperature on the conductivity of polymer electrolytes has long been appreciated. When comparing polymers with different monomer chemistries, the nature and distribution of ion solvation sites may also play an important role. To investigate these effects, a combined experimental and computational study of ion transport is performed on a systematic set of polymer electrolytes in which aliphatic linkers have been added to a PEO backbone. Experiments are conducted on mixtures of the ether-based polymers and LiTFSI over a wide range of salt concentrations, while the simulations focus on the solvation of lithium ions in the dilute-salt limit and the distribution of available lithium-ion solvation sites in neat polymers.

The experimentally measured conductivities are affected by a variety of often com-

peting factors, including T_g and also the density of available ion solvation sites. To isolate the effects of these factors, we employ a two-step normalization scheme. In the first step, VFT fits are used to calculate a temperature-dependent reduced conductivity, $\sigma_r(T - T_g)$, which is defined as the conductivity of the electrolyte of interest at a fixed value of $T - T_g$. This step mitigates differences in the conductivity of polymers that arise due to disparities in T_g. In the second step, we compute a dimensionless parameter f_{exp}, defined as the ratio of the reduced ion mobility of the electrolyte of interest to that of a reference polymer (PEO). This parameter is used to assess to what extent changes in conductivity can be attributed to factors other than T_g, such as those due to differences in the connectivity of solvation sites. Remarkably, within the set of polyethers studied, f_{exp} is shown to depend only on oxygen mole fraction, x_O, and is largely independent of temperature and salt concentration. This suggests that f_{exp} is an intrinsic property of the neat polymer that distinguishes the conductivity of polymers at a given concentration and $T - T_g$.

Molecular dynamics simulations conducted on neat polymers and polymers in the presence of an isolated lithium ion are used to develop molecular insight for f_{exp} and its dependence on x_O. The latter simulations are used to identify the nature of lithium-ion solvation sites, and the distribution of such sites is examined in simulations of neat polymer systems. We introduce three metrics for quantifying the connectivity among solvation sites using simulation ($C_1 = \kappa/\kappa_{PEO}$, $C_2 = \lambda/\lambda_{PEO}$, $C_3 = \exp[-\langle r_{nn}\rangle]/\exp[-\langle r_{nn}\rangle_{PEO}]$). In the range $0.2 < x_O < 1$, we find that f_{exp} is correlated with the various connectivity metrics according to $f_{exp} = 0.32 + 0.71C_i$. The simulations thus provide molecular insight into the underpinnings of f_{exp}. Namely, f_{exp} reports on the proximity of lithium-ion solvation sites in the polymer, which is essential in facilitating lithium-ion diffusion in polymer electrolytes.

References

(1) Tarascon, J.; Armand, M *Nature* **2001**, *414*, 359–367.

(2) Scrosati, B.; Garche, J. *Journal of Power Sources* **2010**, *195*, 2419–2430.

(3) Meyer, W. H. *Adv. Mater.* **1998**, *10*, 439–448.

(4) Scrosati, B.; Vincent, C. A. *MRS Bulletin* **2011**, *25*, 28–30.

(5) Lascaud, S.; Perrier, M.; Vallee, A.; Besner, S.; Prud'homme, J.; Armand, M. *Macromolecules* **1994**, *27*, 7469–7477.

(6) Shi, J.; Vincent, C. A. *Solid State Ion.* **1993**, *60*, 11 –17.

(7) Gorecki, W; Jeannin, M; Belorizky, E; Roux, C; Armand, M *Journal of Physics: Condensed Matter* **1995**, *7*, 6823–6832.

(8) Borodin, O; Smith, G. *Macromolecules* **2006**, *39*, 1620–1629.

(9) Fenton, D; Parker, J; Wright, P *Polymer* **1973**, *14*, 589–589.

(10) Shriver, D; Papke, B; Ratner, M; Dupon, R; Wong, T; Brodwin, M *Solid State Ion.* **1981**, *5*, 83–88.

(11) Borodin, O.; Smith, G. D. *Macromolecules* **1998**, *31*, 8396–8406.

(12) Croce, F; Persi, L; Scrosati, B; Serraino-Fiory, F; Plichta, E; Hendrickson, M. *Electrochim. Acta* **2001**, *46*, 2457 –2461.

(13) Johansson, P.; Ratner, M. A.; Shriver, D. F. *J. Phys. Chem. B* **2001**, *105*, 9016–9021.

(14) Bruce, P. G.; Scrosati, B.; Tarascon, J.-M. *Angewandte Chemie* **2008**, *47*, 2930–46.

(15) Croce, F.; Appetecchi, G. B.; Persi, L.; Scrosati, B. *Nature* **1998**, *394*, 456–458.

(16) Bandara, L.; Dissanayake, M.; Mellander, B.-E. *Electrochimica Acta* **1998**, *43*, 1447–1451.

(17) Kim, Y. T.; Smotkin, E. S. *Solid State Ion.* **2002**, *149*, 29–37.

(18) Rhoo, H.-J.; Kim, H.-T.; Park, J.-K.; Hwang, T.-S. *Electrochimica Acta* **1997**, *42*, 1571–1579.

(19) Shin, J. H.; Henderson, W. A.; Passerini, S. *Electrochemistry Communications* **2003**, *5*, 1016–1020.

(20) Choi, B. K.; Kim, Y. W.; Shin, H. K. *Electrochimica Acta* **2000**, *45*, 1371–1374.

(21) Michael, M.; Jacob, M.; Prabaharan, S.; Radhakrishna, S *Solid State Ion.* **1997**, *98*, 167–174.

(22) Tanaka, R; Sakurai, M; Sekiguchi, H; Mori, H; Murayama, T; Ooyama, T *Electrochim. Acta* **2001**, *46*, 1709–1715.

(23) Acosta, J *Solid State Ion.* **1996**, *85*, 85–90.

(24) Khurana, R.; Schaefer, J. L.; Archer, L. A.; Coates, G. W. *J. Am. Chem. Soc.* **2014**, *136*, 7395–7402.

(25) Zhang, Z.; Jin, J.; Bautista, F; Lyons, L.; Shariatzadeh, N; Sherlock, D; Amine, K; West, R *Solid State Ion.* **2004**, *170*, 233 –238.

(26) Watanabe, M.; Hirakimoto, T.; Mutoh, S.; Nishimoto, A. *Solid State Ion.* **2002**, *148*, 399 –404.

(27) Redfern, P. C.; Curtiss, L. A. *Journal of Power Sources* **2002**, *110*, 401–405.

(28) Watanabe, M; Nagaoka, K; Kanba, M; Shinohara, I *Polym. J.* **1982**, *14*, 877–886.

(29) Watanabe, M.; Ikeda, J.; Shinohara, I. *Polymer Journal* **1983**, *15*, 65–69.

(30) Nagaoka, K.; Naruse, H.; Shinohara, I.; Watanabe, M. *Journal of Polymer Science: Polymer Letters Edition* **1984**, *22*, 659–663.

(31) Qiao, J.; Chen, Y.; Baker, G. L. *Chemistry of Materials* **1999**, *11*, 2542–2547.

(32) Buriez, O; Han, Y.; Hou, J; Kerr, J.; Qiao, J; Sloop, S.; Tian, M.; Wang, S. *J. Power Sources* **2000**, *89*, 149–155.

(33) Barteau, K. P.; Wolffs, M.; Lynd, N. A.; Fredrickson, G. H.; Kramer, E. J.; Hawker, C. J. *Macromolecules* **2013**, *46*, 8988–8994.

(34) Liu, G *Solid State Ion.* **2004**, *175*, 781–783.

(35) Webb, M. A.; Jung, Y.; Pesko, D. M.; Savoie, B. M.; Yamamoto, U.; Coates, G. W.; Balsara, N. P.; Wang, Z.-G.; Miller III, T. F. *ACS Cent. Sci.* **2015**, 198–205.

(36) Webb, M. A.; Savoie, B. M.; Wang, Z.-G.; Miller III, T. F. *Macromolecules* **2015**, *48*, 7346–7358.

(37) Sarapas, J. M.; Tew, G. N. *Macromolecules* **2016**, *49*, 1154–1162.

(38) Schmidt, B. *European Journal of Organic Chemistry* **2004**, *2004*, 1865–1880.

(39) Teran, A. A.; Tang, M. H.; Mullin, S. A.; Balsara, N. P. *Solid State Ion.* **2011**, *203*, 18–21.

(40) Wagener, K. B.; Brzezinska, K. *Macromolecules* **1991**, *24*, 5273–5277.

(41) Wagener, K. B.; Brzezinska, K.; Bauch, C. G. *Die Makromolekulare Chemie, Rapid Communications* **1992**, *13*, 75–81.

(42) Vanommeslaeghe, K.; Hatcher, E.; Acharya, C.; Kundu, S.; Zhong, S.; Shim, J.; Darian, E.; Guvench, O.; Lopes, P.; Vorobyov, I.; Mackerell, A. D. *J. Comput. Chem.* **2010**, *31*, 671–690.

(43) Stubbs, J. M.; Potoff, J. J.; Siepmann, J. I. *J. Phys. Chem. B* **2004**, *108*, 17596–17605.

(44) Wu, H.; Wick, C. D. *Macromolecules* **2010**, *43*, 3502–3510.

(45) Plimpton, S. *J. Comp. Phys.* **1995**, *117*, 1 –19.

(46) Brown, W. M.; Wang, P; Plimpton, S. J.; Tharrington, A. N. *Comput. Phys. Commun.* **2011**, *182*, 898–911.

(47) Brown, W. M.; Kohlmeyer, A.; Plimpton, S. J.; Tharrington, A. N. *Comput. Phys. Commun.* **2012**, *183*, 449–459.

(48) Figueirido, F.; Del Buono, G. S.; Levy, R. M. *The Journal of chemical physics* **1995**, *103*, 6133.

(49) Maitra, A.; Heuer, A. *Phys. Rev. Lett.* **2007**, *98*.

(50) Diddens, D.; Heuer, A.; Borodin, O. *Macromolecules* **2010**, *43*, 2028–2036.

(51) Nitzan, A; MA, R. *J. Phys. Chem.* **1994**, *98*, 1765–1775.

(52) Devaux, D.; Bouchet, R.; Glé, D.; Denoyel, R. *Solid State Ion.* **2012**, *227*, 119–127.

(53) Pesko, D. M.; Jung, Y.; Hasan, A.; Webb, M. A.; Coates, G. W.; Miller III, T. F.; Balsara, N. P. *Solid State Ion.* **2016**, *289*, 118–124.

(54) Chintapalli, M.; Chen, X. C.; Thelen, J. L.; Teran, A. A.; Wang, X.; Garetz, B. A.; Balsara, N. P. *Macromolecules* **2014**, *47*, 5424–5431.

(55) Müller-Plathe, F; Vangunsteren, W. *J. Chem. Phys.* **1995**, *103*, 4745–4756.

Chapter 4

CHEMICALLY SPECIFIC DYNAMIC BOND PERCOLATION MODEL FOR ION TRANSPORT IN POLYMER ELECTROLYTES

Chapter 2 provided the foundation for solvation-site connectivity as a polymer-specific property that plays an essential role for ion transport in polymer electrolytes. Meanwhile, in Chapter 3, we demonstrated a direct correspondence between experimental conductivity and solvation-site connectivity, resulting in an equation that would facilitate predictions of conductivity for a particular class of polymers. This success invites us to speculate on how the conceptual notion of solvation-site connectivity might be leveraged as a general predictive tool for polymer electrolyte performance.

In this chapter, we introduce a coarse-grained approach for characterizing the long-timescale dynamics of ion diffusion in general polymer electrolytes using input from short molecular dynamics trajectories. The approach includes aspects of the dynamic bond percolation model [*J. Chem. Phys.* **1983**, 79, 3133-3142] by treating ion diffusion in terms of hopping transitions on a fluctuating lattice. We extend this well-known approach by using short (i.e., 10 ns) molecular dynamics (MD) trajectories to predict the distribution of ion solvation sites that comprise the lattice and to predict the rate of hopping among the lattice sites. This yields a chemically specific dynamic bond percolation (CS-DBP) model that enables the description of long-timescale ion diffusion in polymer electrolytes at a computational cost that makes feasible the screening of candidate materials. We employ the new model to characterize lithium-ion diffusion properties in six polyethers that differ by oxygen content and backbone stiffness: poly(trimethylene oxide), poly(ethylene oxide-alt-trimethylene oxide), poly(ethylene oxide), poly(propylene oxide), poly(ethylene oxide-alt-methylene oxide) and poly(methylene oxide). Good agreement is observed between the predictions of the CS-DBP model and long-timescale atomistic MD simulations, thus providing validation of the model. Among the most striking results from this analysis is the unexpectedly good lithium-ion diffusivity of poly(trimethylene oxide-alt-ethylene oxide) by comparison to poly(ethylene oxide), which is widely used. Additionally, the model straightforwardly reveals a range of polymer features than lead to low lithium-ion diffusivity, including the competing effects of the density of solvation sites and polymer stiffness. These results illustrate

the potential of the CS-DBP model to screen polymer electrolytes on the basis of ion diffusivity and to identify important design criteria.

Data and content in this chapter have been published as M.A. Webb, B.M Savoie, Z.-G. Wang and T.F. Miller III. "Chemically Specific Dynamic Bond Percolation Model for Ion Transport in Polymer Electrolytes." *Macromolecules*, **48**, 7346-7358 (2015).

4.1 Introduction

Rechargeable lithium-ion batteries are important for many technological applications.[1] Since the discovery that polyethers like poly(ethylene oxide) (PEO) provide an ion-conducting medium,[2,3] there has been interest in developing solid polymeric electrolytes as a replacement for liquid electrolytes for safe, stable, and cost-effective batteries.[4,5] However, the ionic conductivities of such materials remain insufficient for many practical applications, despite research focus on both the synthesis of novel polymers[6–14] and additives.[15,16] Indeed, the most studied and widely employed polymer electrolytes continue to be based on PEO.[17–33] The design of more conductive polymer electrolytes requires both a better understanding of ion-transport mechanisms in polymers as well as the development of tools for screening candidate polymers prior to synthesis and characterization.

Molecular simulation provides a powerful tool for studying ion transport in polymers, for predicting transport properties, and for developing design principles based on mechanistic insight. Significant theoretical and computational effort has been devoted to the study of ion conduction in PEO and PEO-based systems.[34–48] Through these efforts, a number of transport mechanisms in PEO-based polymers have been identified, including both intra- and inter-segmental hopping events, as well as the co-diffusion of cations and polymer chains.[38,49] However, even long molecular dynamics (MD) trajectories (i.e., in excess of 100 ns) may reveal only a small number of the rare events associated with ion transport and may not report on the diffusive regime,[48] thus necessitating the development of less computationally intensive theoretical models to study ion transport properties in other polymers.

A number of theories and models have been developed for ion transport in amorphous polymers.[38,50–54] Some models based on the specific mechanisms of ion transport observed in PEO[38,54] have been successfully applied in several PEO-based electrolyte systems[38,49,54–57]. However, these models are not immediately generalizable to other polymers, which can exhibit different ion transport mechanisms,[48]

and they require long (up to 700 ns)[56] MD trajectories to determine necessary model parameters. In contrast, the dynamical bond percolation (DBP) model[50–53] provides a general, phenomenological approach that treats ion transport in terms of hopping transitions on a fluctuating lattice. Although this framework is quite general, the DBP model has been practically implemented with a number of simplifying assumptions, including that the array of sites is uniform and that the hopping rate is identical among all neighboring sites;[53] as such, the DBP model has been limited to the description of generic aspects of ion diffusion in polymers,[50–53,58,59] rather than addressing detailed aspects of specific polymer systems. Another possible approach is the trajectory-extending kinetic Monte Carlo (TEKMC) method, which extrapolates transport properties based on the construction of a transition matrix with statistics generated from MD trajectories.[45,47,60] Although TEKMC can be used to obtain long-timescale diffusion coefficients from shorter trajectories, it is not directly connected to an underlying model for ion transport in polymer electrolytes, which would be useful for future polymer design. We aim to build upon this earlier work by establishing a framework for ion transport that is both computationally tractable and generally applicable to a wide range of polymer classes, while also incorporating sufficient chemical specificity to enable the identification of promising candidate polymers for ion-transport applications.

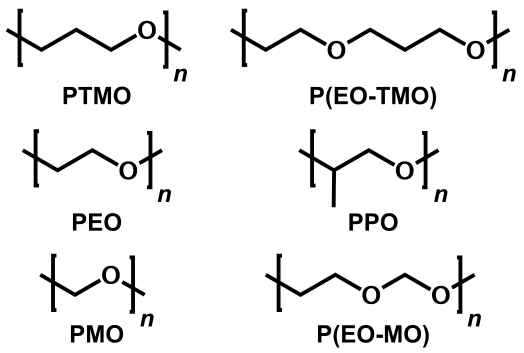

Figure 4.1: Polymers considered in this chapter.

In this paper, we present a chemically specific DBP (CS-DBP) model for ion transport in polymer electrolytes. We begin by presenting MD simulations of lithium-ion transport in PEO to illustrate general features of ion transport in polymers. These features are then distilled into a framework in which ion diffusion occurs via hopping transitions on a dynamical network of ion solvation sites. In the CS-DBP model, the hopping rates depend on the distribution and connectivity of solvation sites, which are obtained from short-timescale (1-10 ns) MD trajectories and which account

for the effects of detailed molecular properties of the polymer, such as monomer topology, composition, and flexibility. The model is employed to predict the rate of lithium-ion diffusion in a range of polymers, including poly(trimethylene oxide), poly(ethylene oxide-alt-trimethylene oxide), poly(ethylene oxide), poly(propylene oxide), poly(ethylene oxide-alt-methylene oxide) and poly(methylene oxide). For the remainder of the chapter, these polymers are referred to respectively as PTMO, P(EO-TMO), PEO, PPO, P(EO-MO), and PMO as indicated in Figure 4.1. The CS-DBP model predictions are compared to those of long-timescale MD simulations of lithium-ion transport in the same polymers to evaluate the performance of the new model.

4.2 Characteristics of Ion Transport in Polymers

In this section, atomistic MD simulations of lithium-ion diffusion in PEO are used to illustrate fundamental mechanistic features of ion transport in polymers and to motivate the development of the CS-DBP model in the following sections. Four independent MD trajectories of a single lithium cation diffusing in PEO at 400 K and 1 atm are each run for 300 ns, following system preparation and equilibration. To simulate diffusion in a high-molecular-weight polymer, to mitigate potential artifacts associated with ends of the polymer chains, and to suppress co-diffusion of the lithium cation with the polymer chain (i.e., rafting), a single PEO chain with 640 monomer units (approximately 29,000 g/mol) is used as the electrolyte solvent. Full details regarding the simulation methodology are provided in Section 4.4.a.

Figures 4.2A and 4.2B feature trajectory snapshots that illustrate inter- and intra-segmental hopping events of the lithium cation. For the inter-segmental hopping event depicted in Figure 4.2A, the lithium cation is initially coordinated by six oxygen atoms from a single contiguous polymer chain segment (i.e., an unbroken sequence of adjacent monomers). Two oxygen atoms that initially coordinate the lithium cation are then exchanged for two others from nonadjacent monomers, such that, after the hopping event, the lithium cation is coordinated by oxygens from two different chain segments. For the intra-segmental hopping event depicted in Figure 4.2B, the lithium cation is again initially coordinated by six oxygen atoms from a single contiguous chain segment. A torsional flip at the end of this segment breaks the contact between the lithium cation and one oxygen, allowing the lithium cation to form a new coordinating contact with an oxygen on a monomer that is adjacent to the original chain segment. After this intra-segmental hop, the lithium cation remains coordinated by oxygens that form a single contiguous chain segment;

the lithium cation has effectively "slid" along the backbone of the PEO chain. Both inter- and intra-segmental hopping events have been discussed in the context of PEO,[34–38,41–43,48,50,51] and we also discussed them in a range of different polymers in Chapter 2.

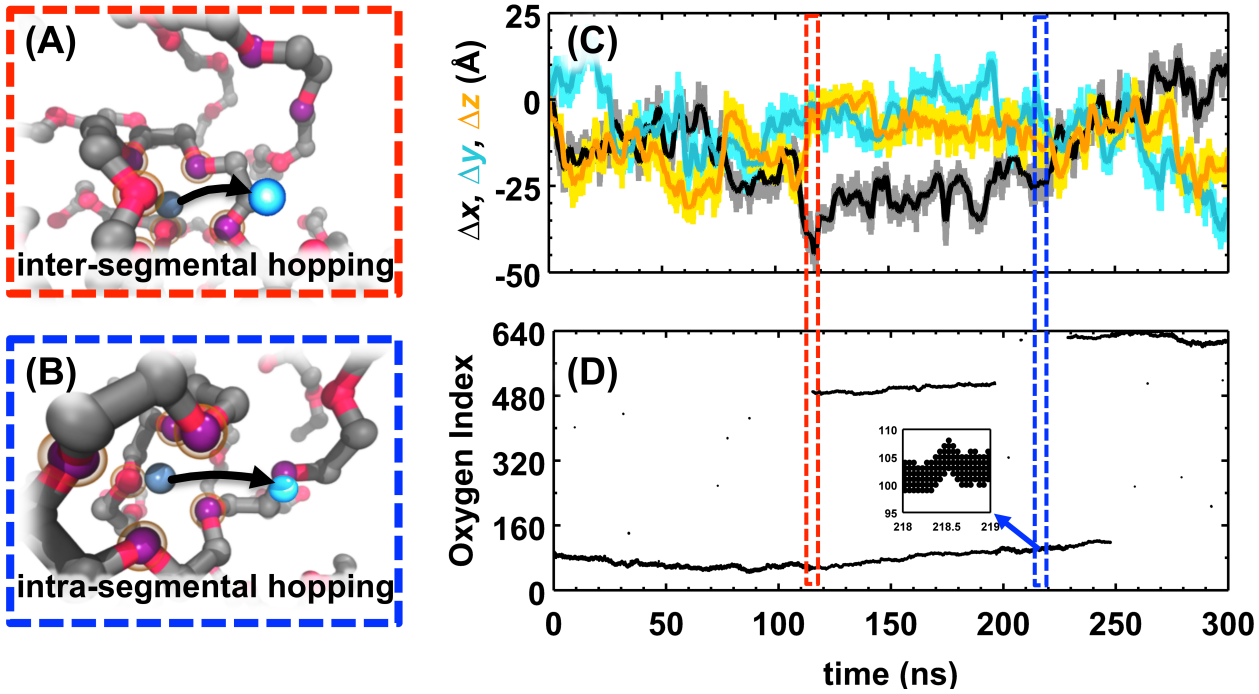

Figure 4.2: MD analysis of lithium-ion diffusion in PEO. (A) A simulation snapshot of an inter-segmental hopping event. (B) A simulation snapshot of an intra-segmental hopping event. In both (A) and (B), the lithium cation is shown in green, and an arrow indicates the direction to the lithium-ion position after the event. The orange rings indicate oxygen atoms present in the initial lithium-ion solvation shell; the color purple indicates oxygen atoms present in the final lithium-ion solvation shell. (C) Lithium-ion displacement from initial position as a function of time. The shaded regions correspond to instantaneous position while the darker lines correspond to average positions over a 50 ps time interval. (D) Lithium-ion coordination environment as a function of time. All oxygen atoms are numbered sequentially from the beginning of the polymer chain. Markers are placed for oxygen atoms that are within 3.25 Å of the lithium cation for at least 25 ps of a 50 ps time interval.

Figures 4.2C and 4.2D reveal how hopping events like those depicted in Figures 4.2A and 4.2B lead to changes in the lithium-ion coordination environment and position during a simulation trajectory. In Figure 4.2C, the lithium cation is monitored by tracking its net displacement (Δx, Δy, and Δz) as a function of simulation time. The lithium-ion motion is characterized by local fluctuations on the 1-10 ns timescale, interspersed with larger displacements that occur on the 10-100 ns timescale. In Figure 4.2D, the lithium-ion coordination environment is monitored by tracking the oxygen atoms in the first lithium-ion solvation shell; specifically, each PEO oxygen atom is sequentially labeled according to its position in the polymer chain (oxygen-1 and oxygen-640 are at the two endpoints of the polymer chain), and markers are plotted for oxygen atoms that are within 3.25 Å of the lithium cation for at least half of a given 50 ps time interval. The figure inset shows that four to seven oxygen atoms (from one or two chain segments) typically coordinate the lithium cation at any given time, which is consistent with previous studies of lithium-ion transport in PEO-based polymers.[34–38,41–44,48] Here, a drift in oxygen indices is indicative of the lithium-ion hopping to adjacent monomer units, as in the event depicted in Figure 4.2B, which occurs in the blue-boxed time interval. Alternatively, the appearance or disappearance of lines in Figure 4.2D is indicative of the lithium-ion hopping to nonadjacent parts of the polymer chain, as in the event depicted in Figure 4.2A, which occurs in the red-boxed time interval. Similar events of this type are observed at around 198 ns and 228 ns in this particular MD trajectory.

Although the two molecular events highlighted in Figure 4.2 are typically regarded as distinct ion-transport mechanisms, they have common features that suggest a more general view of ion transport in polymers.[48] In particular, both events involve a hopping transition between ion solvation sites that is accompanied by both reorganization of the polymer environment and exchange of atoms that directly coordinate the ion. In the following section, we develop a model for ion transport in polymers that incorporates this more general view of lithium-ion diffusion mechanisms in polymers.

4.3 Chemically Specific Dynamic Bond Percolation Model

4.3.a Overview of Model Strategy

In this section, we present a chemically specific dynamic bond percolation (CS-DBP) model for ion transport in polymers. Figure 4.3 illustrates the overall strategy for calculating lithium-ion transport properties in polymers from a small number (less than five) of short-timescale (10 ns) MD trajectories using the CS-DBP model, in con-

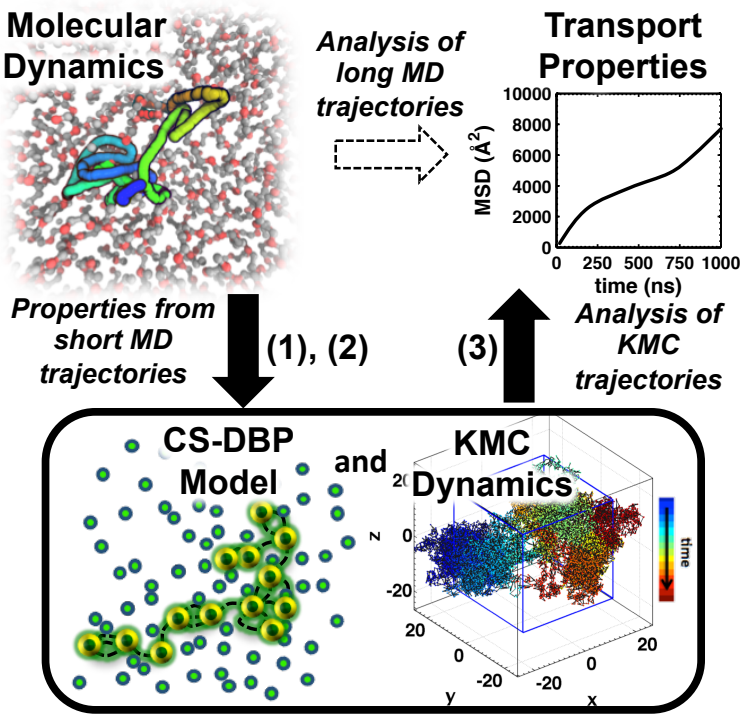

Figure 4.3: Alternative strategies for obtaining ion-transport properties in polymers. The dashed arrow indicates the conventional brute-force approach, in which transport properties are obtained by running long and computationally expensive MD trajectories. The black arrows indicate the approach of the CS-DBP model, in which short MD trajectories are used to obtain parameters for kinetic Monte Carlo simulations that predict transport properties at reduced computational cost.

trast to performing computationally expensive, microsecond-timescale trajectories that are needed to directly simulate ion transport in polymers using MD. Obtaining transport properties from the CS-DBP model consists of three main stages. We first briefly describe each stage and then elaborate on them in the following sections.

In stage (1), polymer configurations taken from short MD simulations are scanned to find viable ion solvation sites in the polymer on the basis of the arrangement of lithium-coordinating atoms, such as oxygen atoms in PEO. Details of the solvation sites and the site-identification protocol are provided in Section 4.3.b.

In stage (2), properties obtained from short MD simulations are used to estimate hopping rates between the lithium-ion solvation sites found in stage (1). Details of the transition-rate expression and the relevant quantities are provided in Section 4.3.c.

In stage (3), the solvation sites and hopping rates obtained in the previous two stages are used in kinetic Monte Carlo (KMC) simulations to study long-timescale lithium-ion diffusion properties in the polymer. Details of the KMC simulations are

provided in Section 4.3.d.

The strategy outlined incorporates system-specific details in a DBP framework. As such, this approach could also be applied to study various particle transport phenomena in disordered media, while simultaneously including important atomistic details for system specificity; however, here, we focus on lithium-ion transport in polymers.

4.3.b Solvation Site Identification

As outlined in Section 4.3.a, the first stage in the CS-DBP model is to identify lithium-ion solvation sites. Lithium-ion solvation sites are identified in three steps for a given polymer configuration, as depicted in Figure 4.4.

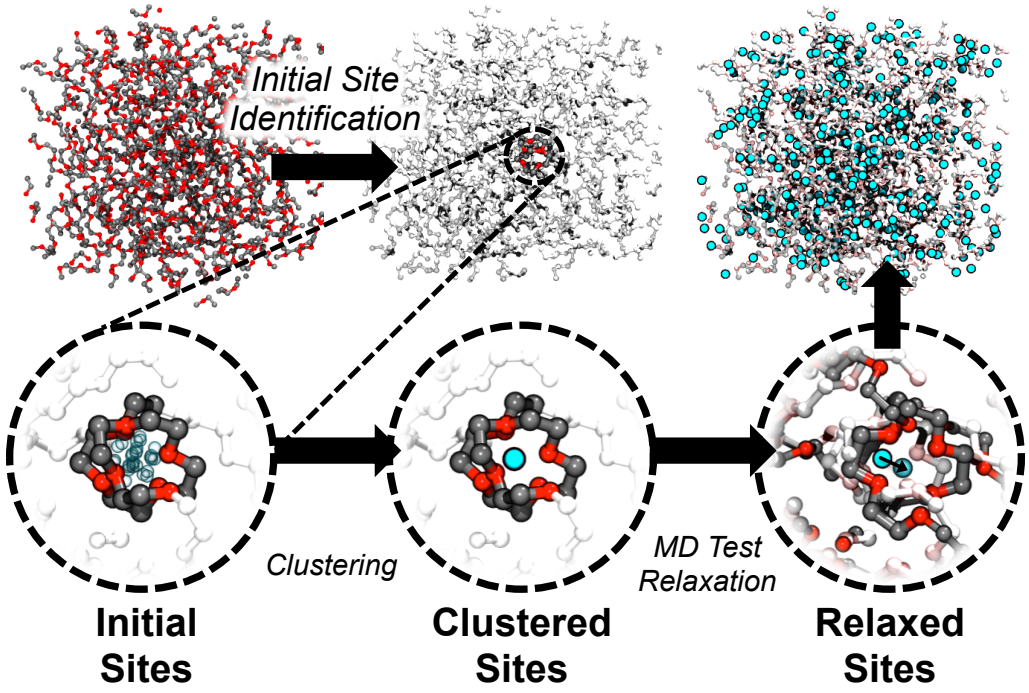

Figure 4.4: The protocol for finding lithium-ion solvation sites. Starting from a polymer configuration, a geometric search enables the identification of initial sites (blue rings). Clustering is used to eliminate sites with significant spatial overlap, which then yields clustered sites (filled blue circles). MD simulations are run with a lithium cation placed at the position of the clustered sites to determine if the site survives polymer relaxation, yielding the relaxed sites.

First, the polymer configuration is scanned to find sets of oxygen atoms that resemble a lithium-ion solvation shell. In particular, a solvation site is identified at the centroid of a set of oxygen-atom positions that fall within a threshold distance of the centroid. Here, the threshold distance is the size of the first lithium-ion solvation shell (the

distance to the first minimum of the lithium-oxygen radial distribution function). The sites identified in this step are termed "initial sites."

Second, initial sites are clustered to identify spatially distinct sites. Specifically, initial sites are clustered into a single site if the distance between them is less than the van der Waals radius of the lithium cation,[42] $\sigma_{\mathrm{Li}} = 1.4$ Å; the position of the clustered site is at the centroid of its constituent initial sites. An additional check confirms that no set of oxygen atoms associated with one clustered site is a subset of the oxygen atoms associated with another, such that all sites correspond to a unique list of associated oxygen atoms.

Third, the stability of each clustered site is tested using short MD trajectories. Specifically, a lithium cation is placed at the coordinates of the clustered site, and multiple picosecond-timescale MD trajectories are run from this configuration using randomized initial velocities. If the oxygen atoms associated with the clustered site remain within the first lithium-ion solvation shell, then the site is kept; otherwise it is discarded. The sites remaining after this step are termed "relaxed sites."

Solvation site densities and distribution functions are then calculated using the relaxed sites. For a given pair of particle types (either atoms or sites), we compute the pair number distribution function (NDF)

$$n_{\alpha\beta}(r) = \frac{1}{N_\alpha}\Big\langle \sum_{i\in\alpha}\sum_{j\in\beta} \delta(r - ||\mathbf{r}_i - \mathbf{r}_j||)\Big\rangle, \tag{4.1}$$

and the associated pair radial distribution function (RDF)

$$g_{\alpha\beta}(r) = \frac{V}{N_\beta} n_{\alpha\beta}(r), \tag{4.2}$$

where r is a given separation distance, $\mathbf{r}_k$ is the position vector of particle k, $\delta(\cdots)$ is the Dirac delta function, V is the volume of the periodic simulation cell, $||\cdots||$ denotes the Euclidean distance, and $\langle\cdots\rangle$ denotes an average over an ensemble of configurations.

Although the protocol has been discussed for the case in which oxygen atoms are the coordinating atoms, the protocol is easily generalized to account for the possibility that other atom types (such as nitrogen or sulfur) coordinate the lithium cation.

4.3.c Transition Rates Between Solvation Sites

As outlined in Section 4.3.a, the second stage in the CS-DBP model is to estimate the rate of lithium-ion hopping between solvation sites. During a hopping event

between solvation sites, a lithium cation exchanges at least one coordinating atom and translates some distance in the polymer medium. In principle, MD simulations could be used to calculate the classical mechanical rate associated with the hopping transition; however, such calculations are computationally intensive,[61] and would prohibit most materials-screening applications of the model. Instead, we propose a simple transition state theory expression for the hopping rates that uses information that is accessible from short-timescale MD trajectories. In particular, the rate constant k_0 associated with hopping between solvation sites that are separated by a distance r is

$$k_0(r) = \tau^{-1} e^{-\beta E_{\mathrm{dis}}(r)} e^{-\beta E_{\lambda}(r)}, \tag{4.3}$$

where $\beta = 1/k_{\mathrm{B}}T$ is the inverse thermodynamic temperature, τ^{-1} is an attempt frequency related to the timescale on which an ion collides with its solvation shell, $E_{\mathrm{dis}}(r)$ is a dissociation energy related to the lithium-oxygen contacts that are broken during the hop, and $E_{\lambda}(r)$ is a reorganization energy related to the polymer rearrangement that facilitates the displacement of the lithium cation. Eq. (4.3) is of the same form as that originally proposed for DBP[50], except that we explicitly partition the activation energy into $E_{\mathrm{dis}}(r)$ and $E_{\lambda}(r)$. Each term in Eq. (4.3) corresponds to a feature of the underlying physical process but is accessible from short MD simulations.

Since the attempt frequency τ in eq. (4.3) corresponds to the timescale for attempting a transition between solvation sites, it is approximated as twice the time of the first zero in the lithium-ion velocity autocorrelation function (VACF), which corresponds to the period of oscillation of the lithium cation in its solvation shell and occurs on the picosecond timescale.

The dissociation energy $E_{\mathrm{dis}}(r)$ in Eq. (4.3) is calculated as the work required to replace favorable lithium-oxygen interactions in the solvation shell with corresponding bulk-type interactions. In practice, we obtain this from the reversible work theorem,[62] which relates the potential of mean force between two particles to the corresponding pair RDF. For a lithium-oxygen interaction, this gives

$$E^0_{\mathrm{dis}} = k_{\mathrm{B}}T \ln\left[g_{\mathrm{Li,O}}(r_p)\right], \tag{4.4}$$

where r_p is distance of separation associated with the first peak of the pair RDF, $g_{\mathrm{Li,O}}(r)$. The distance-dependent $E_{\mathrm{dis}}(r)$ is subsequently computed using

$$E_{\mathrm{dis}}(r) = z(r) E^0_{\mathrm{dis}}, \tag{4.5}$$

where $z(r)$ is the site-overlap function, which reports the number of lithium cation-oxygen atom interactions that are broken, on average, for hopping events of length r.

The reorganization energy $E_\lambda(r)$ in Eq. (4.3) corresponds to the work required to create a cavity with volume large enough for the lithium cation to move between two solvation sites. Specifically, we assume that $E_\lambda(r) = M v_{\text{act}}(r)$, where M is an energy density and v_{act} is an activation volume, which is a form that appears in the treatment of various activated-hopping processes.[63–67] In the theory of small-lengthscale hydrophobic solvation, the free energy associated with spontaneous cavity formation is proportional to density fluctuations in the liquid and the cavity volume.[68–71] Similarly, we approximate M using the bulk modulus, which is proportional to density fluctuations in the polymer, and v_{act} is calculated as the volume of a cylinder with a cross-sectional area equal to that of the lithium cation, such that

$$E_\lambda(r) = B\pi\sigma_{\text{Li}}^2 r, \tag{4.6}$$

where B is the bulk modulus of the polymer. We note that Eq. (4.6) is one of multiple possible estimates for the reorganization energy, but it provides a simple and physically reasonable relation that is easily accessible from short MD simulations.

4.3.d Kinetic Monte Carlo

As outlined in Section 4.3.a, the final stage in the CS-DBP algorithm is to model the lithium-ion dynamics on the network of solvation sites. Given the distribution of lithium-ion solvation sites (Section 4.3.b) and the hopping rates between them (Section 4.3.c), KMC simulations[72–75] are used to predict lithium-ion diffusivities in polymers. At each time step of a KMC trajectory, the lithium cation occupies a solvation site, and one of two types of moves is allowed. The first type involves hopping of the lithium cation to another available solvation site; each transition to a site has an associated rate, which is given by Eq. (4.3). The second type is a complete "refresh" of the site network, in which case the existing distribution of sites to which a lithium cation can hop is replaced by a new distribution. Here, the timescale for refreshing the site network is governed by the rate ν, which is based on the characteristic lifetime of solvation sites. After a move is selected, time is evolved according to the residence-time algorithm[73],

$$t_k = t_{k+1} + \frac{\ln(1/u)}{\nu + \sum_{i=1}^{N} k_0^{(i)}}, \tag{4.7}$$

where t_k denotes the time after the kth KMC step, u is a uniform random number from 0 to 1, N is the number of available solvation sites, and $k_0^{(i)}$ is the rate constant given by Eq. (4.3) associated with a hopping transition to the ith site. Technical details regarding the KMC simulations are provided in Section 4.4.b.

4.4 Calculation Details

The lithium-ion transport characteristics are assessed in the six polymers shown in Figure 4.1 using the CS-DBP model and long-timescale MD simulations. A description of the MD simulations is given in Section 4.4.a. Model inputs for the CS-DBP model are obtained using short segments taken from the beginning of the MD production runs, as described in Section 4.4.b. Details regarding the KMC simulations are provided in Section 4.4.c.

4.4.a Molecular Dynamics Simulation Details

All polymers are simulated using a united-atom description with bonding parameters taken from the CHARMM[76] force field and all other parameters taken from the TraPPE-UA force field;[77] compatible lithium-ion parameters are obtained from previous simulation studies.[42] Although polarizable force fields have been shown to be quantitatively more accurate for simulating ion dynamics in polymer electrolytes in some cases,[78] our primary interest is the relative performance of polymer electrolytes rather than a quantitative comparison to experiment; furthermore, we note that the CS-DBP model depends mostly on neat-polymer properties or static distribution functions, for which non-polarizable force fields are expected to be sufficiently accurate. Regardless, the use of polarizable force fields in the CS-DBP model would be straightforward.

All MD simulations are performed using the LAMMPS simulation package[79] with GPU acceleration.[80,81] The equations of motion are evolved using the velocity-Verlet integrator with a 1 fs time step. Particle-particle-particle-mesh Ewald summation[81] is used to compute non-bonded interactions beyond a 14 Å cutoff for all periodic simulations. A Nosé-Hoover thermostat (100 fs relaxation) and barostat (1000 fs relaxation) are used to control the temperature and pressure, unless otherwise noted.

Four independent copies of the simulation cell are generated for each polymer studied. Each copy consists of a single long polymer chain ($M_n \approx 30,000$ g/mol) and a single lithium cation to mimic a high-molecular-weight polymer electrolyte in the dilute-ion limit. Because no explicit anion is included, the system is neutralized with a uniform background charge.[82] Initial polymer chain configurations are generated

via a self-avoiding random walk according to the rotational isomeric state approximation,[83] and the lithium cation is placed randomly in the polymer-containing simulation cell.

To generate starting configurations for MD production runs, the systems are equilibrated in five steps. In step (1), the initial configuration is relaxed for 10,000 steps with non-periodic boundary conditions using steepest descent energy minimization with the maximum atom displacement limited to 0.1 Å for any given step. In step (2), the system is annealed at 1000 K with periodic boundary conditions using 100,000 steps of Langevin dynamics with a 100 fs damping factor. In step (3), the simulation cell is adjusted at a constant rate over 500 ps at 500 K to achieve a cubic simulation cell with a density of 1.0 g/cm^3. In step (4), the system is annealed for 1.5 ns at 500 K and 1 atm. In step (5), the system is equilibrated for 25 ns at 400 K and 1 atm. Despite being prepared in an amorphous state, we find that the structures of PTMO and PMO exhibit significant orientational order upon equilibration; this result is reproducible across various initialization protocols; we note that this propensity towards ordering does not prevent the comparison of results from the CS-DBP model and results from MD simulations.

For each polymer system, a single average density is computed after step (5) by averaging the last 5 ns of the trajectories. Using this fixed density, NVT production runs of 300 ns are performed at 400 K.

4.4.b CS-DBP Model Calculation Details

To obtain the lithium-oxygen NDF, the first 10 ns of each production run is used to compute the ensemble average in Eq. (4.1); the RDF is then obtained using Eq. (4.2).

To obtain the site-site NDF and RDF, polymer configurations are taken after 5, 10, and 15 ns from each MD production run (a total of twelve configurations for each polymer system). In each configuration, initial sites are identified at the centroid of sets of three oxygen-atom positions. Clustering proceeds as in Section 4.3.b to identify clustered sites that have at least four oxygen atoms. To test the stability of each clustered site, four MD trajectories are run for 5 ps at 400 K with different randomized initial velocities. Sites that have had four or more oxygen atoms present in the first lithium-ion coordination shell for at least 80% of the last 4 ps are used as relaxed sites. The coordinates of the relaxed sites are used to compute the NDF and RDF for lithium-site and site-site pairs using Eqs. (4.1) and (4.2).

To obtain the site-overlap function, $z(r)$ in Eq. (4.5), the twelve configurations with

relaxed sites are used to compute a histogram of the overlap between two sets of oxygen atoms associated with different relaxed sites at a given distance from one another. Specifically, the overlap between two sites i and j separated by distance r is computed using

$$z_{ij}(r) = |\mathbb{S}_i - \mathbb{S}_j|, \tag{4.8}$$

where $\mathbb{S}_i$ and $\mathbb{S}_j$ denote the sets of associated oxygen atoms, $\mathbb{S}_i - \mathbb{S}_j$ is the relative complement of $\mathbb{S}_j$ in $\mathbb{S}_i$, and $|\cdots|$ reports the number of elements in the set. Then, $z(r)$ is calculated as $\langle z_{ij}(r)\rangle$, which is averaged over all pairs at a given distance r and over all polymer configurations. Occasionally no samples are obtained for $z_{ij}(r)$, in which case $z(r)$ is linearly interpolated between the two nearest nonzero entries in the histogram.

To obtain the attempt frequency, τ, the VACF of the lithium cation is computed from the first 1 ns of each production run. The time at the first zero of the VACF is obtained by linear interpolation.

To obtain the bulk modulus, B, initial configurations for the production runs are copied, and the lithium cation is removed. MD trajectories are run for these neat-polymer systems at 400 K and 1 atm for 10 ns to obtain statistics on the relative volume fluctuations in the NPT-ensemble, which are used to compute B.[84]

To obtain the polymer-specific site-refresh rate, ν, a continuous indicator function $h_i(t) \in (0, 1]$ is defined that reports on the extent to which any site spatially overlaps with a given site i after time t. A relaxation time for $h_i(t)$ is then computed using the normalized site autocorrelation function,

$$\mathrm{SACF}(t) = \frac{\langle h_i(t)h_i(0)\rangle - \langle h_i(t \to \infty)h_i(0)\rangle}{1 - \langle h_i(t \to \infty)h_i(0)\rangle}, \tag{4.9}$$

which yields a relaxation time via

$$\tau_{\mathrm{site}} = \int_0^\infty \mathrm{SACF}(t)dt, \tag{4.10}$$

and finally the site-refresh rate via $\nu = \tau_{\mathrm{site}}^{-1}$. Here, a single relaxation time is used to characterize ν, which is consistent with the implementation of a "renewal time" in the original DBP model;[50] however, this implementation could easily be generalized to account for a distribution of site-refresh rates due to the internal modes of the polymer. In practice, Eq. (4.9) is calculated using the coordinates of the clustered sites that are found between 1.5 Å and 2.5 Å of the lithium cation, which are easily extracted as a function of time from the trajectories, and the integral in Eq. (4.10)

is performed by fitting the results to a stretched exponential function. Note that the choice to use the stretched exponential fit is purely based on mathematical convenience; in the approximation of a single relaxation time, the specific form of SACF(t) is unimportant since only its integral is needed. The first 10 ns of each production run are used for ensemble averaging.

4.4.c Kinetic Monte Carlo Simulation Details

For each polymer, 160 independent KMC trajectories are run until the simulation time reaches 5 μs or until 2.5×10^6 KMC moves have been performed. Explicit site networks are modeled with cubic periodic boundary conditions and 512 sites per periodic cell; the side length of the simulation cell is adjusted to match the average site density obtained from the twelve MD configurations used to identify lithium-ion solvation sites (Section 4.4.b). Prior to each KMC trajectory, iterative Boltzmann inversion[85] (IBI) is used to obtain five realizations of the site network that reflect the site-site RDFs obtained from the MD configurations. In the KMC moves associated with refreshing the site network, three steps are performed. First, one of the five realizations is randomly chosen. Second, the orientation of the chosen network is randomized by applying (with equal probability) a 0°, 90°, 180°, or 270° rotation about the x-, y-, and z-axis, in random order. Third, the simulation cell is shifted such that a randomly selected site coincides with the coordinates of the lithium cation.

4.5 Results

In this section, we illustrate the application of the CS-DBP model to the set of polyethers in Figure 4.1. Additionally, the results of the CS-DBP model are compared to those of long-timescale atomistic MD simulations.

4.5.a Site Distributions

We begin by demonstrating the implementation of stage (1) of the CS-DBP model, in which the solvation-site distribution functions are obtained. Figure 4.5A illustrates the solvation sites in a representative MD configuration for each polymer considered in this study. As expected, polymers with less oxygen content are typically populated with fewer sites, such that PTMO exhibits the smallest number of solvation sites and PMO exhibits the largest. Interestingly, PPO has more sites than PTMO, even though the ratio of carbon to oxygen atoms is 3:1 in both cases; this suggests that the arrangement of oxygen atoms in PPO, which is similar to that of PEO, leads to

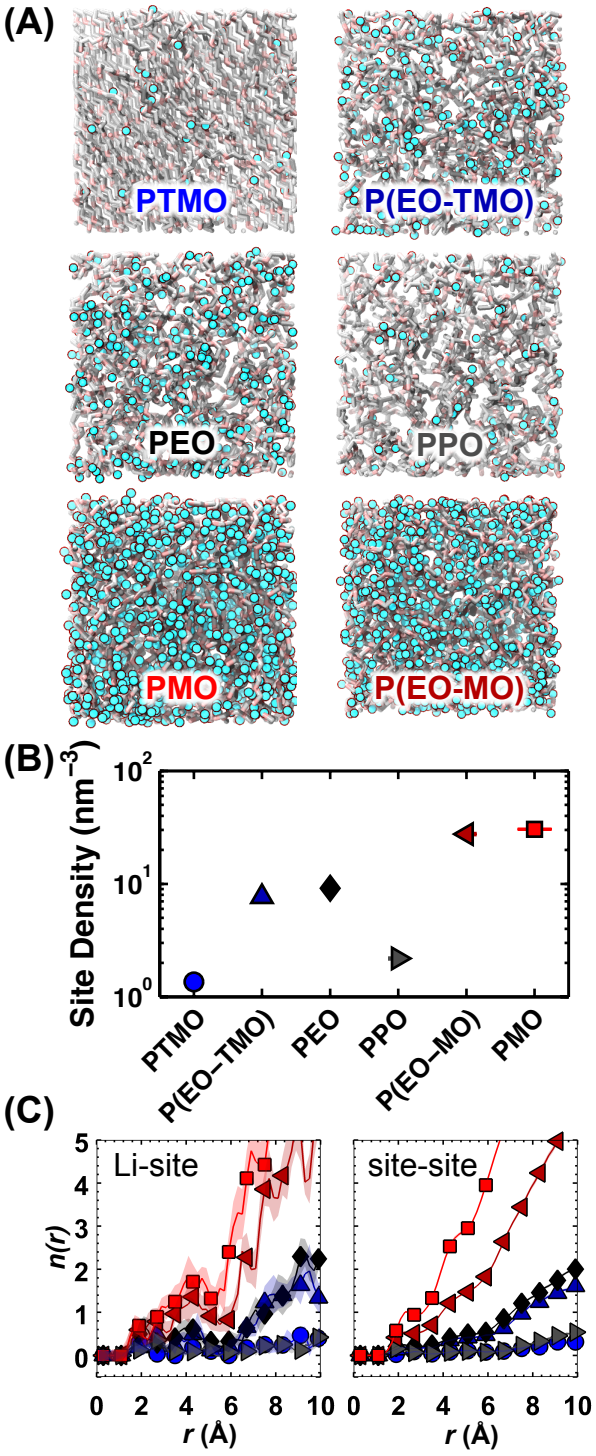

Figure 4.5: Analysis of solvation sites in the model. (A) A depiction of lithium cation sites (green circles) identified in a representative polymer configuration. (B) The number density of lithium cation sites in the model obtained from averaging twelve configurations in each polymer host. (C) Lithium-site and site-site radial NDFs, $n(r)$, across all polymers. The standard errors for the data in (C) and (D) are depicted with the colored, transparent regions.

more viable solvation sites.

Figure 4.5B makes a quantitative comparison of the site densities in the various polymers, which are obtained by averaging over twelve MD configurations for each polymer. An unexpected result is that the the site density of P(EO-TMO) is nearly identical to that of PEO, even though it is an alternating copolymer of PTMO and PEO repeat units; the same is true for P(EO-MO) with respect to PEO and PMO. These results indicate a non-trivial relationship between the density of solvation sites and the density of oxygen atoms in these polyethers.

Figure 4.5C compares the lithium-site and site-site NDFs. Both plots in Figure 4.5C exhibit similar trends with respect to the different polymers, although comparison between the lithium-site and site-site NDF for a given polymer reveals some minor differences. For example, the lithium-site NDF is relatively enriched compared to the site-site NDF at distances less than about 4 Å, whereas the lithium-site NDF is relatively depleted by comparison to the site-site NDF at distances between 4-6 Å. This suggests a "site recruitment" effect, in which the lithium cation attracts nearby coordinating atoms, resulting in an increase in the number of viable solvation sites in the vicinity of the oxygen atoms that coordinate the lithium cation. Due to a significant amount of self-averaging across the configurations, the errors associated with the site-site NDFs are much smaller than those in the lithium-site NDFs.

4.5.b Site Hopping Rates

We now illustrate the computations required in stage (2) of the model, in which the hopping rates among solvation sites are determined. As described in Section 4.3.c, these rates are obtained from atomistic MD simulations that account for polymer-specific properties, including the lithium-oxygen dissociation energy and the polymer reorganization energy.

Figure 4.6 provides the data required to calculate the dissociation energy contribution to the hopping rate (Eq. (4.5)). Figure 4.6A shows that $g_{\mathrm{Li,O}}(r)$ is strongly peaked for polymers with less oxygen content, which indicates that the relative cost of disrupting a single lithium-oxygen interaction in PTMO is greater than that for a more oxygen-rich polymer like PMO. However, Figure 4.6B reveals that this effect is small, as the intrinsic dissociation energy E^0_{dis} varies by less than 1 kcal/mol across the set of polyethers. Figure 4.6C provides the site-overlap function $z(r)$ for each polymer, which also impacts the dissociation energy contribution according to Eq. (4.5). Note that the trends in Figure 4.6C are nearly inverted compared to

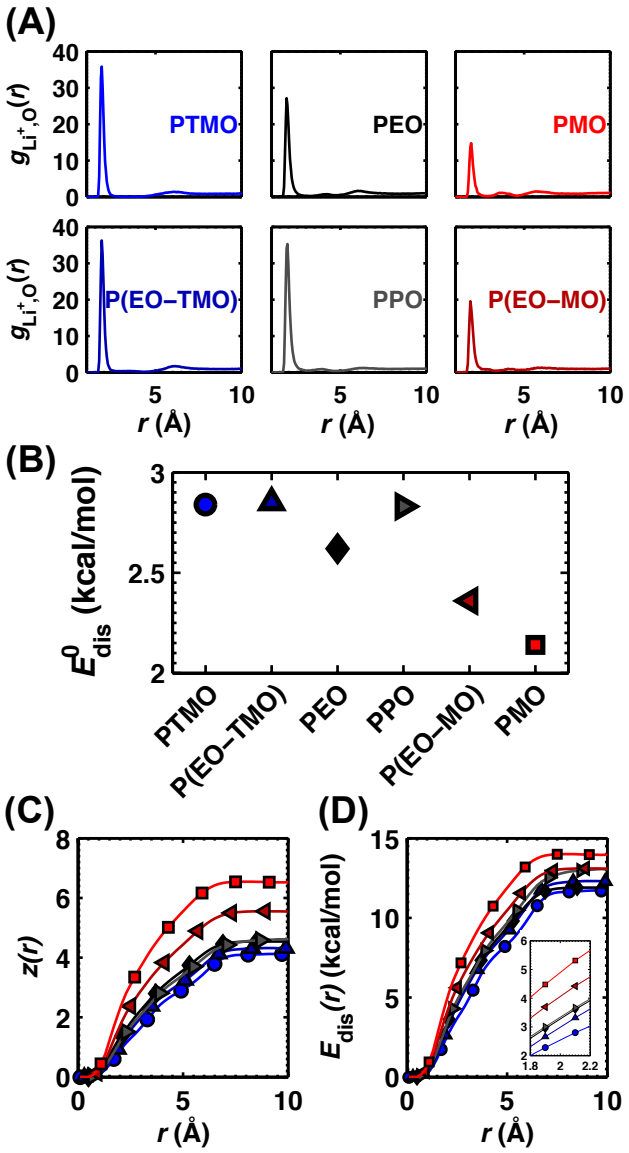

Figure 4.6: Analysis of the dissociation energy contribution to the model. (A) Lithium-O pair radial distribution functions in each polymer, (B) the intrinsic dissociation energy E^0_{dis} determined via Eq. (4.4), (C) the average number of oxygen atoms displaced during transition as a function of distance $z(r)$, and (D) the computed dissociation energy computed using (B) and (C). The inset shows the relative ordering of the curves around 2 Å

those observed in Figure 4.6B; although individual lithium-oxygen interactions are somewhat easier to break in oxygen-rich compared to oxygen-poor environments, a larger number of interactions must be broken in oxygen-rich environments to move between sites at a given distance. Using Eq. (4.5), the results of Figure 4.6B and 4.6C are combined to compute the final dissociation energy contribution to the hopping rate, which is given in Figure 4.6D. Despite the trend in Figure 4.6B, Figure 4.6D

indicates that the dissociation energy generally increases with oxygen content.

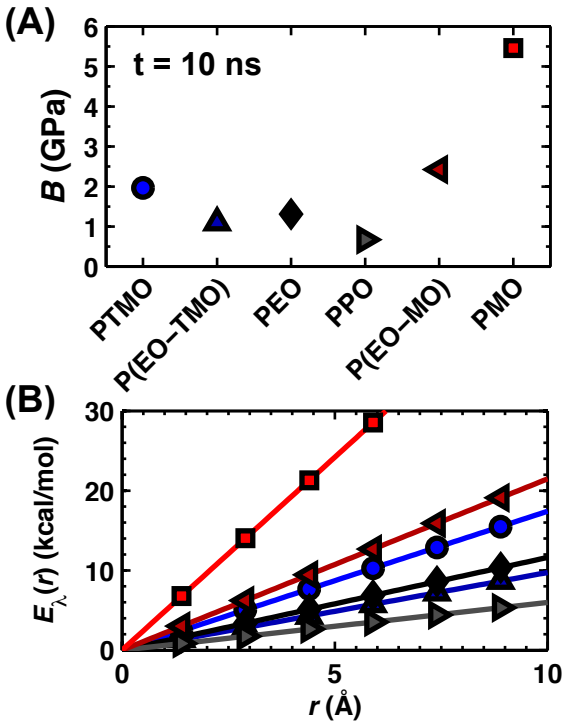

Figure 4.7: Analysis of the reorganization energy contribution to the model. (A) Comparison of bulk moduli used for the model, obtained after $t = 10$ ns of simulation. (B) The reorganization energy computed from Eq. (4.6) and the bulk moduli in (B).

Figure 4.7 presents the data needed to compute the reorganization energy contribution to the hopping rate using Eq. (4.6). Figure 4.7A reports the values of the bulk modulus for each polymer, which is well-converged after approximately 5 ns of simulation time. PMO and P(EO-MO) have the largest bulk moduli, which correlates with their high polymer density and oxygen content. PTMO has a larger bulk modulus than expected, which may be the result of its ordered structure, as noted in Section 4.4.a. Figure 4.7B shows the reorganization energy computed using Eq. (4.6). Both Figure 4.6D and Figure 4.7B illustrate energetic penalties that disfavor long-ranged hopping events.

Figure 4.8 displays the final intrinsic hopping rate constant $k_0(r)$ computed from Eq. (4.3) using the data from Figures 4.6 and 4.7 and the attempt frequencies taken from the lithium-ion VACF; a summary of the contributions is provided in Table 4.1. Due to a combination of large bulk moduli and rapidly increasing $z(r)$, P(EO-MO) and PMO have small $k_0(r)$ relative to the other polymers. Conversely, $k_0(r)$ for PPO is the largest among the polymers considered, due to its low bulk modulus and correspondingly small reorganization energy. Note that the rates in Figure 4.8 do not

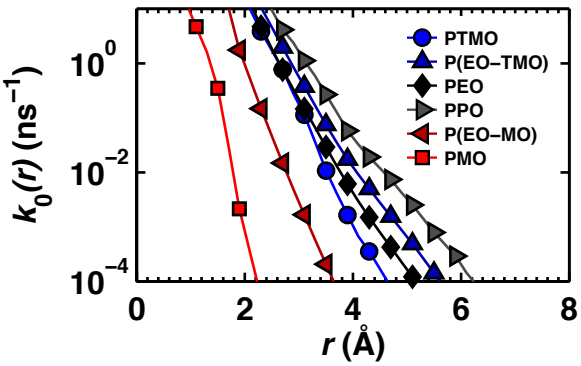

Figure 4.8: Intrinsic hopping rates between sites at a given distance for each polymer.

entirely determine the lithium-ion diffusivity since they do not contain information regarding the distribution of available lithium-ion solvation sites nor the site-refresh rate; to model lithium-ion diffusion, these distance-dependent rates are employed in KMC simulations that explicitly account for the fluctuating distribution of solvation sites.

Table 4.1: Summary of various CS-DBP model inputs for the polyethers.

Polymer	ρ_{site} (nm^{-3})^{a,b}	$E_{\text{dis}}^{(0)}$ ($\frac{\text{kcal}}{\text{mol}}$)^b	B (GPa)^b	τ (ps^{-1})	ν (ns^{-1})
PTMO	1.33(5)	2.84(4)	1.8(1)	29.1	2.9
P(EO-TMO)	6.60(9)	2.85(5)	1.10(1)	28.7	8.1
PPO	1.95(5)	2.8(2)	0.68(1)	26.5	1.2
PEO	8.12(3)	2.62(8)	1.29(1)	27.8	6.1
P(EO-MO)	23.8(4)	2.4(1)	2.25(5)	29.0	0.6
PMO	44.1(3)	2.1(1)	4.9(5)	26.7	0.3

[a] Density of solvation sites in polymer

[b] Statistical errors of the final digit are indicated in parentheses

4.5.c KMC Simulation Results

In stage (3) of the CS-DBP model, the results of Sections 4.5.a and 4.5.b are used in KMC simulations to obtain long-timescale lithium-ion diffusion properties in each polymer. To make predictions for a given polymer, it is necessary that the KMC simulations utilize polymer-specific solvation-site distributions. Figure 4.9 illustrates a comparison between the reference site-site RDFs obtained directly from MD and those generated via the IBI procedure for the CS-DBP model. Although IBI reproduces the site-site RDFs for all polymers well, we find that this inversion is less robust for the lithium-site RDFs. Due to these results, as well as the similarity between the lithium-site and site-site NDFs in Figure 4.6, all CS-DBP model results

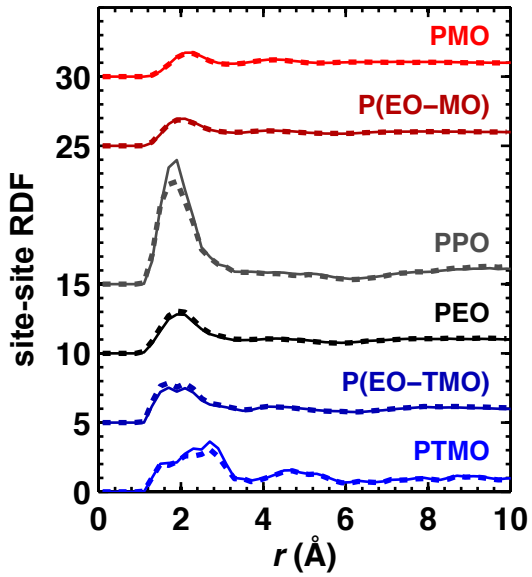

Figure 4.9: Site-site radial distribution functions (RDF) obtained from MD (solid lines) and from IBI (dashed lines). For clarity, the data for P(EO-TMO), PEO, PPO, P(EO-MO), and PMO are shifted vertically by 5, 10, 15, 25, and 30 units, respectively.

are obtained using the site-site RDFs.

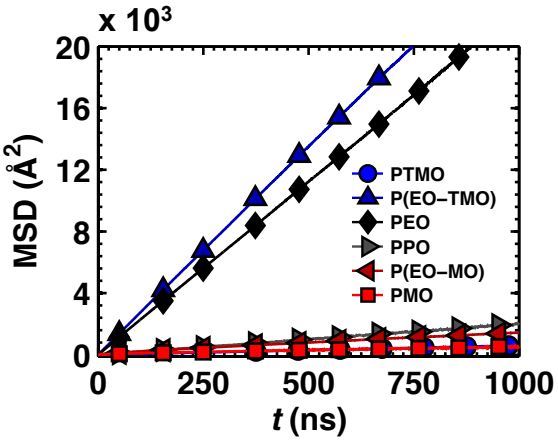

Figure 4.10: Mean square-displacement (MSD) of a lithium cation obtained from KMC trajectories using the CS-DBP model.

Figure 4.10 presents the final mean-square displacements associated with lithium-ion diffusion as predicted by the CS-DBP model for the polymers studied. As expected, lithium-ion diffusion is much faster in PEO than in many of the other polyethers such as PPO and PTMO, which are known to exhibit small experimental conductivities.[86] The CS-DBP model also predicts slow lithium-ion diffusion for P(EO-MO) and PMO, though the conduction properties of these polymers have yet to be experimentally studied. A surprising prediction of the model is that P(EO-

TMO) exhibits faster lithium-ion diffusion than even PEO. This is unexpected since P(EO-TMO) is an alternating copolymer of the repeat units in PEO and PTMO, and the latter homopolymer is characterized by very slow lithium-ion diffusion.

Importantly, the CS-DBP model enables a qualitative understanding of the results of Figure 4.10. For example, sparse site distributions limit lithium-ion diffusion in PPO and PTMO, and large reorganization energies limit diffusion in P(EO-MO) and PMO. Furthermore, we note that neither P(EO-TMO) nor PEO has the best site distribution (Figure 4.5) or the fastest hopping rates (Figure 4.8), yet the combination of average properties leads to faster lithium-ion diffusion by comparison to the other polyethers. The results also suggest that the site-refresh rate plays a role in lithium-ion diffusion, as the site-refresh rate for PEO exceeds that of all others except for P(EO-TMO).

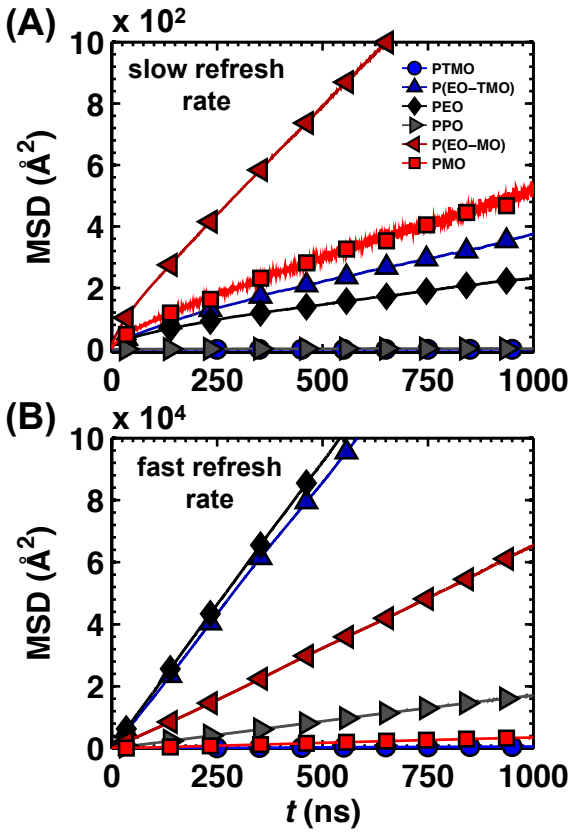

Figure 4.11: Mean square-displacement (MSD) of a lithium cation obtained from KMC trajectories using (A) $\nu = 0$ and (B) $\nu = 2000$ ns^{-1}. Note the change in scale of the y-axis in the different panels.

To illustrate the effect of the site-refresh rate on the lithium-ion diffusivity, Figure 4.11A and 4.11B show limiting cases obtained using infinitely slow ($\nu = 0$ ns^{-1}) and very fast ($\nu = 2000$ ns^{-1}) refresh rates for each polymer. In both cases, the mag-

nitude and ordering of the results are somewhat different than those in Figure 4.10. In Figure 4.11A, all lithium-ion diffusion is slowed, but P(EO-MO) and PMO actually exhibit the fastest lithium-ion diffusion. Here, lithium cations in polymers like PPO and PTMO are largely confined to hopping within a local cluster with few sites or forced to make long-range hops, which limits the diffusivity and indicates that the site distribution primarily controls lithium-ion diffusion in this regime. In Figure 4.11B, lithium-ion diffusion is faster than that shown in Figure 4.10, but the hopping rates among sites becomes increasingly important, as evidenced by the rate of lithium-ion diffusion in PPO. Thus, all three factors in the model–the site distributions, hopping rates, and refresh rates–are important in determining the overall rate of lithium-ion diffusion.

4.5.d Comparison to Molecular Dynamics

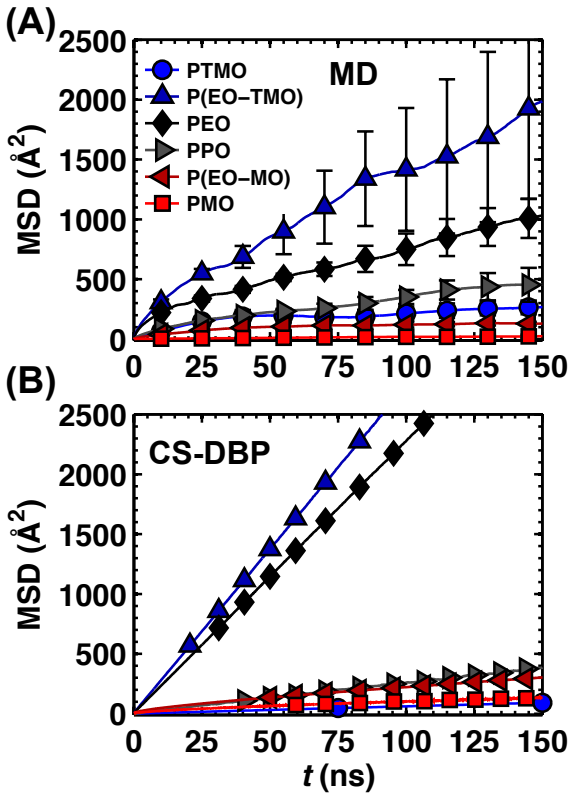

Figure 4.12: Mean square-displacement of lithium cation obtained from (A) MD simulation and (B) the CS-DBP model. Note that the data in (B) are the same as in Figure 4.10, but the limits of the axes are changed.

To validate the predictions of the CS-DBP model, we now compare the results of direct simulations of lithium-ion diffusivity from long MD trajectories of the

polymer systems (Figure 4.12A) with the results of the CS-DBP model (Figures 4.10 and 4.12B). The results in Figure 4.12B are identical to those from Figure 4.10, although they are presented for the shorter timescales associated with the atomistic MD simulations. We emphasize that whereas the results from the CS-DBP model required MD trajectories of only 10 ns or less, the corresponding model results in Figure 4.12A required multiple MD trajectories of 300 ns and still do not indicate fully diffusive behavior (see Figure S5 of the SI for an indication of the power-law scaling between MSD and time). Nonetheless, the relative ordering of the MSDs predicted by the CS-DBP model is very similar to that given by the MD simulations. It is particularly notable that the MD results predict that lithium-ion diffusion is faster in P(EO-TMO) compared to PEO and that the diffusivities of P(EO-TMO) and PEO are well-separated from those of the other polymers. It is also encouraging that the order of magnitude of the MSDs is comparable between Figure 4.12A and those of Figure 4.12B, despite the approximations of the CS-DBP model. Overall, the correlation between the MD and the CS-DBP model results suggests that the CS-DBP model provides a reasonable physical picture for lithium-ion transport in polymers and also incorporates sufficient chemical detail to distinguish transport characteristics in different polymers.

4.6 Additional Considerations

The good agreement between the results of the CS-DBP model (Figure 4.10) and that of brute-force MD simulations (Figure 4.12A) offers encouraging validation of the new model. Nonetheless, several refinements and future developments are of interest to extend the scope of model. Firstly, no explicit counter-ion is currently included in the model, such that ion-pairing and aggregation effects are ignored; anions might be incorporated into the model as additional, specialized sites in the network. Secondly, cation-cation interactions associated with finite lithium-ion concentrations are not included; while we expect lithium-ion diffusivities at dilute-salt concentrations to correlate with ionic conductivities at higher salt concentrations, such effects might be incorporated by self-consistently including multiple cations on the same site network or by extracting model inputs from MD simulations that have multiple cations. Thirdly, while polymer dynamics are included in the model via the reorganization energy $E_\lambda(r)$, the dissociation energy $E_{\text{dis}}(r)$, and the site-refresh rate ν, both co-diffusion of the cation with the entire polymer chain and local segmental diffusion with coordinating chains is neglected. Although co-diffusion with the entire polymer is expected to be negligible in applications that feature polymer chains in excess

of 10,000 g/mol,[49,87,88] local segmental motion can contribute to the lithium-ion diffusivity even in high-molecular weight polymers due to coupling to higher-order Rouse modes.[49] In the future, local segmental diffusion could potentially be included, as in other theoretical models.[54] but it would require extraction of timescales that are not accessible in our current parameterization protocol. The inclusion of diffusive dynamics due to co-diffusion with polymer chain segments on timescales accessible in our protocol is the subject of current investigation. Finally, we note that the model can immediately be applied to systems that exhibit similar features of ion transport, including random copolymers and polymers with cross-linked, comb,[40,41] or graft polymer architectures,[43,48] and may additionally be applicable to polymeric single-ion conductors[39,44] and mixtures of polymers and ionic liquids[55,56] with some modification.

4.7 Conclusions

In this study, we present and apply a chemically specific (CS) extension to the dynamic bond percolation (DBP) model for ion transport in polymer electrolytes. As in the original model, the CS-DBP model characterizes ion diffusion in polymers as hopping transitions on a fluctuating lattice of solvation sites. However, the CS-DBP model additionally incorporates the molecular details of the polymer systems, including solvation-site distributions, site-hopping rates, and site-refresh rates. Although local segmental diffusion with coordinating chains is not presently included in the CS-DBP model, we note that polymer dynamics are reflected through the polymer reorganization energy, the dissociation energy, and the site-refresh rate. Importantly, all of the inputs for the CS-DBP model are physically motivated and accessible through short-timescale (1-10 ns) MD simulations, thus enabling predictions of long-timescale ion transport properties at reduced computational cost.

To demonstrate the CS-DBP model, it is applied to characterize the relative rate of lithium-ion diffusion in six polyethers, which exhibit a range of conductivity. Good agreement between results of the model (Figure 4.10) and those of the MD simulations (Figure 4.12A), both in terms of relative ordering and magnitude, suggest that the essential features of ion transport in polymers are included in the model and provide confidence in the calculation procedures (Section 4.3).

A notable advantage of the model is that it provides mechanistic insight for ion diffusion in polymer electrolytes, since the model characterizes ion diffusion in terms of the physical properties of the polymer. For example, the CS-DBP model

reveals that the origin of the slow lithium-ion diffusion in P(EO-MO) and PMO is the reorganization energy associated with lithium-ion hopping. In contrast, the origin of the slow lithium-ion diffusion in PPO and PTMO is due to the low density of solvation sites. These results support conventional efforts to design flexible polymers with low glass-transition temperatures, which correlates with lower reorganization energies, but it also motivates the design of polymers with polymer architectures that feature percolating networks of solvation sites. Additionally, the model demonstrates that efficient lithium-ion diffusion should occur through short hopping events that exchange only one or two lithium-oxygen solvating contacts as opposed to more long-ranged hopping events,[48] since the latter are more energetically costly.

Finally, the CS-DBP model yields the prediction of a new candidate polymer electrolyte, P(EO-TMO), that exhibits faster lithium-ion diffusion than PEO; this unintuitive prediction is confirmed via long-timescale MD simulations. This prediction illustrates that the CS-DBP model is well-suited for screening future candidate polymer electrolytes with semi-quantitative accuracy at reduced computational cost.

References

(1) Tarascon, J.; Armand, M *Nature* **2001**, *414*, 359–367.

(2) Fenton, D; Parker, J; Wright, P *Polymer* **1973**, *14*, 589–589.

(3) Van Gool, W.; Division, N. A. T. O. S. A., *Fast ion transport in solids: Solid state batteries and devices. Proceedings of the NATO sponsored Advanced Study Institute on Fast Ion Transport in Solids, Solid State Batteries and Devices, Belgirate, Italy, 5-15 September 1972*; North Holland Pub. Co.: 1973.

(4) Gray, F., *Solid Polymer Electrolytes: Fundamentals and Technological Applications*; Wiley: 1991.

(5) Armand, M. *Solid State Ion.* **1983**, *9–10, Part 2*, 745 –754.

(6) Watanabe, M.; Rikukawa, M.; Sanui, K.; Ogata, N.; Kato, H.; Kobayashi, T.; Ohtaki, Z. *Macromolecules* **1984**, *17*, 2902–2908.

(7) Motogami, K.; Kono, M.; Mori, S.; Watanabe, M.; Ogata, N. *Electrochim. Acta* **1992**, *37*, 1725 –1727.

(8) Harris, C. S.; Shriver, D. F.; Ratner, M. A. *Macromolecules* **1986**, *19*, 987–989.

(9) Blonsky, P. M.; Shriver, D. F.; Austin, P; Allcock, H. R. *J. Am. Chem. Soc* **1984**, *106*, 6854–6855.

(10) Shintani, Y.; Tsutsumi, H. *J. Power Sources* **2010**, *195*, 2863 –2869.

(11) Tsutsumi, H.; Suzuki, A. *Solid State Ion.* **2014**, *262*, 761 –764.

(12) Shintani, Y.; Tsutsumi, H. *Electrochemistry* **2010**, *78*, 387–389.

(13) Zhang, Z.; Jin, J.; Bautista, F; Lyons, L.; Shariatzadeh, N; Sherlock, D; Amine, K; West, R *Solid State Ion.* **2004**, *170*, 233 –238.

(14) Nakamura, M.; Tominaga, Y. *Electrochim. Acta* **2011**, *57*, 36–39.

(15) Croce, F; Persi, L; Scrosati, B; Serraino-Fiory, F; Plichta, E; Hendrickson, M. *Electrochim. Acta* **2001**, *46*, 2457 –2461.

(16) Johansson, P.; Ratner, M. A.; Shriver, D. F. *J. Phys. Chem. B* **2001**, *105*, 9016–9021.

(17) Florjanczyk, Z; Krawiec, W; Wieczorek, W; Przyluski, J *Angewandte Makromolekulare Chemie* **1991**, *187*, 19–32.

(18) Bouridah, A.; Dalard, F.; Deroo, D.; Cheradame, H.; Nest, J. L. *Solid State Ion.* **1985**, *15*, 233 –240.

(19) Wilson, D. J.; Nicholas, C. V.; Mobbs, R. H.; Booth, C *British Polymer Journal* **1990**, *22*, 129–135.

(20) Andrieu, X; Fauvarque, J. F.; Goux, A; Hamaide, T; Mhamdi, R; Vicedo, T *Electrochim. Acta* **1995**, *40*, 2295–2299.

(21) Deng, Y. L.; Ding, J. F.; Y U, G; Mobbs, R. H.; Heatley, F; Price, C; Booth, C *Polymer* **1992**, *33*, 1959–1962.

(22) Quartarone, E.; Mustarelli, P.; Magistris, A. *Solid State Ion.* **1998**, *110*, 1 –14.

(23) Buriez, O; Han, Y.; Hou, J; Kerr, J.; Qiao, J; Sloop, S.; Tian, M.; Wang, S. *J. Power Sources* **2000**, *89*, 149–155.

(24) Watanabe, M.; Hirakimoto, T.; Mutoh, S.; Nishimoto, A. *Solid State Ion.* **2002**, *148*, 399 –404.

(25) Miwa, Y; Tsutsumi, H; Oishi, T *Electrochemistry* **2002**, *70*, 264–269.

(26) Ikeda, Y; Masui, H; Matoba, Y *J. Appl. Polym. Sci* **2005**, *95*, 178–184.

(27) Nishimoto, A.; Watanabe, M.; Ikeda, Y.; Kohjiya, S. *Electrochim. Acta* **1998**, *43*, 1177 –1184.

(28) Wolfenson, A.; Torresi, R.; Bonagamba, T.; DePaoli, M.; Panepucci, H *J. Phys. Chem. B* **1997**, *101*, 3469–3473.

(29) Barbosa, P. C.; Rodrigues, L. C.; Silva, M. M.; Smith, M. J.; Parola, A. J.; Pina, F.; Pinheiro, C. *Electrochim. Acta* **2010**, *55*, 1495–1502.

(30) Nithya, H.; Selvasekarapandian, S.; Kumar, D. A.; Sakunthala, A.; Hema, M.; Christopherselvin, P.; Kawamura, J.; Baskaran, R.; Sanjeeviraja, C. *Mater. Chem. Phys.* **2011**, *126*, 404–408.

(31) Tanaka, R; Sakurai, M; Sekiguchi, H; Mori, H; Murayama, T; Ooyama, T *Electrochim. Acta* **2001**, *46*, 1709–1715.

(32) Barteau, K. P.; Wolffs, M.; Lynd, N. A.; Fredrickson, G. H.; Kramer, E. J.; Hawker, C. J. *Macromolecules* **2013**, *46*, 8988–8994.

(33) Khurana, R.; Schaefer, J. L.; Archer, L. A.; Coates, G. W. *J. Am. Chem. Soc.* **2014**, *136*, 7395–7402.

(34) Müller-Plathe, F; Vangunsteren, W. *J. Chem. Phys.* **1995**, *103*, 4745–4756.

(35) Neyertz, S; Brown, D *J. Chem. Phys.* **1996**, *104*, 3797–3809.

(36) Duan, Y.; Halley, J.; Curtiss, L; Redfern, P *J. Chem. Phys.* **2005**, *122*.

(37) Siqueira, L. J. A.; Ribeiro, M. C. C. *J. Chem. Phys.* **2006**, *125*.

(38) Borodin, O; Smith, G. *Macromolecules* **2006**, *39*, 1620–1629.

(39) Borodin, O.; Smith, G. D.; Geiculescu, O.; Creager, S. E.; Hallac, B.; DesMarteau, D. *J. Phys. Chem. B* **2006**, *110*, 24266–24274.

(40) Borodin, O.; Smith, G. D. *Macromolecules* **2007**, *40*, 1252–1258.

(41) Karo, J.; Brandell, D. *Solid State Ion.* **2009**, *180*, 1272–1284.

(42) Wu, H.; Wick, C. D. *Macromolecules* **2010**, *43*, 3502–3510.

(43) Brandell, D.; Priimaegi, P.; Kasemaegi, H.; Aabloo, A. *Electrochim. Acta* **2011**, *57*, 228–236.

(44) Lin, K.-J.; Maranas, J. K. *Phys. Chem. Chem. Phys.* **2013**, *15*, 16143–16151.

(45) Hanson, B.; Pryamitsyn, V.; Ganesan, V. *ACS Macro Lett.* **2013**, *2*, 1001–1005.

(46) Lin, K.-J.; Maranas, J. K. *Phys. Rev. E* **2013**, *88*, 052602.

(47) Mogurampelly, S.; Ganesan, V. *Macromolecules* **2015**, *48*, 2773–2786.

(48) Webb, M. A.; Jung, Y.; Pesko, D. M.; Savoie, B. M.; Yamamoto, U.; Coates, G. W.; Balsara, N. P.; Wang, Z.-G.; Miller III, T. F. *ACS Cent. Sci.* **2015**, 198–205.

(49) Diddens, D.; Heuer, A.; Borodin, O. *Macromolecules* **2010**, *43*, 2028–2036.

(50) Druger, S.; Nitzan, A; Ratner, M. *J. Chem. Phys.* **1983**, *79*, 3133–3142.

(51) Druger, S.; Ratner, M.; A, N. *Phys. Rev. B* **1985**, *31*, 3939–3947.

(52) Druger, S. D.; Ratner, M. A.; Nitzan, A. *Solid State Ion.* **1986**, *18–19, Part 1*, 106 –111.

(53) Nitzan, A; MA, R. *J. Phys. Chem.* **1994**, *98*, 1765–1775.

(54) Maitra, A.; Heuer, A. *Phys. Rev. Lett.* **2007**, *98*.

(55) Diddens, D.; Heuer, A. *ACS Macro Lett.* **2013**, *2*, 322–326.

(56) Chattoraj, J.; Diddens, D.; Heuer, A. *J. Chem. Phys.* **2014**, *140*.

(57) Chattoraj, J.; Knappe, M.; Heuer, A. *J. Phys. Chem. B* **2015**, *Article ASAP*.

(58) Snyder, J.; Ratner, M.; Shriver, D. *Solid State Ion.* **2002**, *147*, 249 –257.

(59) Schulz, B.; Karatchentsev, A.; Schulz, M.; Dieterich, W. *J. Non-Cryst. Solids* **2006**, *352*, 5136 –5140.

(60) Neyertz, S.; Brown, D. *Macromolecules* **2010**, *43*, 9210–9214.

(61) Bolhuis, P. G.; Chandler, D.; Dellago, C.; Geissler, P. L. *Annu. Rev. Phys. Chem.* **2002**, *53*, 291–318.

(62) Chandler, D., *Introduction to Modern Statistical Mechanics*; Oxford University Press: 1987.

(63) Varotsos, P.; Ludwig, W.; Alexopoulos, K. *Phys. Rev. B* **1978**, *18*, 2683–2691.

(64) Varotsos, P.; Alexopoulos, K., *Thermodynamics of point defects and their relation with bulk properties*; Defects in solids; North-Holland: 1986.

(65) Ingram, M.; Imrie, C.; Stoeva, Z; Pas, S.; Funke, K; Chandler, H. *J. Phys. Chem. B* **2005**, *109*, 16567–16570.

(66) Ingram, M. D.; Imrie, C. T.; Ledru, J.; Hutchinson, J. M. *J. Phys. Chem. B* **2008**, *112*, 859–866.

(67) Ingram, M. D.; Imrie, C. T. *Solid State Ion.* **2011**, *196*, 9–17.

(68) Pratt, L.; Chandler, D *J. Chem. Phys.* **1977**, *67*, 3683–3704.

(69) Hummer, G; Garde, S; Garcia, A.; Pohorille, A; Pratt, L. *Proc. Natl. Acad. Sci. U.S.A.* **1996**, *93*, 8951–8955.

(70) Hummer, G.; Garde, S.; García, A. E.; Paulaitis, M. E.; Pratt, L. R. *J. Phys. Chem. B* **1998**, *102*, 10469–10482.

(71) Chandler, D *Nature* **2005**, *437*, 640–647.

(72) Young, W. M.; Elcock, E. W. *Proc. Phys. Soc.* **1966**, *89*, 735.

(73) Bortz, A.; Kalos, M.; Lebowitz, J. *J. Comp. Phys.* **1975**, *17*, 10 –18.

(74) Gillespie, D. T. *J. Comp. Phys.* **1976**, *22*, 403 –434.

(75) Voter, A. F. In *Radiation Effects in Solids*, Sickafus, K., Kotomin, E., Uberuaga, B., Eds.; NATO Science Series, Vol. 235; Springer Netherlands: 2007, pp 1–23.

(76) Vanommeslaeghe, K.; Hatcher, E.; Acharya, C.; Kundu, S.; Zhong, S.; Shim, J.; Darian, E.; Guvench, O.; Lopes, P.; Vorobyov, I.; Mackerell, A. D. *J. Comput. Chem.* **2010**, *31*, 671–690.

(77) Stubbs, J. M.; Potoff, J. J.; Siepmann, J. I. *J. Phys. Chem. B* **2004**, *108*, 17596–17605.

(78) Borodin, O.; Smith, G. D.; Douglas, R. *J. Phys. Chem. B* **2003**, *107*, 6824–6837.

(79) Plimpton, S. *J. Comp. Phys.* **1995**, *117*, 1 –19.

(80) Brown, W. M.; Wang, P; Plimpton, S. J.; Tharrington, A. N. *Comput. Phys. Commun.* **2011**, *182*, 898–911.

(81) Brown, W. M.; Kohlmeyer, A.; Plimpton, S. J.; Tharrington, A. N. *Comput. Phys. Commun.* **2012**, *183*, 449–459.

(82) Figueirido, F.; Del Buono, G. S.; Levy, R. M. *The Journal of chemical physics* **1995**, *103*, 6133.

(83) Flory, P., *Statistical mechanics of chain molecules*; Interscience Publishers: 1969.

(84) Tildesley, D.; Allen, M. *Clarendon, Oxford* **1987**.

(85) Reith, D.; Pütz, M.; Müller-Plathe, F. *J. Comput. Chem.* **2003**, *24*, 1624–1636.

(86) Watanabe, M; Nagaoka, K; Kanba, M; Shinohara, I *Polym. J.* **1982**, *14*, 877–886.

(87) Shi, J.; Vincent, C. A. *Solid State Ion.* **1993**, *60*, 11 –17.

(88) Hayamizu, K.; Akiba, E.; Bando, T.; Aihara, Y. *J. Chem. Phys.* **2002**, *117*, 5929–5939.

Chapter 5

HIGH-THROUGHPUT SCREENING OF POLYMER ELECTROLYTES

In Chapter 4, we introduced a chemically specific dynamic bond percolation (CS-DBP) model for estimating lithium-ion diffusivities in polymer electrolytes. The power of the CS-DBP model is three-fold. First, it utilizes an abstraction of ion transport, i.e., hopping on a dynamical lattice of sites, which makes it generically applicable to many classes of polymer electrolytes. Second, the parameters describing the transition rates, lattice fluctuations, and lattice arrangement are derived from polymer-specific properties such that the predictions reflect the underlying chemistry of the polymer. Third, obtaining the requisite parameters for the CS-DBP model requires only short (<10 ns) molecular dynamics (MD) trajectories, which enables semi-quantitative predictions at near-trivial computational cost compared to equivalent MD trajectories.

In this chapter, we discuss the potential application of the CS-DBP model to high-throughput screening of polymer electrolyte materials. We discuss the scope and scale of studies for which the CS-DBP model is immediately suitable. In addition, some key challenges for these efforts are discussed.

5.1 Introduction

Rechargeable lithium-ion batteries are widely viewed as potential contributors to energy storage problems.[1,2] Lithium-ion batteries have found a number of applications as modern portable devices and even electric vehicles; applications in load-leveling for large-scale energy generation may also be an eventual possibility.[3–5] However, recent years have seen a litany of notable lithium-ion battery failures, including those in electric vehicles like the Chevy Volt[6] and Tesla Model S,[7] the 787 Boeing Dreamliner,[8] and the Hoverboard toy.[9] These examples highlight safety and performance issues that must be addressed before secondary lithium-ion technology can be reliably and practically implemented for high energy content usage.[3,10,11]

A critical problem with even state-of-the-art lithium-ion batteries is that the electrolyte solvent is typically a flammable, liquid mixture of alkyl carbonates that additionally exhibits limited operating temperatures, electrode corrosion, and metal

dendrite growth during cycling. Any one or combination of these issues may lead to early catastrophic failure of the entire battery system.[12] Solid polymer electrolytes (SPEs) are non-flammable, non-volatile alternatives to liquid electrolytes that may exhibit superior mechanical and processing properties.[3,13–17] Interest in SPEs stems from the discovery in 1973 that alkali salts could dissolve and conduct in poly(ethylene oxide) (PEO).[18] Studies later suggested that ionic conductivity in polymer electrolytes was intrinsically coupled to the polymer dynamics,[14,19–22] motivating significant research effort on strategies to improve conductivity by (1) avoiding crystallization to and (2) lowering the glass-transition temperature T_g.[15,23–37] Nevertheless, conductivities in SPEs remain limited to about 10^{-4} S/cm at ambient temperatures, and remarkably, the best SPEs also remain based on PEO.[29]

The historical precedent set by the extensive characterization of PEO-based SPEs suggests that the next-generation polymer electrolytes will require new chemistries and/or new topologies to achieve substantial gains in conductivity. However, initial efforts to design SPEs with chemistries more varied than simple polyethers,[38–45] have not resulted in significant improvements in conductivity, in part due to a fundamental lack of understanding regarding the molecular underpinnings of ion transport in such systems. In previous chapters, we proposed a new framework for analyzing ion transport in polymer electrolytes that considers not only the polymer dynamics but also the solvation-site connectivity, which is a notion not articulated in earlier design efforts. These insights led to the development of a coarse-grained model (chemically specific dynamic bond percolation model, or CS-DBP) that should be widely applicable to predicting lithium-ion diffusivities in diverse sets of polymer electrolytes. Here, we provide a brief and speculative discussion on using the CS-DBP model for high-throughput screening of polymer electrolytes.

5.2 Scope

The CS-DBP model is particularly well-suited to study the influence of systematic variations on lithium-ion diffusivity for multiple reasons. First, its computational efficiency permits examination of a large number of small topological perturbations. Second, the semi-quantitative nature of the predictions are likely more robust in capturing trends due to systematic changes than in making one-off predictions. Third, the framework of CS-DBP, which transparently depends on a set of defined parameters, lends itself to straightforward identification of structure-function relationships. Chapters 3 and 4 provide examples of pseudo-systematic studies on a small scale, but CS-DBP is likely capable of much larger characterization efforts.

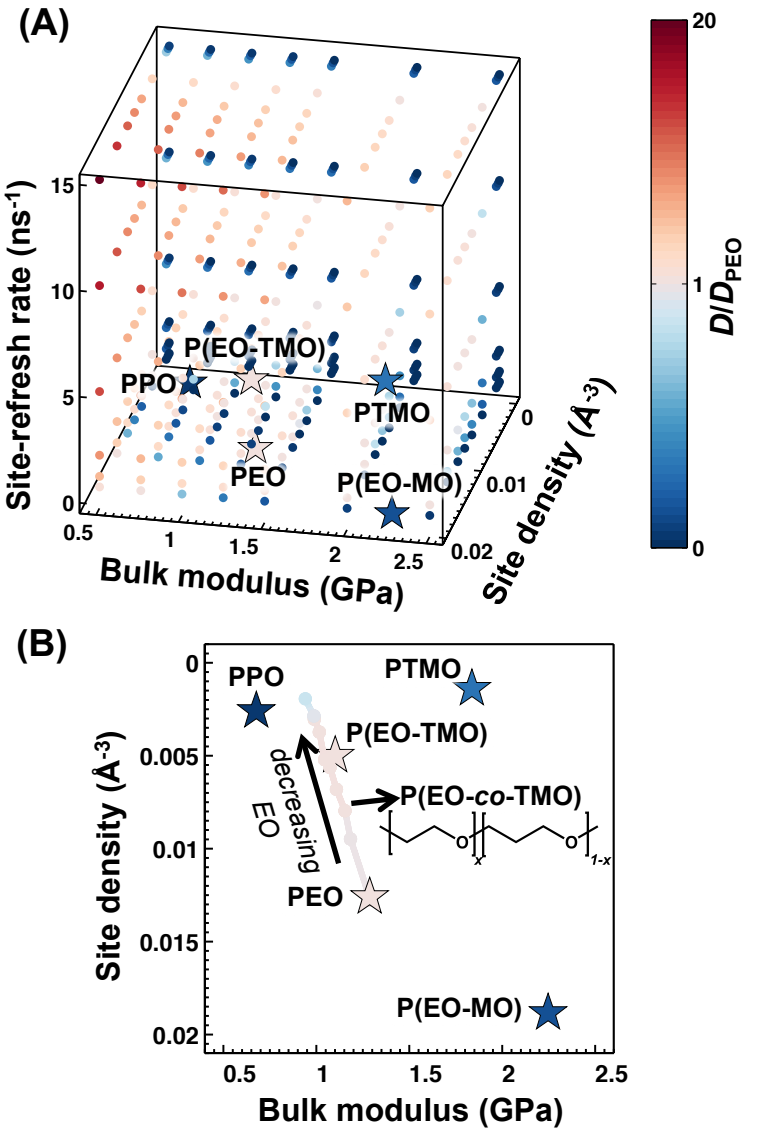

Figure 5.1: (A) Heat map of lithium-ion diffusivities obtained from the CS-DBP model in site-refresh rate/site density/bulk modulus ($\nu\rho B$) space. The positioning of each point in the diagram indicates the input properties for the CS-DBP model, and the color intensity indicates the predicted diffusivity relative to that in PEO. The pentagrams indicate results obtained using parameters that were determined from short MD simulations of the labeled polymers. The remaining spheres indicate results obtained using simple parameter combinations and do not represent the diffusivities of any particular polymer. (B) Heat map of lithium-ion diffusivities in select polyethers projected onto the ρB-plane. Note that y-axis is in a reversed orientation. The diffusivity for each point is computed as an average over 160 trajectories, each 10 μs in length.

Figure 5.1A presents a heat map of lithium-ion diffusivities in a simplified, three-dimensional parameter space of site-refresh rate, site density, and bulk modulus, henceforth referred to as $\nu\rho B$-space; as explained in Chapter 4, these parameters

reflect much of the essential physics of the ion transport process. The figure shows data for the polyethers studied in Chapter 4 (pentagrams) in addition to data obtained from 378 unique parameter combinations (spheres) that all assume the same generic site-site radial distribution function. Consequently, the different parameter combinations cannot be linked back to physical polymer chemistries. Nonetheless, the figure illustrates an idealized application of the CS-DBP model to easily characterize large numbers of polymers at very little computational cost.

By construction, the data for the aphysical* polymers span a significant portion of $\nu\rho B$-space and exhibit a range of diffusivities. In Figure 5.1A, the data for the polyethers, which have some variation in topology but feature the same ion-solvating groups (oxygen atoms), appear to be confined to a small sub-volume of $\nu\rho B$-space. In particular, site-refresh rates for the polyethers are within a narrow range. One possibility is that physical polymers cannot attain very high site-refresh rates; perhaps a more interesting possibility is that this *particular* class of polymers cannot attain very high site-refresh rates. The latter situation implies a pertinent application of the CS-DBP model–to perform systematic class-based screening. Although the polymer electrolytes studied in this thesis all feature oxygen atoms as the primary ion-solvating group, nothing in the CS-DBP coarse-graining approach precludes analysis of other solvating groups. Thus, CS-DBP could be used to examine polymer electrolytes based on polythioethers, polyamines, polyphosphazenes, or polyboranes, among other possibilities. If such studies were confined to a small set of topological variants but included broad chemical diversity, the results could be used as a low-resolution map to identify the promising regions of chemical design space for future synthetic efforts. It will be generally interesting to understand how changing polymer chemistry enables access to different regions of $\nu\rho B$-space.

Beyond a broad characterization of chemical design space, CS-DBP also provides a framework to interrogate systematic changes in polymer topology. To illustrate this idea, Figure 5.1B shows a projection of Figure 5.1A onto the site-density/bulk modulus plane with the results of the aphysical polymers removed and data for random copolymers of ethylene oxide and trimethylene oxide, P(EO-*co*-TMO), added. The dataset, which is shown as a contour with points, includes random copolymers with average ethylene oxide comonomer ratios ranging from $x = 0.0$ to $x = 0.9$ in increments of 0.1. For each x studied, eight independent MD trajectories of 10 ns are run to obtain parameters for the CS-DBP model with a protocol similar

*without physical representation

to that described in Chapter 4. The longtime lithium-ion diffusivities are then obtained from 160 kinetic Monte Carlo trajectories of 10 μs based on the CS-DBP model. Figure 5.1B shows how tuning x in this case, which corresponds to fractional perturbations to polymer topology, nearly reflects moving along a diagonal in $\nu\rho B$-space and a corresponding "hyper" contour in diffusivity-$\nu\rho B$-space. In particular, decreasing x leads to tandem decreases in site density and bulk modulus, which is an effect that we have qualitatively identified and expected in previous chapters. We suspect that a similar characterization for P(EO-*co*-MO), i.e., random copolymers of ethylene oxide and methylene oxide, would trace a contour that roughly links the pentagrams labeled PEO and P(EO-MO) and extends into regions not shown. Studies of this kind would enable clear identification of structure-function relationships, demonstrating how structural changes manifest in material properties that in turn affect the diffusivity. Moreover, these finer-resolution systematics could be used for design optimization.

5.3 Challenges

In a screening application, the CS-DBP model would make use of properties derived from MD simulations, and for the foreseeable future, those MD simulations will use parameterized force fields. Therefore, a major obstacle to high-throughput, computational screening of polymer electrolytes, or even small-scale systematic studies, is the availability of reliable force-field parameters to study polymers with diverse chemistries. The extent that CS-DBP can make predictions that usefully guide design efforts assumes that the MD simulations reasonably reflect the properties of real chemical systems. Unfortunately, parameters to study even simple polymers of interest, like polyphosphazenes, do not exist, and moreover, there is little consistency in the way that existing parameters are obtained, which naturally limits the efficacy of comparative studies. We are actively working to develop consistent force-field parameterization strategies that enable MD simulations of polymer electrolytes for any desired chemistry and topology, but this remains an existing limitation.

Another question related to the efficacy of CS-DBP model predictions is its applicability to higher concentration regimes and its capability to describe ion-ion correlations. In many cases, understanding lithium-ion transport in the dilute regime may be sufficient to provide guidance of design efforts and general design principles. Nevertheless, the nature of ion diffusion at higher concentrations is of interest, and atomistic MD is extremely limited in its capacity to study such regimes. Therefore, it would be valuable if the CS-DBP framework could be extended to provide insights

regarding ion-transport phenomena in high-concentration regimes.

5.4 Conclusions

To conclude, the CS-DBP model seems well-suited to (1) assay the general effect of polymer chemistry on ion transport through systematic variations in solvating groups and (2) provide systematic characterization of topological effects within a given chemical space. The viability of CS-DBP for these applications derives from its general description of ion transport in disordered systems and its computationally efficient coarse-graining approach to obtain system-specific properties. A significant obstacle for computational screening of polymer electrolytes in general is the availability of methodologically consistent force fields. For the existing CS-DBP model, it is most important that the force fields provide a reasonable description of neat-polymer properties, but accurate descriptions of ion-ion interactions will be of general interest to understanding ion transport at high salt concentrations, which was not anywhere a focus in this thesis. A related point is that predictions of the CS-DBP model are limited to the dilute-ion limit, neglecting ion-ion correlations and property changes induced by salt loading. For high-throughput screening applications, it may be that predictions in the dilute-ion limit are sufficient to direct synthetic efforts with efficacy. However, the possibility that some candidate materials would perform exceptionally well in certain concentration regimes and worse in others makes screening at finite concentrations a desirable capability.

References

(1) Divya, K.; Østergaard, J. *Electric Power Systems Research* **2009**, *79*, 511 –520.

(2) Marom, R.; Amalraj, S. F.; Leifer, N.; Jacob, D.; Aurbach, D. *J. Mater. Chem.* **2011**, *21*, 9938–9954.

(3) Tarascon, J.; Armand, M *Nature* **2001**, *414*, 359–367.

(4) Arico, A. S.; Bruce, P.; Scrosati, B.; Tarascon, J.-M.; van Schalkwijk, W. *Nature Materials* **2005**, *4*, 366–377.

(5) Bruce, P. G.; Scrosati, B.; Tarascon, J.-M. *Angewandte Chemie* **2008**, *47*, 2930–46.

(6) Muller, J. GM Moves Quickly To Put Out Chevy Volt Firestorm., ed. by forbes.com, [Online; posted 28-November-2011], 2011.

(7) Woollaston, V. New blow for Tesla: Fire in the 'world's safest electric car' began in vehicle's battery., ed. by dailymail.co.uk, [Online; posted 03-October-2013], 2013.

(8) Jamieson, A. Boeing 787 Dreamliner Fire: Investigators Urge Battery Safety Review., ed. by nbcnews.com, [Online; posted 21-August-2015], 2015.

(9) Moynihan, T. Why Hoverboards Keep Exploding., ed. by wired.com, [Online; posted 12-December-2015], 2015.

(10) Goodenough, J. B.; Kim, Y. *Chemistry of Materials* **2010**, *22*, 587–603.

(11) Goodenough, J. B. *Accounts of Chemical Research* **2013**, *46*, 1053–1061.

(12) Agrawal, R. C.; Pandey, G. P. *Journal of Physics D: Applied Physics* **2008**, *41*, 223001.

(13) Van Gool, W.; Division, N. A. T. O. S. A., *Fast ion transport in solids: Solid state batteries and devices. Proceedings of the NATO sponsored Advanced Study Institute on Fast Ion Transport in Solids, Solid State Batteries and Devices, Belgirate, Italy, 5-15 September 1972*; North Holland Pub. Co.: 1973.

(14) Armand, M. *Solid State Ion.* **1983**, *9–10, Part 2*, 745 –754.

(15) Alloin, F; Sanchez, J. Y.; Armand, M *J. Electrochem. Soc* **1994**, *141*, 1915–1920.

(16) Meyer, W. H. *Adv. Mater.* **1998**, *10*, 439–448.

(17) Jr., D. T. H.; Balsara, N. P. *Annual Review of Materials Research* **2013**, *43*, 503–525.

(18) Fenton, D; Parker, J; Wright, P *Polymer* **1973**, *14*, 589–589.

(19) Papke, B. L.; Ratner, M. A.; Shriver, D. F. *Journal of Physics and Chemistry of Solids* **1981**, *42*, 493–500.

(20) Berthier, C.; Gorecki, W.; Minier, M.; Armand, M. B.; Chabagno, J. M.; Rigaud, P. *Solid State Ion.* **1983**, *11*, 91–95.

(21) Druger, S.; Nitzan, A; Ratner, M. *J. Chem. Phys.* **1983**, *79*, 3133–3142.

(22) Druger, S.; Ratner, M.; A, N. *Phys. Rev. B* **1985**, *31*, 3939–3947.

(23) Croce, F.; Appetecchi, G. B.; Persi, L.; Scrosati, B. *Nature* **1998**, *394*, 456–458.

(24) Croce, F; Persi, L; Scrosati, B; Serraino-Fiory, F; Plichta, E; Hendrickson, M. *Electrochim. Acta* **2001**, *46*, 2457 –2461.

(25) Johansson, P.; Ratner, M. A.; Shriver, D. F. *J. Phys. Chem. B* **2001**, *105*, 9016–9021.

(26) Nishimoto, A.; Watanabe, M.; Ikeda, Y.; Kohjiya, S. *Electrochim. Acta* **1998**, *43*, 1177 –1184.

(27) Watanabe, M.; Hirakimoto, T.; Mutoh, S.; Nishimoto, A. *Solid State Ion.* **2002**, *148*, 399 –404.

(28) Matoba, Y.; Ikeda, Y.; Kohjiya, S. *Solid State Ion.* **2002**, *147*, 403 –409.

(29) Buriez, O; Han, Y.; Hou, J; Kerr, J.; Qiao, J; Sloop, S.; Tian, M.; Wang, S. *J. Power Sources* **2000**, *89*, 149–155.

(30) Khurana, R.; Schaefer, J. L.; Archer, L. A.; Coates, G. W. *J. Am. Chem. Soc.* **2014**, *136*, 7395–7402.

(31) Andrieu, X; Fauvarque, J. F.; Goux, A; Hamaide, T; Mhamdi, R; Vicedo, T *Electrochim. Acta* **1995**, *40*, 2295–2299.

(32) Deng, Y. L.; Ding, J. F.; Y U, G; Mobbs, R. H.; Heatley, F; Price, C; Booth, C *Polymer* **1992**, *33*, 1959–1962.

(33) Florjanczyk, Z; Krawiec, W; Wieczorek, W; Przyluski, J *Angewandte Makromolekulare Chemie* **1991**, *187*, 19–32.

(34) Ikeda, Y; Masui, H; Matoba, Y *J. Appl. Polym. Sci* **2005**, *95*, 178–184.

(35) Schroers, M; Kokil, A; Weder, C *J. Appl. Polym. Sci* **2004**, *93*, 2883–2888.

(36) Wolfenson, A.; Torresi, R.; Bonagamba, T.; DePaoli, M.; Panepucci, H *J. Phys. Chem. B* **1997**, *101*, 3469–3473.

(37) Barteau, K. P.; Wolffs, M.; Lynd, N. A.; Fredrickson, G. H.; Kramer, E. J.; Hawker, C. J. *Macromolecules* **2013**, *46*, 8988–8994.

(38) Watanabe, M.; Rikukawa, M.; Sanui, K.; Ogata, N.; Kato, H.; Kobayashi, T.; Ohtaki, Z. *Macromolecules* **1984**, *17*, 2902–2908.

(39) Blonsky, P. M.; Shriver, D. F.; Austin, P; Allcock, H. R. *Solid State Ion.* **1986**, *18-9*, 258–264.

(40) Harris, C. S.; Shriver, D. F.; Ratner, M. A. *Macromolecules* **1986**, *19*, 987–989.

(41) Lee, Y. C.; Ratner, M. A.; Shriver, D. F. *Solid State Ion.* **2001**, *138*, 273–276.

(42) Zhang, Z.; Jin, J.; Bautista, F; Lyons, L.; Shariatzadeh, N; Sherlock, D; Amine, K; West, R *Solid State Ion.* **2004**, *170*, 233 –238.

(43) Tominaga, Y; Shimomura, T; Nakamura, M *Polymer* **2010**, *51*, 4295–4298.

(44) Nakamura, M.; Tominaga, Y. *Electrochim. Acta* **2011**, *57*, 36–39.

(45) Webb, M. A.; Jung, Y.; Pesko, D. M.; Savoie, B. M.; Yamamoto, U.; Coates, G. W.; Balsara, N. P.; Wang, Z.-G.; Miller III, T. F. *ACS Cent. Sci.* **2015**, 198–205.

Part II

Position-specific and Clumped Isotope Effects

Chapter 6

COMPARISON OF THE UREY AND PATH-INTEGRAL APPROACHES FOR ISOTOPOLOGUES OF CARBON DIOXIDE, NITROUS OXIDE, METHANE, AND PROPANE

The theoretical foundation of the Urey model for computing equilibrium isotope effects is the rigid-rotor, harmonic oscillator approximation. Although this approach is expected to yield reasonably accurate estimates for the free energies of isotopologues in many molecular systems, the essential question asked in this chapter is "*is it accurate enough?*" The increasing accuracy and precision of analytical instrumentation to measure isotopic enrichment demands an answer, and if the answer is no, then different approaches are required to provide calculations of accuracy commensurate to that of experimental observables.

In this chapter, we combine path-integral Monte Carlo methods with high-quality potential energy surfaces to compute equilibrium isotope effects in a variety of systems relevant to 'clumped' isotope analysis and isotope geochemistry, including CO_2, N_2O, methane, and propane. Through a systematic study of heavy-atom isotope-exchange reactions, we quantify and analyze errors that arise in the widely used Urey model for predicting equilibrium constants of isotope-exchange reactions using reduced partition function ratios. These results illustrate that the Urey model relies on a nontrivial cancellation of errors that can shift the apparent equilibrium temperature by as much as 35 K for a given distribution of isotopologues. The calculations reported here provide the same level of precision as the best existing analytical instrumentation, resolving free-energy differences to within 6×10^{-6} kcal/mol. These findings demonstrate path-integral methods to be a rigorous and viable alternative to more approximate methods for heavy-atom geochemical applications.

Data and content in this chapter have been published as M.A. Webb and T.F. Miller III. "Position-Specific and Clumped Stable Isotope Studies: Comparison of the Urey and Path-Integral Approaches for Carbon Dioxide, Nitrous Oxide, Methane, and Propane." *J. Phys. Chem. A*, **118**, 467-474 (2014).

6.1 Introduction

Stable isotope analyses are essential for the understanding of many atmospheric, environmental, biological, and geochemical processes.[1–9] Recently developed methods for experimental analysis of isotopic enrichment can detect the enhanced thermodynamic stability of a specific placement or 'clumping' of rare isotopes.[10–15] Position-specific or clumped isotope enrichment results from homogeneous isotopic fractionation, which is quantified by

$$\Delta_i = 1000\left[\frac{(x_i/x_0)_{\mathrm{eq}}}{(x_i/x_0)_{\mathrm{r}}} - 1\right], \tag{6.1}$$

the degree to which a given isotopologue is enriched in the equilibrium ensemble due to its relative thermodynamic stability.[16] Here, x_i/x_0 is the abundance of a particular isotopologue, i, relative to that with no rare isotope substitutions; $(\cdots)_{\mathrm{eq}}$ indicates quantities obtained from the equilibrium thermal distribution; and $(\cdots)_{\mathrm{r}}$ indicates quantities obtained from the stochastic distribution, in which the abundances of isotopologues are strictly determined by the abundances of their composite isotopes.

Though the effects of homogeneous isotopic fractionation may be subtle, modern instruments can determine Δ_i to precisions of $0.01 - 0.02‰$.[12,17–19] Relating the enrichment of isotopologues to their thermal populations (Eq. (6.1)) enables the correlation of measurements of isotopic enrichment with temperatures in the geological record, thus facilitating applications that include the reconstruction of ancient marine ocean temperatures, the determination of body temperatures of extinct vertebrates, and the assessment of hydrocarbon deposits and organic matter.[10,20–24] Clumped and position-specific isotope analyses are also used to characterize the production and consumption mechanisms of greenhouse gases.[5,11,13,14,25,26]

Theoretical methods are essential for both understanding and predicting stable isotope fractionation.[16,23,27–32] In particular, theoretical predictions regarding isotopic clumping can be used to establish an absolute reference frame for standardizing isotope ratio measurements, which assist in inter-laboratory reproducibility.[17] For decades, the primary theoretical framework for characterizing equilibrium isotope effects has been the Urey model.[16,23,32–34] In this approach, however, effects associated with vibrational anharmonicity and rovibrational coupling are ignored, which may become problematic as analytical instruments resolve increasingly smaller temperature differences. Although anharmonic and other corrections to the Urey model have been developed,[35,36] the correction terms are generally complicated and have not been widely employed.

The Feynman path-integral (PI) formulation of quantum statistical mechanics[37] provides a useful framework for calculating equilibrium isotope effects. By exploiting the mathematical isomorphism between the quantum Boltzmann statistics of a given system and the classical Boltzmann statistics of its ring-polymer representation, PI methods have been applied to study equilibrium isotope effects, particularly for

Here, PI Monte Carlo (PIMC) is used to predict the temperature-dependence of equilibrium constants in isotope-exchange reactions featuring heavy-atom isotope exchange between isotopologues of CO_2, N_2O, methane, and propane. The reported calculations resolve the enrichment of isotopologues to the same level as experimental resolution, while employing accurate, isotopically-independent potential energy surfaces for CO_2, N_2O, and methane. These simulations are used to identify and examine breakdowns in the assumptions of the Urey model. The impact of these potential errors on the determination of apparent equilibrium temperatures is further explored.

6.2 Methodology

We aim to investigate the relative enrichment of isotopologues that are of primary interest in clumped and position-specific isotope analysis.

For clumped isotope analysis, we assess the balance of thermodynamic equilibrium in isotopic clumping reactions that principally influence the abundance of clumped isotopologues, such as

$$\mathrm{XY} + \mathrm{X'Y'} \overset{K}{\rightleftharpoons} \mathrm{XY'} + \mathrm{X'Y}, \tag{6.2}$$

where $K = \frac{Q_{\mathrm{XY'}}}{Q_{\mathrm{XY}}}\frac{Q_{\mathrm{X'Y}}}{Q_{\mathrm{X'Y'}}}$. Here, X′ and Y′ are rare isotopes of X and Y, respectively, and X′Y′ is the isotopically clumped species. The equilibrium constant for Eq. (6.2) can be connected to the experimentally measurable enrichment of X′Y′ as given by Eq. (6.1), $\Delta_{\mathrm{X'Y'}}$, via the relationship[16]

$$\Delta_{\mathrm{X'Y'}} = -1000 \ln(K/K_{\mathrm{r}}), \tag{6.3}$$

where K_{r} is the equilibrium constant in Eq. (6.2) for the stochastic distribution; this relation has a leading-order error of $O(\Delta_{\mathrm{X'Y}} + \Delta_{\mathrm{XY'}})$, which is generally small when there are no structural isotopomers for singly-substituted species (i.e., isomers with the same number of each isotope), as is the case for the specific reactions considered here.[16,32]

For position-specific isotope analysis, we assess the balance of thermal equilibrium in isotopomerization reactions that influence the relative isotopic enrichment of

specific positions in a molecule, such as

$$(\mathrm{X}_{m-1}\mathrm{X}'\mathrm{Y}_n)_i \overset{K_{ij}}{\rightleftharpoons} (\mathrm{X}_{m-1}\mathrm{X}'\mathrm{Y}_n)_j, \tag{6.4}$$

where $K_{ij} = \frac{Q_{(\mathrm{X}_{m-1}\mathrm{X}'\mathrm{Y}_n)_j}}{Q_{(\mathrm{X}_{m-1}\mathrm{X}'\mathrm{Y}_n)_i}}$. Here, $(\mathrm{X}_{m-1}\mathrm{X}'\mathrm{Y}_n)_i$ and $(\mathrm{X}_{m-1}\mathrm{X}'\mathrm{Y}_n)_i$ indicate isotopomers of $\mathrm{X}_m\mathrm{Y}_n$ with a single X' substitution. The relative enrichment of $(\mathrm{X}_{m-1}\mathrm{X}'\mathrm{Y}_n)_i$ for a set of t possible isotopomers is given by the expression[32]

$$\Delta_{(\mathrm{X}_{m-1}\mathrm{X}'\mathrm{Y}_n)_i} = 1000\left[\frac{mS_i}{1+\sum_{j\neq i}^{t} K_{ij}} - 1\right], \tag{6.5}$$

where $S_i = \sigma_i/\sigma_0$ is the ratio of the symmetry number for the isotopologue $(\mathrm{X}_{m-1}\mathrm{X}'\mathrm{Y}_n)_i$ and for that with no rare isotopes; the symmetry number is defined as the number of configurations that are indistinguishable by rotation.[38] This relation has a leading-order error that is proportional to the relative abundances of minority isotopes,[32] which are negligible for the specific reactions considered here.

Eqs. (6.3) and (6.5) have a clear connection to the temperature of the thermal ensemble through the various equilibrium constants. Differences between PI and Urey-model calculations of the equilibrium constant can thus be used to identify errors in the determination of apparent equilibrium temperatures using the Urey model.

6.2.a Urey Model

The Urey model uses the rigid-rotor and harmonic-oscillator approximations to compute partition function ratios (PFRs) that determine the relative abundances of isotopologues. By treating the rotational motions classically, the Teller-Redlich product rule[38,39] is applied to avoid explicitly calculating the molecular moments of inertia, such that the total PFR between two isotopologues is

$$\frac{Q'}{Q} = \frac{\sigma}{\sigma'} e^{-\beta(E_0'-E_0)} \prod_{i=1}^{N}\left(\frac{m_i'}{m_i}\right)^{3/2} \prod_{j=1}^{\alpha} \frac{\omega_j'}{\omega_j} \frac{1-\exp[-\beta\hbar\omega_j]}{1-\exp[-\beta\hbar\omega_j']}, \tag{6.6}$$

where σ and σ' again indicate the rotational symmetry numbers, $\beta = 1/(k_\mathrm{B}T)$ is the inverse temperature, E_0 is the zero-point energy, m_i is the mass of the ith atom in a molecule of N atoms, ω_j is the harmonic frequency of the jth normal mode, and α is the total number of normal vibrational modes ($\alpha = 3N-5$ for linear molecules and $3N-6$ for nonlinear molecules).

The utility of Eq. (6.6) is that it reduces the problem of calculating PFRs to that of determining the relative harmonic vibrational frequencies for different isotopologues. The zero-point energy is typically calculated from harmonic vibrational

contributions, such that $E_0 = \frac{1}{2}\sum_{j=1}^{\alpha}\hbar\omega_j$, although anharmonic and other contributions can also be approximately included.[36,40] In the following, calculations that employ the Urey model with a harmonic treatment of the zero-point energy are denoted Urey-HO; Urey-model calculations that include anharmonic corrections to the zero-point energy are denoted Urey-AHO.

6.2.b Path Integral Statistics

The quantum mechanical canonical partition function is given by the trace of the equilibrium density operator, $Q = \mathrm{Tr}\,(e^{-\beta\hat{H}})$.[37] The primitive, discretized PI representation of the partition function for a system of N distinguishable particles takes the form of a classical configuration integral,

$$Q(N,\beta) = \lim_{P\to\infty}\frac{1}{\sigma}\prod_{i=1}^{N}\left(\frac{m_i P}{2\pi\beta\hbar^2}\right)^{3P/2}\int\prod_{j=1}^{N}\prod_{k=1}^{P}d\boldsymbol{r}_j^{(k)}e^{-\beta_P U_P(\{\boldsymbol{r}_j^{(k)}\})}. \tag{6.7}$$

Here, P indicates the number of ring-polymer beads, $\boldsymbol{r}_j^{(k)}$ indicates the position of the jth atom in the kth ring-polymer bead, and $\beta_P = \beta/P$. The effective ring-polymer potential is

$$U_P(\{\boldsymbol{r}_j^{(k)}\}) = \sum_{j=1}^{N}\sum_{k=1}^{P}\left[\frac{1}{2}m_j\omega_P^2(\boldsymbol{r}_j^{(k)}-\boldsymbol{r}_j^{(k-1)})^2\right] + \sum_{k=1}^{P}U(\boldsymbol{r}_1^{(k)},\ldots,\boldsymbol{r}_N^{(k)}), \tag{6.8}$$

where $\omega_P = 1/(\beta_P\hbar)$ is the intra-bead vibrational frequency, $\boldsymbol{r}^{(0)} = \boldsymbol{r}^{(P)}$, and $U(\boldsymbol{r}_1,\ldots,\boldsymbol{r}_N)$ is the Born-Oppenheimer PES for the system. To enable direct comparison with the Urey model, the indistinguishability of identical nuclei in the PI calculations is treated in Eq. (6.7) using the classical, rotational symmetry number, σ. However, we note that PI descriptions that explicitly account for nuclear exchange statistics have been previously developed.[41]

6.3 Calculation Details

6.3.a Systems

We perform calculations on four molecules that are of current interest in stable isotope studies: CO_2, N_2O, methane, and propane. In a first application, the enrichment of $^{16}O^{13}C^{18}O$, which dominates the mass-47 experimental signature in clumped isotope studies of CO_2,[5] is investigated using the isotopic-clumping reaction

$$^{16}O^{12}C^{16}O + {}^{16}O^{13}C^{18}O \overset{K}{\rightleftharpoons} {}^{16}O^{13}C^{16}O + {}^{16}O^{12}C^{18}O. \tag{6.9}$$

The equilibrium constant for this reaction is $K = \frac{R_{^{16}O^{12}\to{}^{13}C^{16}O}}{R_{^{16}O^{12}\to{}^{13}C^{18}O}}$, where $R_{^{16}O^{12}\to{}^{13}C^{16}O} = \frac{Q(^{16}O^{13}C^{16}O)}{Q(^{16}O^{12}C^{16}O)}$ and $R_{^{16}O^{12}\to{}^{13}C^{18}O} = \frac{Q(^{16}O^{13}C^{18}O)}{Q(^{16}O^{12}C^{18}O)}$.

In a second application, the enrichment of $^{14}N^{15}N^{16}O$, which is a primary contributor to the overall enrichment of ^{15}N at the central position of N_2O and is thus a potentially useful tool for characterizing origin processes,[4,26] is investigated using the isotopomerization reaction

$$^{14}N^{15}N^{16}O \overset{K}{\rightleftharpoons} {}^{15}N^{14}N^{16}O. \tag{6.10}$$

The equilibrium constant for this reaction is $K = \frac{R_{14\rightarrow 15_N 14_N 16_O}}{R_{14_N 14\rightarrow 15_N 16_O}}$, where $R_{14\rightarrow 15_N 14_N 16_O} = \frac{Q(^{15}N^{14}N^{16}O)}{Q(^{14}N^{14}N^{16}O)}$ and $R_{14_N 14\rightarrow 15_N 16_O} = \frac{Q(^{14}N^{15}N^{16}O)}{Q(^{14}N^{14}N^{16}O)}$.

In a third application, the enrichment of $^{13}CH_3D$, a clumped isotopologue of methane with relevance to isotope studies of natural gas,[23] is investigated using the isotopic-clumping reaction

$$^{12}CH_4 + {}^{13}CH_3D \overset{K}{\rightleftharpoons} {}^{13}CH_4 + {}^{12}CH_3D. \tag{6.11}$$

The equilibrium constant for this reaction is $K = \frac{R_{12\rightarrow 13_{CH_4}}}{R_{12\rightarrow 13_{CH_3D}}}$, where $R_{12\rightarrow 13_{CH_4}} = \frac{Q(^{13}CH_4)}{Q(^{12}CH_4)}$ and $R_{12\rightarrow 13_{CH_3D}} = \frac{Q(^{13}CH_3D)}{Q(^{12}CH_3D)}$.

In a fourth application, the enrichment of $^{12}CH_3{}^{13}CH_2{}^{12}CH_3$, a ^{13}C-substituted isotopomer of propane, is investigated using the isotopomerization reaction

$$^{12}CH_3{}^{13}CH_2{}^{12}CH_3 \overset{K}{\rightleftharpoons} {}^{13}CH_3{}^{12}CH_2{}^{12}CH_3. \tag{6.12}$$

The equilibrium constant for this reaction is $K = \frac{R_{12\rightarrow 13_{C_t}}}{R_{12\rightarrow 13_{C_c}}}$, where $R_{12\rightarrow 13_{C_t}} = \frac{Q(^{13}CH_3{}^{12}CH_2{}^{12}CH_3)}{Q(^{12}CH_3{}^{12}CH_2{}^{12}CH_3)}$ and $R_{12\rightarrow 13_{C_c}} = \frac{Q(^{12}CH_3{}^{13}CH_2{}^{12}CH_3)}{Q(^{12}CH_3{}^{12}CH_2{}^{12}CH_3)}$.

In a final application, the enrichment of $^{12}CH_3{}^{12}CHD{}^{12}CH_3$, a deuterium-substituted isotopomer of propane, is investigated using the isotopomerization reaction

$$^{12}CH_3{}^{12}CHD{}^{12}CH_3 \overset{K}{\rightleftharpoons} {}^{12}CH_2D{}^{12}CH_2{}^{12}CH_3. \tag{6.13}$$

The equilibrium constant for this reaction is $K = \frac{R_{1\rightarrow 2_{H_t}}}{R_{1\rightarrow 2_{H_c}}}$, where $R_{1\rightarrow 2_{H_t}} = \frac{Q(^{12}CH_2D{}^{12}CH_2{}^{12}CH_3)}{Q(^{12}CH_3{}^{12}CH_2{}^{12}CH_3)}$ and $R_{1\rightarrow 2_{H_c}} = \frac{Q(^{12}CH_3{}^{12}CHD{}^{12}CH_3)}{Q(^{12}CH_3{}^{12}CH_2{}^{12}CH_3)}$.

6.3.b Potential Energy Surfaces

The simulations for CO_2 and N_2O use intramolecular PESs from Zúñiga and coworkers[42–44] for which the coefficients of a fourth-order Morse-cosine expansion are determined using spectroscopic data. The simulations for methane utilize a PES computed at the CCSD(T) level of theory.[45,46] The simulations for propane use

the empirical CHARMM PES with general force field parameters;[47] although the propane PES is significantly lower in quality than those used for the other systems, it nonetheless enables us to identify deviations between PI calculations and those based on the Urey model.

6.3.c PI Calculations

PIMC sampling trajectories are performed in Cartesian coordinates with an explicit staging transformation.[48] The staging length, j, is set such that $35-45\%$ of all proposed staging moves are accepted. Prior to any data collection, each sampling trajectory is equilibrated for 10^7 MC steps, with P/j staging moves (rounded up to the nearest integer) attempted per MC step. Thereafter, ring-polymer configurations are sampled every 25 MC steps for the duration of the sampling trajectory, which is sufficient for achieving nearly uncorrelated MC samples. The number of MC steps run for each sampling trajectory is detailed in Table 6.1.

The equilibrium constants and PFRs defined in Eqs. (6.9)-(6.12) are computed at T = 300, 400, 500, and 600 K using the weighted histogram analysis method (WHAM).[49] Each PFR calculation requires several independent sampling trajectories. The ring-polymer potentials employed for these sampling trajectories are identical except for the isotope masses that appear in Eq. (6.8). For each PFR calculation, the independent sampling trajectories employ atomic masses that correspond to the two 'endpoint' isotopologues, as well as fractional atomic masses that lie intermediate to these endpoint isotopologues; the endpoint isotopologues are those that define the PFR. For example, to compute $R_{^{14}\rightarrow{}^{15}\mathrm{N}^{14}\mathrm{N}^{16}\mathrm{O}}$, the different sampling trajectories utilize masses in the ring-polymer potential that are evenly-spaced from ^{14}N to ^{15}N. Nine sampling trajectories are used to compute the PFRs detailed in Eqs. (6.9), (6.10), and (6.13); five sampling trajectories are used to compute the PFRs in Eqs. (6.11) and (6.12). The convergence of the WHAM calculations is tested with multiple sensitivity checks. In particular, the PFR calculations are repeated after removing/adding entire sampling trajectories at some of the intermediate isotope masses to check that the PFRs are converged with respect to the overlap of neighboring probability distributions. Additionally, the PFR calculations are repeated with different histogram resolutions to confirm that the bin sizes do not bias the results.

To ensure that the number of ring-polymer beads is sufficiently large to converge the PI calculations, tests are performed in which the analytical expression for the

primitive PI discretization of the partition function for a simple harmonic oscillator[50] is used to compute PFRs and equilibrium constants. The harmonic oscillator frequencies that are employed in these convergence tests correspond to the normal mode vibrational frequencies for each molecule, and the number of beads, P, that are required to converge the PFRs or equilibrium constants to within a specified tolerance of the exact result is determined. In general, PI calculations of equilibrium constants converge more rapidly than PFRs as a function of P, due to a systematic cancellation of errors in the equilibrium constant calculation. These tests indicate that equilibrium constants can be computed using fewer ring-polymer beads in the following applications, resulting in less statistical variance and computational cost. The bead number for each PIMC sampling trajectory is detailed in Table 6.1.

Two sets of sampling trajectories are employed for calculating the equilibrium constant for the isotopic-clumping reaction for CO_2 (Eq. (6.9)). The first, denoted HB, uses values of P needed to converge the PFRs to within 5×10^{-6}; the second set, denoted LB, uses values of P needed to converge the equilibrium constant to within 10^{-5}. PFR convergence tolerances of 5×10^{-6}, 6×10^{-5}, 10^{-4}, and 4×10^{-3} are used for the PIMC calculations pertaining to Eq. (6.10), Eq. (6.11), Eq. (6.12), and Eq. (6.13), respectively. These parameters are based on the limiting experimental precision of $0.01-0.2‰$ in the measurement of Δ_i.[12,14,18,23]

The Urey-HO calculations employ vibrational frequencies obtained from the PESs described in Section 6.3.b. Anharmonic corrections to the zero-point energy are obtained from the literature[16,32,44] and used to compute Urey-AHO results for CO_2, N_2O, and methane.

Table 6.1: Number of Beads and MC steps for PIMC Simulations.

T (K)	CO_2*		N_2O		Methane		Propane†	
	P	MC steps/10^9	P	MC steps/10^9	P	MC steps/10^9	P	MC steps/10^9
300	720/46	5.0/25.0	720	2.5	128	5.0	90/246	5.0/5.0
400	480/30	5.0/25.0	450	2.5	96	5.0	58/126	5.0/5.0
500	360/22	5.0/25.0	350	2.5	80	5.0	41/78	5.0/5.0
600	290/20	5.0/25.0	250	2.5	70	5.0	32/55	5.0/5.0

* Numbers on the left are for the HB simulations; numbers on the right are for the LB simulations.

† Numbers on the left are for the exchange in Eq. (6.12); numbers on the right are for the exchange in Eq. (6.13).

Table 6.2: Δ_i values for CO_2, N_2O, and methane. Statistical errors for PIMC calculations are in parentheses and apply to the last reported number of the estimate.

T (K)	$\Delta_{^{16}O^{13}C^{18}O}$				$\Delta_{^{14}N^{15}N^{16}O}$			$\Delta_{^{13}CH_3D}$		
	PIMC-HB	PIMC-LB	Urey-HO	Urey-AHO	PIMC	Urey-HO	Urey-AHO	PIMC	Urey-HO	Urey-AHO
300	0.96(8)	0.960(9)	0.938	0.949	22.85(4)	23.42	22.81	5.73(5)	5.71	5.33
400	0.58(5)	0.571(9)	0.556	0.564	15.33(3)	15.77	15.31	3.50(4)	3.46	3.18
500	0.36(4)	0.357(7)	0.350	0.357	11.06(3)	11.47	11.10	2.29(4)	2.23	2.01
600	0.25(6)	0.232(5)	0.228	0.234	8.44(3)	8.74	8.43	1.51(4)	1.50	1.31

6.4 Results

6.4.a Carbon Dioxide, Nitrous Oxide, and Methane

We begin by considering the isotopic enrichment of $^{16}O^{13}C^{18}O$, $^{14}N^{15}N^{16}O$, and $^{13}CH_3D$. Figure 6.1 presents $\Delta_{^{16}O^{13}C^{18}O}$, $\Delta_{^{14}N^{15}N^{16}O}$, and $\Delta_{^{13}CH_3D}$ as functions of temperature, computed with both PIMC and Urey-model calculations; detailed numerical results are reported in Table 6.2. Statistical uncertainties for the PIMC calculations are reported as the standard error of the mean obtained from block-averaging.[51] With the exception of the HB simulations for CO_2, the statistical errors of the PIMC calculations are better than or comparable to the resolving power of analytical instrumentation, demonstrating the capability to precisely determine Δ_i using PI methods.

Figure 6.1 illustrates that the Urey-HO results agree well with PIMC calculations for some of the systems considered, but not for others. For $\Delta_{^{16}O^{13}C^{18}O}$, the results for both the Urey-HO and Urey-AHO methods are in good agreement with the PIMC calculations, with Urey-AHO results deviating from the PIMC calculations by less than $0.01‰$. In contrast, the Urey-HO and Urey-AHO calculations are clearly different for both $\Delta_{^{14}N^{15}N^{16}O}$ and $\Delta_{^{13}CH_3D}$. For $\Delta_{^{14}N^{15}N^{16}O}$, only the Urey-AHO results agree with the PIMC calculations to within statistical error; the Urey-HO results are in error by $0.3 - 0.6‰$. For $\Delta_{^{13}CH_3D}$, the reverse is true; only the Urey-HO results are within statistical error of the PIMC calculations.

The uneven performance of the Urey model can be understood by examining errors in the Urey-HO calculation of the PFRs. For a given PFR, R, the relative error (per mil) in the Urey-HO calculation with respect to the corresponding PIMC calculation is

$$M_R = 1000\left(\frac{R^{(\text{Urey}-\text{HO})}}{R^{(\text{PIMC})}} - 1\right), \tag{6.14}$$

where $R^{(\text{PIMC})}$ and $R^{(\text{Urey}-\text{HO})}$ are the PFRs computed using PIMC and the Urey-HO method, respectively. Figure 6.2 reports this quantity for a variety of PFRs. Interestingly, it is evident from the figure that the predictions for the Urey-HO method have errors that range from $1 - 5‰$. These PFR errors are very large in comparison to the experimental resolution on Δ_i and the statistical uncertainty of the PIMC calculations. For CO_2 and methane, these relatively large PFR errors precisely cancel when calculating the equilibrium constant, giving rise to the agreement between the Urey-HO and PIMC calculations of Δ_i in Figure 6.1. In contrast, the errors for $R_{^{14}\rightarrow^{15}N^{14}N^{16}O}$ and $R_{^{14}N^{14}\rightarrow^{15}N^{16}O}$ differ in magnitude such that the errors only

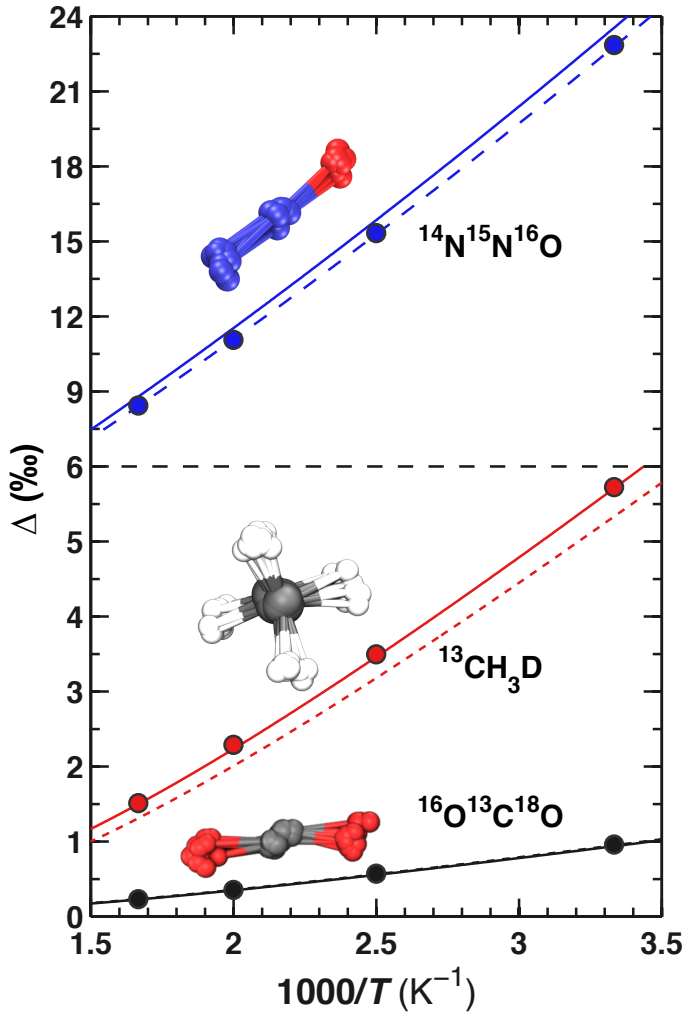

Figure 6.1: $\Delta_{^{16}O^{13}C^{18}O}$, $\Delta_{^{14}N^{15}N^{16}O}$, and $\Delta_{^{13}CH_3D}$ as functions of $1000/T$. PIMC results are indicated by circles; the error bars are smaller than the symbol size. PIMC results for $\Delta_{^{16}O^{13}C^{18}O}$ correspond to the set of calculations that employ a lower number of ring-polymer beads (LB). The solid and dashed lines correspond to the Urey-HO and Urey-AHO results, respectively. Note that the scaling of the y-axis differs above and below $\Delta = 6‰$.

partially cancel when computing the equilibrium constant in Eq. (6.10), resulting in the residual difference between the Urey-HO and PIMC calculations of $\Delta_{^{14}N^{15}N^{16}O}$.

Inaccurate estimates of Δ_i values based on Urey-model calculations result in errors in determination of the apparent equilibrium temperature. Figure 6.3 quantifies these temperature errors by comparing the apparent equilibrium temperature for a given Δ_i, as determined from Urey-model calculations versus the PIMC results. As expected from Figure 6.1, the temperature errors associated with Urey-HO calculations are negligible for $\Delta_{^{13}CH_3D}$ and small for $\Delta_{^{16}O^{13}C^{18}O}$. In contrast, temperature errors as large as 15 K are observed for the Urey-HO calculation of $\Delta_{^{14}N^{15}N^{16}O}$.

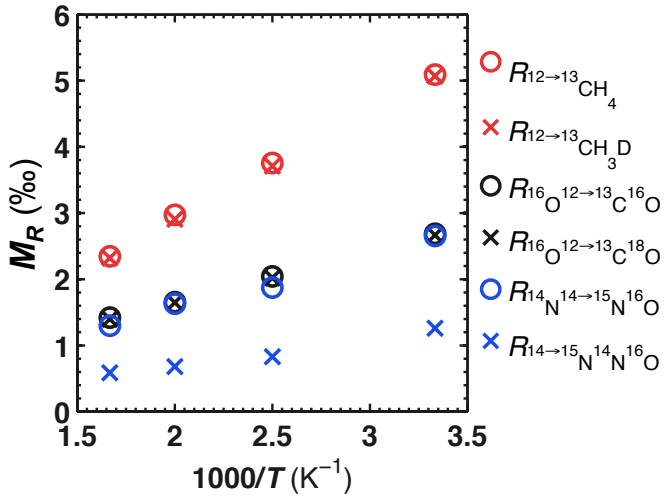

Figure 6.2: The relative error (per mil) of Urey-HO calculations of PFRs for the isotope-exchange reactions given by Eqs. (6.9)-(6.11). The error bars are smaller than the symbol size.

For the Urey-AHO calculations, the predicted values of $\Delta_{^{16}O^{13}C^{18}O}$ and $\Delta_{^{14}N^{15}N^{16}O}$ do not result in statistically significant temperature errors; however, the temperature errors for $\Delta_{^{13}CH_3D}$ are found to be as high as 35 K. We emphasize that the errors for the Urey-HO calculations of $\Delta_{^{14}N^{15}N^{16}O}$ and the Urey-AHO calculations of $\Delta_{^{13}CH_3D}$ are both clearly larger than the statistical error of the PIMC calculations and the associated resolution of experimental measurements.[12,14,23] Taken together, Figures 6.1-6.3 combine to illustrate potential pitfalls of inherent approximations in Urey-model calculations for predicting Δ_i values even in simple molecules, irrespective of whether higher-order corrections are applied.

6.4.b Propane

To test the assumptions of the Urey model in a molecule that exhibits torsional motions, we investigate the isotopic enrichment of the propane isotopologues $^{12}CH_3{}^{12}CHD{}^{12}CH_3$ and $^{12}CH_3{}^{13}CH_2{}^{12}CH_3$. Figure 6.4 presents PIMC and Urey-HO calculations for $\Delta_{^{12}CH_3{}^{13}CH_2{}^{12}CH_3}$ and $\Delta_{^{12}CH_3{}^{12}CHD{}^{12}CH_3}$ as functions of temperature; detailed numerical results are reported in Table 6.3. Statistical uncertainties for the PIMC calculations are again reported as the standard error of the mean obtained from block-averaging. For the $^{12}CH_2D{}^{12}CH_2{}^{12}CH_3$ isotopologue, deuterating the terminal methyl group can result in trans, gauche-plus, and gauche-minus rotamers with respect to the carbon backbone. Although these rotamers have identical equilibrium geometries, the trans and gauche rotamers have different normal vibrational frequencies. Consequently, the reported Urey-HO results for $\Delta_{^{12}CH_3{}^{12}CHD{}^{12}CH_3}$ are

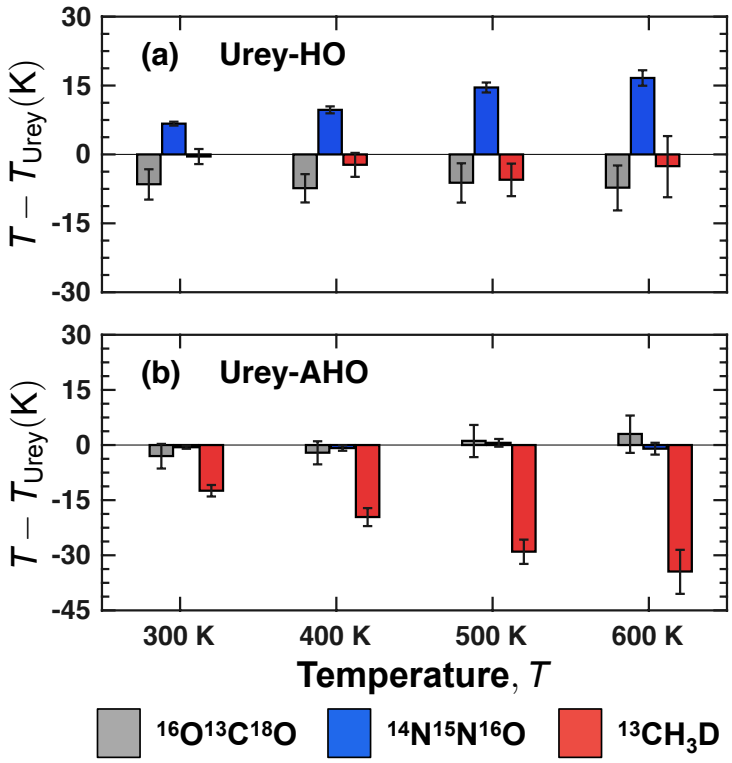

Figure 6.3: Errors in the apparent equilibrium temperature obtained for $\Delta_{^{16}O^{13}C^{18}O}$, $\Delta_{^{14}N^{15}N^{16}O}$, and $\Delta_{^{13}CH_3D}$ using **(a)** Urey-HO calculations and **(b)** Urey-AHO calculations.

obtained by Boltzmann-averaging $R_{1\to 2H_t}$ over these rotamers.[52]

Table 6.3: Δ_i values for propane. Statistical errors are in parentheses and apply to the last digit.

T (K)	$\Delta_{^{12}CH_3{}^{12}CHD{}^{12}CH_3}$		$\Delta_{^{12}CH_3{}^{13}CH_2{}^{12}CH_3}$	
	PIMC	Urey	PIMC	Urey
300	72.1(3)	69.1	9.74(2)	9.58
400	40.5(2)	39.6	5.42(1)	5.29
500	25.4(1)	24.9	3.09(1)	3.07
600	16.7(1)	16.7	1.90(1)	1.84

In Figure 6.4, the Urey-HO results for both $\Delta_{^{12}CH_3{}^{13}CH_2{}^{12}CH_3}$ and $\Delta_{^{12}CH_3{}^{12}CHD{}^{12}CH_3}$ display very little deviation from PIMC for $T \geq 500$ K; however, larger deviations are found at lower temperatures. Figure 6.5 illustrates that the good agreement in Figure 6.4 is once again due to a cancellation of errors during the the Urey-HO calculation of the equilibrium constant. For the calculation of $\Delta_{^{12}CH_3{}^{12}CHD{}^{12}CH_3}$, the errors in $R_{1\to 2H_t}$ and $R_{1\to 2H_c}$ are determined to be nearly 20‰. Nevertheless, the error in the Urey-HO calculation of $\Delta_{^{12}CH_3{}^{12}CHD{}^{12}CH_3}$ is determined to be only as

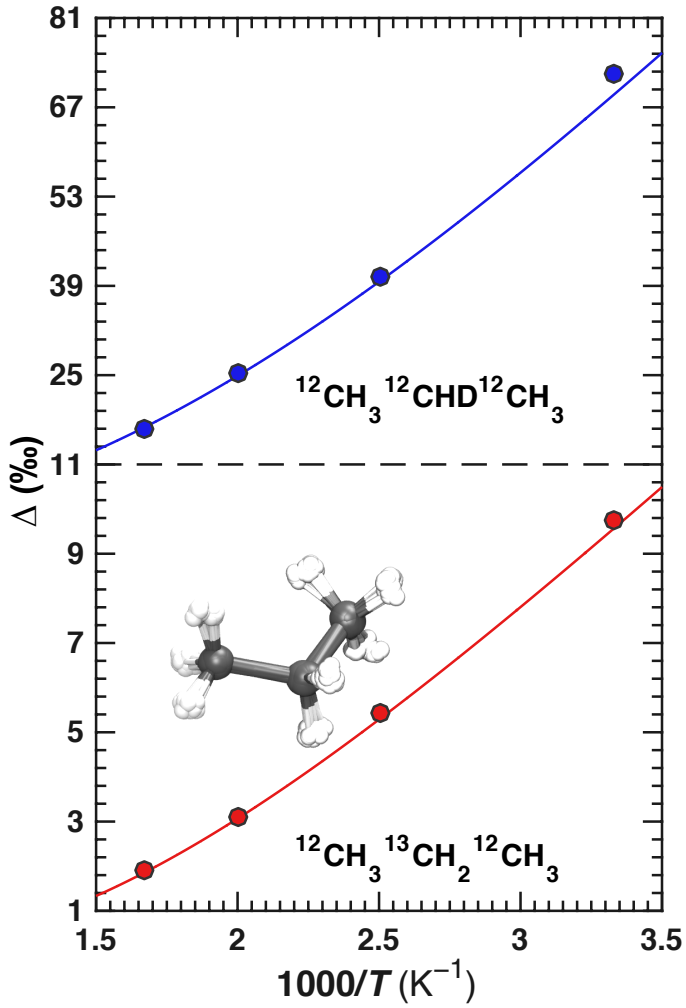

Figure 6.4: $\Delta_{^{12}CH_3{}^{12}CHD{}^{12}CH_3}$ and $\Delta_{^{12}CH_3{}^{13}CH_2{}^{12}CH_3}$ as functions of $1000/T$, with PIMC results given by circles and Urey-HO results given by the solid lines. Note that the scaling of the y-axis differs above and below $\Delta = 11‰$.

large as 2‰, which is smaller than might be anticipated. For $R_{^{12}\rightarrow{}^{13}C_t}$ and $R_{^{12}\rightarrow{}^{13}C_c}$, the associated errors in the Urey-HO model are less than about 2‰, and they too mostly cancel when calculating the equilibrium constant for Eq. (6.12).

Errors in the apparent equilibrium temperature when determined with the Urey model are shown in Figure 6.6. The temperature errors for the Urey-HO calculations of both $\Delta_{^{12}CH_3{}^{13}CH_2{}^{12}CH_3}$ and $\Delta_{^{12}CH_3{}^{12}CHD{}^{12}CH_3}$ are observed to be near to or less than 5 K. This is partially due to the fact that large changes in $\Delta_{^{12}CH_3{}^{13}CH_2{}^{12}CH_3}$ and $\Delta_{^{12}CH_3{}^{12}CHD{}^{12}CH_3}$ correspond to small changes in the apparent equilibrium temperature when the temperature is low. Consequently, the errors in $\Delta_{^{12}CH_3{}^{13}CH_2{}^{12}CH_3}$ and $\Delta_{^{12}CH_3{}^{12}CHD{}^{12}CH_3}$ at low temperatures do not drastically change the apparent equilibrium temperature.

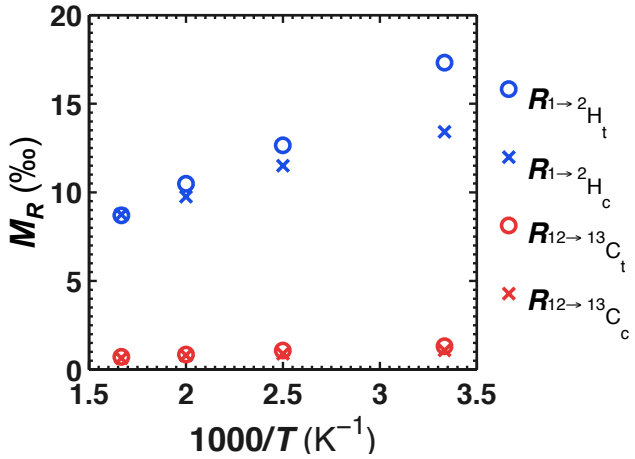

Figure 6.5: The relative error (per mil) of the Urey-HO calculations of PFRs for the isotope-exchange reactions given by Eqs. (6.12) and (6.13). The error bars are smaller than the symbol size.

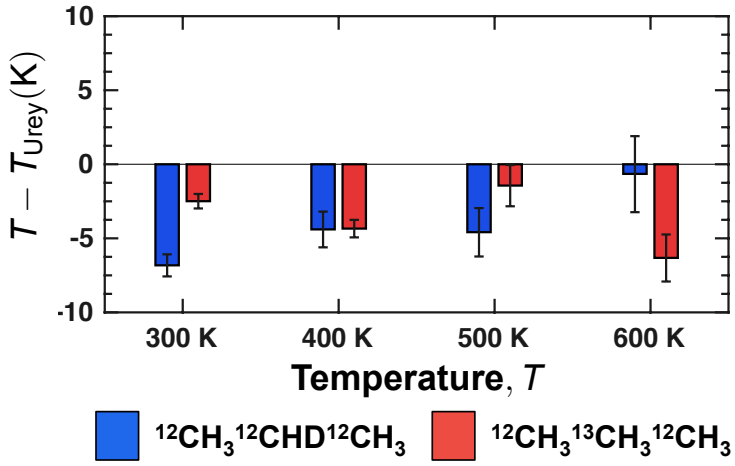

Figure 6.6: Errors in the apparent equilibrium temperature obtained for $\Delta_{^{12}CH_3{}^{12}CHD{}^{12}CH_3}$ and $\Delta_{^{12}CH_3{}^{13}CH_2{}^{12}CH_3}$ using Urey-HO calculations.

6.5 Conclusions

In this work, we utilize path-integral methods to accurately characterize the equilibrium enrichment of certain isotopologues, Δ_i, in four molecules: CO_2, N_2O, methane, and propane. It is shown that PIMC methods combined with high-quality potential energy surfaces enable the determination of Δ_i to the same level of precision as the best analytical instrumentation currently available. These capabilities are used to demonstrate that the Urey-HO model relies upon a substantial cancellation of errors in partition function ratios to calculate Δ_i. Errors in Δ_i are observed when partition function ratio errors do not precisely cancel, as shown for $\Delta_{^{14}N^{15}N^{16}O}$. We additionally find that adopting corrections to the Urey model, such

as including anharmonic contributions to the zero-point energy, does not reliably improve results. Using Urey-model predictions for Δ_i, with or without anharmonic corrections, is found to lead to experimentally resolvable errors in the apparent equilibrium temperature of up to 35 K for the isotopologues studied here. The use of path-integral methods neither relies on any cancellation of errors nor requires any a priori assumptions about the relative importance of effects such as anharmonicity and rovibrational coupling. These results demonstrate that PIMC is an accurate and feasible method for clumped and position-specific isotope analyses, as well as other heavy-atom geochemical applications.

References

(1) Schoell, M *Org Geochem.* **1984**, *6*, 645 –663.

(2) Whiticar, M. J. *Org Geochem.* **1990**, *16*, 531–547.

(3) Conny, J.; Currie, L. *Atmospheric Environment* **1996**, *30*, 621–638.

(4) Stein, L. Y.; Yung, Y. L. *Annual Review of Earth and Planetary Sciences* **2003**, *31*, 329–356.

(5) Affek, H. P.; Eiler, J. M. *Geochim. Cosmochim. Acta* **2006**, *70*, 1–12.

(6) Eiler, J. M. *Earth. Planet. Sci. Lett.* **2007**, *262*, 309–327.

(7) Sturup, S.; Hansen, H. R.; Gammelgaard, B. *Analytical and Bioanalytical Chemistry* **2008**, *390*, 541–554.

(8) Dlugokencky, E. J.; Nisbet, E. G.; Fisher, R; Lowry, D *Philosophical Transactions of the Royal Society A-Mathemtaical Phyiscal and Engineering Sciences* **2011**, *369*, 2058–2072.

(9) Tilley, B; Muehlenbachs, K *Chem. Geol.* **2013**, *339*, 194 –204.

(10) Oba, Y.; Naraoka, H. *Rapid Commun. Mass Spectrom.* **2006**, *20*, 3649–3653.

(11) Mohn, J; Tuzson, B; Manninen, A; Yoshida, N; Toyoda, S; Brand, W. A.; Emmenegger, L *Atmospheric Measurement Techniques* **2012**, *5*, 1601–1609.

(12) Eiler, J. M.; Clog, M.; Magyar, P.; Piasecki, A.; Sessions, A.; Stolper, D.; Deerberg, M.; Schlueter, H.-J.; Schwieters, J. *Int. J. Mass spectrom.* **2013**, *335*, 45 –56.

(13) Well, R; Eschenbach, W; Flessa, H; von der Heide, C; Weymann, D *Geochim. Cosmochim. Acta* **2012**, *90*, 265–282.

(14) Koester, J. R.; Well, R; Tuzson, B; Bol, R; Dittert, K; Giesemann, A; Emmenegger, L; Manninen, A; Cardenas, L; Mohn, J *Rapid Commun. Mass Spectrom.* **2013**, *27*, 216–222.

(15) Eiler, J. M. In *Annual Review of Earth and Planetary Sciences, Vol. 41*, Jeanloz, R, Ed.; Annual Review of Earth and Planetary Sciences, Vol. 41, 2013, 411–441.

(16) Wang, Z. G.; Schauble, E. A.; Eiler, J. M. *Geochim. Cosmochim. Acta* **2004**, *68*, 4779–4797.

(17) Dennis, K. J.; Affek, H. P.; Passey, B. H.; Schrag, D. P.; Eiler, J. M. *Geochim. Cosmochim. Acta* **2011**, *75*, 7117–7131.

(18) Yoshida, N; Vasilev, M; Ghosh, P; Abe, O; Yamada, K; Morimoto, M *Rapid Commun. Mass Spectrom.* **2013**, *27*, 207–215.

(19) Grauel, A.-L.; Schmid, T. W.; Hu, B.; Bergami, C.; Capotondi, L.; Zhou, L.; Bernasconi, S. M. *Geochim. Cosmochim. Acta* **2013**, *108*, 125–140.

(20) Eiler, J. M. *Quaternary Science Reviews* **2011**, *30*, 3575–3588.

(21) Finnegan, S; Bergmann, K; Eiler, J. M.; Jones, D. S.; Fike, D. A.; Eisenman, I; Hughes, N. C.; Tripati, A. K.; Fischer, W. W. *Science* **2011**, *331*, 903–906.

(22) Eagle, R. A.; Tütken, T.; Martin, T. S.; Tripati, A. K.; Fricke, H. C.; Connely, M.; Cifelli, R. L.; Eiler, J. M. *Science* **2011**, *333*, 443–445.

(23) Ma, Q; Wu, S; Tang, Y *Geochim. Cosmochim. Acta* **2008**, *72*, 5446–5456.

(24) Tsuji, K; Teshima, H; Sasada, H; Yoshida, N *Spectrochimica Acta Part A-Molecular and Biomolecular Spectroscopy* **2012**, *98*, 43–46.

(25) Eiler, J. M.; Schauble, E *Geochim. Cosmochim. Acta* **2004**, *68*, 4767–4777.

(26) Toyoda, S; Yano, M; Nishimura, S; Akiyama, H; Hayakawa, A; Koba, K; Sudo, S; Yagi, K; Makabe, A; Tobari, Y; Ogawa, N. O.; Ohkouchi, N; Yamada, K; Yoshida, N *Global Biogeochemical Cycles* **2011**, *25*.

(27) Schauble, E.; Rossman, G.; Taylor, H. *Geochim. Cosmochim. Acta* **2003**, *67*, 3267–3281.

(28) Anbar, A.; Jarzecki, A.; Spiro, T. *Geochim. Cosmochim. Acta* **2005**, *69*, 825–837.

(29) Schauble, E. A.; Ghosh, P; Eiler, J. M. *Geochim. Cosmochim. Acta* **2006**, *70*, 2510–2529.

(30) Guo, W.; Mosenfelder, J. L.; Goddard III, W. A.; Eiler, J. M. *Geochim. Cosmochim. Acta* **2009**, *73*, 7203–7225.

(31) Ni, Y.; Ma, Q.; Ellis, G. S.; Dai, J.; Katz, B.; Zhang, S.; Tang, Y. *Geochim. Cosmochim. Acta* **2011**, *75*, 2696–2707.

(32) Cao, X; Liu, Y *Geochim. Cosmochim. Acta* **2012**, *77*, 292–303.

(33) Urey, H. *J. Chem. Soc.* **1947**, 562–581.

(34) Bigeleisen, J; Mayer, M. *J. Chem. Phys.* **1947**, *15*, 261–267.

(35) Richet, P; Bottinga, Y; Jayvoy, M *Annual Review of Earth and Planetary Sciences* **1977**, *5*, 65–110.

(36) Liu, Q; Tossell, J. A.; Liu, Y *Geochim. Cosmochim. Acta* **2010**, *74*, 6965–6983.

(37) Feynman, R. P.; Hibbs, A. R., *Quantum Mechanics and Path Integrals*; McGraw-Hill Companies: 1965.

(38) McQuarrie, D. A., *Statistical Mechanics*; Univ Science Books: 2000.

(39) Redlich, O *Zeitschrift Fur Physikalische Chemie-Abteilung B-Chemie Der Element Arprozesse Aufbau Der Materie* **1935**, *28*, 371–382.

(40) Barone, V *J. Chem. Phys.* **2004**, *120*, 3059–3065.

(41) Marx, D; Muser, M. *Journal of Physics-Condensed Matter* **1999**, *11*, R117–R155.

(42) Zúñiga, J; Alacid, M; Bastida, A; Carvajal, F. J.; Requena, A *Journal of Molecular Spectroscopy* **1999**, *195*, 137–146.

(43) Zúñiga, J; Alacid, M; Bastida, A; Carvajal, F. J.; Requena, A *J. Chem. Phys.* **1999**, *110*, 6339–6352.

(44) Zúñiga, J; Bastida, A; Requena, A *Journal of Molecular Spectroscopy* **2003**, *217*, 43–58.

(45) Lee, T. J.; Martin, J. M. L.; Taylor, P. R. *J. Chem. Phys.* **1995**, *102*, 254–261.

(46) Dateo, C. E.; Lee, T. J.; Schwenke, D. W. *J. Chem. Phys.* **1994**, *101*, 5853–5859.

(47) Vanommeslaeghe, K; Hatcher, E; Acharya, C; Kundu, S; Zhong, S; Shim, J; Darian, E; Guvench, O; Lopes, P; Vorobyov, I; MacKerell Jr: A. D. *Journal of Computational Chemistry* **2010**, *31*, 671–690.

(48) Tuckerman, M. E.; Berne, B. J.; Martyna, G. J.; Klein, M. L. *J. Chem. Phys.* **1993**, *99*, 2796–2808.

(49) Kumar, S; Bouzida, D; Swendsen, R. H.; Kollman, P. A.; Rosenberg, J. M. *Journal of Computational Chemistry* **1992**, *13*, 1011–1021.

(50) Schweizer, K. S.; Stratt, R. M.; Chandler, D; Wolynes, P. G. *J. Chem. Phys.* **1981**, *75*, 1347–1364.

(51) Frenkel, D.; Smit, B., *Understanding molecular simulation : from algorithms to applications*, 2nd ed.; Academic Press: 2002.

(52) Wang, Y.; Sessions, A. L.; Nielsen, R. J.; Goddard III, W. A. *Geochim. Cosmochim. Acta* **2009**, *73*, 7060–7075.

Chapter 7

EQUILIBRIUM CLUMPED-ISOTOPE EFFECTS IN DOUBLY-SUBSTITUTED ISOTOPOLOGUES OF ETHANE

In Chapter 6, we found that path-integral methods could provide accurate predictions of equilibrium isotopologue enrichment with similar or better precision than analytical instrumentation, while the Urey model exhibited uneven performance even in the simple systems studied. Meanwhile, clumped-isotope analyses are becoming more widespread and sophisticated, such that the analysis of more complex systems is an inevitability. Effects such as anharmonicity are likely to play a greater role in such systems, making path-integral methods a natural choice for theoretical predictions.

In this chapter, we combine path-integral Monte Carlo methods with a new, high-quality intramolecular potential energy surface to quantify the equilibrium enrichment of doubly-substituted ethane isotopologues due to clumped-isotope effects. Ethane represents the simplest molecule to simultaneously exhibit ^{13}C-^{13}C, ^{13}C-D, and D-D clumped-isotope effects, and the analysis of corresponding signatures could be a useful geochemical and biogeochemical proxy to constrain formation temperatures or reaction pathways. By utilizing the path-integral formalism, the calculated enrichment factors provide equilibrium reference values that fully incorporate nuclear quantum effects such as anharmonicity and rotational-vibrational coupling, which are typically neglected by the widely used Urey model. Comparison among the various enrichment factors reveals that thermodynamic enrichment due to isotopic clumping is observed if rare isotope substitutions are separated by three or fewer chemical bonds. We additionally find that the Urey model systematically underestimates enrichment due to ^{13}C-D and D-D clumped-isotope effects in ethane, leading to errors in the apparent equilibrium temperature as large as 30 K at 873.15 K and less severe errors at lower temperatures. Notably, the Urey model ambiguously treats enrichment for isotopologues that have distinct rotamers, whereas the path-integral calculations provide consistent results due to configurational sampling. These findings may have implications in future clumped-isotope studies of more complex systems.

Data and content in this chapter is in preparation as M.A. Webb, Y. Wang, B. Braams, J. Bowman, and T.F. Miller III. “Equilibrium Clumped-Isotope Effects in

Doubly-substituted Isotopologues of Ethane."

7.1 Introduction

The isotopic composition of a material embeds a wealth of information regarding its origin and history.[1–5] Although stable isotope analysis typically focuses on the bulk isotopic composition of materials, which is often dominated by the concentration of molecules containing only one rare isotope, recent advancements in analytical methods enable the explicit and precise measurement of multiply-substituted isotopologues (isotopologues with two or more rare isotope substitutions) at natural abundances.[6–9] The rich diversity of both equilibrium and non-equilibrium fractionation behavior of multiply-substituted isotopologues could help to identify or place additional constraints on formation temperatures, sources, or reaction pathways in a variety of systems.[10]

Most measurements of multiply-substituted isotopologues are of isotopically 'clumped' species, in which rare isotopes are grouped to be nearby in a molecule.[7] At equilibrium, this grouping of rare isotopes leads to relative enrichment of clumped isotopologues compared to what would be expected from stochastic formation from the composite isotopes at natural abundance.[11] Importantly, this enrichment is a direct function of temperature at equilibrium that depends only on the homogeneous isotope exchange among isotopologues and not on external environmental conditions. Therefore, a major application of clumped-isotope measurements is as a paleothermometer based on the extent of ^{13}C-^{18}O ordering in carbonate ions,[12,13] which has been employed to reconstruct ancient marine ocean environments,[14,15] estimate mountain uplift rate,[16] characterize diagenesis,[17] and understand the thermal physiology of extinct vertebrates.[18,19] More applications of clumped-isotope measurements are emerging, as recent studies have demonstrated capabilities to source methane[7,20–23] and to identify biological signatures in molecular oxygen.[24]

A natural extension of existing clumped-isotope applications would be utilization of clumped-isotope signatures in hydrocarbon exploration or stable isotope studies of other forms of organic matter. Carbon and hydrogen isotope ratios have long been used to unravel the complex origins or source processes of samples in geochemistry and biogeochemistry,[1,25–29] and clumped-isotope measurements could add additional constraints and dimensions to their analysis.[4,22,30] Ethane is the simplest molecule that feasibly exhibits ^{13}C-^{13}C, ^{13}C-D, and D-^{12}C-D (henceforth referred to simply as D-D) clumping effects that could be used to probe fractionation history.

Clumping effects in ethane could potentially indicate the balance of thermodynamic and kinetic factors affecting the distribution of isotopes in kerogen, coal, petroleum, and natural gases,[31–33] and may additionally provide insights into the chemistry of more complex organic molecules. Although gas wetness, diffusion, maturation, and degradation are all likely to affect observed experimental signatures, measurements of ^{13}C-D and D-D clumping in methane do indicate isotopic equilibrium or partial equilibrium conditions for a range of natural samples while deviations also provide evidence of kinetically controlled formation pathways.[21–23] Therefore, a natural starting point for ethane is to quantify the enrichment of isotopologues due to isotopic clumping under equilibrium conditions.

In this work, we rigorously and accurately compute equilibrium clumped-isotope effects in ethane using path-integral Monte Carlo methods and a new high-quality, isotopically independent intramolecular potential energy surface. In particular, we compute equilibrium constants for five double-isotope exchange reactions of ethane as functions of temperature. The path-integral calculations are converged to within anticipated experimental precisions of high-resolution mass spectrometry, and comparison among the various equilibrium constants reveals the effect of isotopic clumping on the enrichment of doubly-substituted ethane isotopologues. The results of the path-integral calculations are further compared to those obtained within the harmonic approximation via the widely used Urey model,[34,35] and the size and nature of the errors are discussed.

7.2 Methodology

7.2.a Enrichment of Doubly-Substituted Isotopologues

The relative enrichment of an isotopologue is quantified as

$$\Delta_i = 1000\left[\frac{(x_i/x_0)_{\text{sam}}}{(x_i/x_0)_{\text{r}}} - 1\right], \tag{7.1}$$

where x_i/x_0 is the abundance of an isotopologue, i, relative to that with no rare isotope substitutions, $(\cdots)_{\text{sam}}$ indicates quantities measured for a sample, and $(\cdots)_{\text{r}}$ indicates quantities obtained from the stochastic distribution, in which the composite isotopes are distributed randomly among all isotopologues.[6,7,11] For the special case that the sample is at a thermal equilibrium, Δ_i for a doubly-substituted isotopologue is primarily controlled by isotope exchange reactions of the form

$$\text{XY} + \text{X}'\text{Y}' \overset{K}{\rightleftharpoons} \text{XY}' + \text{X}'\text{Y}, \tag{7.2}$$

where X′ and Y′ are rare isotopes of X and Y, and $K = \frac{Q_{XY'}}{Q_{XY}} \frac{Q_{X'Y}}{Q_{X'Y'}}$ is the equilibrium constant. As shown, the equilibrium constant can be computed from partition functions, denoted by Q, of the various isotopologues in Eq. (7.2). Although there is some variability in the definition of Δ_i,[6,11,22] an approximate relationship between $\Delta_{X'Y'}$ and K can be derived as

$$\Delta_{X'Y'} = 1000\left[1 - \frac{K}{K_r}\right], \tag{7.3}$$

where K_r is the equilibrium constant in Eq. (7.2) for the stochastic distribution of isotopologues.[9,11,36,37] Eq. (7.3) has a leading-order error of $O(\Delta_{X'Y} + \Delta_{XY'})$, which is generally small when there are no structural isotopomers for singly-substituted species[11,36] (as is the case for the specific reactions considered in this study) and will partially cancel with higher order error terms.[37] Eq. (7.3) should in principle account for the indistinguishability of identical nuclei. However, symmetry does not by itself result in thermodynamic isotopic enrichment,[35] and so we instead report thermodynamic enrichment factors

$$\Delta^*_{X'Y'} = 1000(1 - \alpha), \tag{7.4}$$

where $\alpha = K\frac{\sigma_{XY'}\sigma_{X'Y}}{\sigma_{XY}\sigma_{X'Y'}}$ is the fractionation factor with the σ denoting the various symmetry numbers for reactant and product species. Although the equilibrium abundances of all isotopologues can be computed upon consideration of all homogeneous isotope exchange equilibria,[11] we focus on the enrichment of doubly-substituted isotopologues as quantified by the right-hand side of Eq. (7.4).

7.2.b Path Integral Calculations

The Feynman path-integral (PI) formulation of quantum statistical mechanics[38] provides a rigorous framework that has been widely employed to include nuclear quantum effects in the computation of equilibrium isotope effects in many gas-phase and condensed-phase systems.[39–66] Under the PI formalism, the quantum mechanical canonical partition for a system of N distinguishable particles can be expressed as a classical configuration integral,[67,68]

$$Q(N,\beta) = \lim_{P\to\infty} \prod_{i=1}^{N} \left(\frac{m_i P}{2\pi\beta\hbar^2}\right)^{3P/2} \int \prod_{j=1}^{N}\prod_{k=1}^{P} d\boldsymbol{r}_j^{(k)} e^{-\beta_P U_P(\{\boldsymbol{r}_j^{(k)}\})}. \tag{7.5}$$

Through Eq. (7.5), the quantum Boltzmann statistics of the system are obtained from the classical statistics of a ring-polymer with P beads at inverse temperature

$\beta_P = \beta/P$ that interact via an effective potential:

$$U_P(\{\boldsymbol{r}_j^{(k)}\}) = \sum_{j=1}^{N}\sum_{k=1}^{P}\left[\frac{1}{2}m_j\omega_P^2(\boldsymbol{r}_j^{(k)} - \boldsymbol{r}_j^{(k-1)})^2\right] + \sum_{k=1}^{P} U(\boldsymbol{r}_1^{(k)}, \ldots, \boldsymbol{r}_N^{(k)}). \quad (7.6)$$

Here, $\boldsymbol{r}_j^{(k)}$ indicates the position of the jth atom in the kth ring-polymer bead, $\omega_P = 1/(\beta_P\hbar)$ is the intra-bead vibrational frequency, $\boldsymbol{r}^{(0)} = \boldsymbol{r}^{(P)}$, and $U(\boldsymbol{r}_1, \ldots, \boldsymbol{r}_N)$ is the Born-Oppenheimer potential energy surface, or the physical potential, for the system.

There are a variety of path-integral free-energy methods and estimators available for computing isotopic fractionation.[49,50,52,59,61–63,69] Here, we compute the fractionation factors for reactions in the form of Eq. (7.2) as

$$\alpha_{\mathrm{X'Y'}} = \frac{\langle \mathcal{Z}_{\mathrm{X'},\mathrm{X}}\rangle_{\mathrm{X'Y}}}{\langle \mathcal{Z}_{\mathrm{X'},\mathrm{X}}\rangle_{\mathrm{X'Y'}}}, \quad (7.7)$$

where $\langle\cdots\rangle_{\mathrm{X'Y}}$ and $\langle\cdots\rangle_{\mathrm{X'Y'}}$ denote ensemble averages obtained from simulation of X′Y and X′Y′, respectively, and $\mathcal{Z}_{A',A}$ is a direct scaled-coordinates estimator involving the exchange of an isotope A' for that of A.[63] In particular,

$$\mathcal{Z}_{A',A} \equiv \exp\left\{-\beta_P \sum_{k=1}^{P}\left[U(\boldsymbol{q}_1^{(k)}, \ldots, \boldsymbol{q}_N^{(k)}) - U(\boldsymbol{r}_1^{(k)}, \ldots, \boldsymbol{r}_N^{(k)})\right]\right\}, \quad (7.8)$$

is an estimator involving the difference in physical potential between the given ring-polymer configuration and that with scaled-coordinates, $\boldsymbol{q}_j^{(k)} = \bar{\boldsymbol{r}}_j + \sqrt{\frac{m_A}{m_{A'}}}(\boldsymbol{r}_j^{(k)} - \bar{\boldsymbol{r}}_j)$, where $\bar{\boldsymbol{r}}_j = \sum_{k=1}^{P}\boldsymbol{r}_j^{(k)}$ is the position of the ring-polymer centroid for the jth atom, and $m_{A'}$ and m_A are masses of the isotopes A' and A.

We note that Eqs. (7.7) and (7.8) are written such that simulations are performed on isotopologues with more rare isotope substitutions, which should generally lead to smaller statistical errors than performing the opposite substitution.[63] As previously discussed, none of the equations account for the indistinguishability of identical nuclei. However, PI descriptions that explicitly account for nuclear exchange statistics have been previously developed,[70] or symmetry factors might be appropriately used.[50,71]

7.2.c Urey Model

To compare with PI calculations, we also compute equilibrium constants for isotope exchange reactions using the Urey model (or Bigeleisen-Mayer equation).[34,35] Using the rigid-rotor, harmonic-oscillator approximation and the Teller-Redlich product

rule,[71,72] the Urey model provides a convenient way to compute the reduced partition function ratio[37] between two isotopologues as

$$\frac{Q'}{Q} = e^{-\beta[E'^{(0)}-E^{(0)}]} \prod_{i=1}^{N} \left(\frac{m_i'}{m_i}\right)^{3/2} \prod_{j=1}^{\alpha} \frac{\omega'^{(j)}}{\omega^{(j)}} \frac{1-\exp[-\beta\hbar\omega^{(j)}]}{1-\exp[-\beta\hbar\omega'^{(j)}]}, \tag{7.9}$$

where $\beta = 1/(k_B T)$ is the inverse temperature, $E^{(0)}$ is the zero-point energy, m_i is the mass of the ith atom in a molecule of N atoms, $\omega^{(j)}$ is the harmonic frequency of the jth normal mode, and α is the total number of normal vibrational modes ($\alpha = 3N - 5$ for linear molecules and $3N - 6$ for nonlinear molecules). The mass terms precisely cancel in calculating fractionation factors, such that

$$\alpha_{X'Y'} = e^{-\beta\Delta E^{(0)}} \prod_{j=1}^{\alpha} \frac{\omega_{X'Y}^{(j)}\omega_{XY'}^{(j)}}{\omega_{X'Y'}^{(j)}\omega_{XY}^{(j)}} \frac{1-\exp[-\beta\hbar\omega_{XY}^{(j)}]}{1-\exp[-\beta\hbar\omega_{X'Y}^{(j)}]} \frac{1-\exp[-\beta\hbar\omega_{X'Y'}^{(j)}]}{1-\exp[-\beta\hbar\omega_{XY'}^{(j)}]}, \tag{7.10}$$

where $\Delta E^{(0)}$ is the zero-point energy change for Eq. (7.2). If the zero-point energy is calculated purely from harmonic vibrational contributions, i.e., $E_0 = \frac{1}{2}\sum_{j=1}^{\alpha} \hbar\omega_j$ for each isotopologue, then Eq. (7.10) depends only on variation of the harmonic frequencies among the isotopologues.

It is possible to include higher-order, perturbative corrections to Eq. (7.10), such as those due to vibrational anharmonicity, rovibrational coupling, quantum mechanical rotations, and centrifugal distortion.[36,37,73–75] Such corrections may possibly improve and converge calculations of partition function ratios and equilibrium constants.[37,75] However, including only partial corrections to Eq. (7.10) can be detrimental to the overall accuracy of Eq. (7.3) due to a nontrivial cancellation of errors,[62] and the corrections generally require computation of a large number of molecular constants such that they are not easily or widely employed.[37,75] Therefore, we only compare the PI results with those based on the pure rigid-rotor, harmonic oscillator approximation.

7.3 Calculation Details

7.3.a Double Isotope Exchange Reactions in Ethane

Isotopologues featuring two rare isotope substitutions will have the most practical relevance for near-term clumped-isotope studies of ethane.[31–33] To quantify the equilibrium enrichment of doubly-substituted isotopologues and the strength of isotopic clumping, we focus on five isotope-exchange reactions featuring distinct, doubly-substituted ethane isotopologues.

The first reaction is given by

$$^{12}CH_3{}^{12}CH_3 + {}^{13}CH_3{}^{13}CH_3 \overset{\alpha_1}{\rightleftharpoons} 2 \cdot {}^{12}CH_3{}^{13}CH_3. \tag{7.11}$$

The enrichment factor for this reaction is $\alpha_1 = R_{^{12}\rightarrow{}^{13}CH_3{}^{12}CH_3}/R_{^{12}\rightarrow{}^{13}CH_3{}^{13}CH_3}$ where $R_{^{12}CH_3{}^{12}\rightarrow{}^{13}CH_3} = Q_{^{12}CH_3{}^{13}CH_3}/\ Q_{^{12}CH_3{}^{12}CH_3}$ and $R_{^{12}\rightarrow{}^{13}CH_3{}^{13}CH_3} = Q_{^{13}CH_3{}^{13}CH_3}/\ Q_{^{12}CH_3{}^{13}CH_3}$. Eq. (7.11) is expected to dominate the equilibrium signature of the ^{13}C-^{13}C clumped-isotope effect.

The second reaction is given by

$$^{12}CH_3{}^{12}CH_3 + {}^{12}CH_3{}^{13}CH_2D \overset{\alpha_2}{\rightleftharpoons} {}^{12}CH_3{}^{12}CH_2D + {}^{12}CH_3{}^{13}CH_3. \tag{7.12}$$

The enrichment factor for this reaction is $\alpha_2 = R_{^{12}CH_3{}^{12}\rightarrow{}^{13}CH_3}/R_{^{12}CH_3{}^{12}\rightarrow{}^{13}CH_2D}$ where $R_{^{12}CH_3{}^{12}\rightarrow{}^{13}CH_2D} = Q_{^{12}CH_3{}^{13}CH_2D}/Q_{^{12}CH_3{}^{12}CH_2D}$. Eq (7.12) is expected to dominate the signature for the ^{13}C-D clumped-isotope effect.

The third reaction is given by

$$^{12}CH_3{}^{12}CH_3 + {}^{13}CH_3{}^{12}CH_2D \overset{\alpha_3}{\rightleftharpoons} {}^{12}CH_3{}^{12}CH_2D + {}^{12}CH_3{}^{13}CH_3. \tag{7.13}$$

The enrichment factor for this reaction is $\alpha_3 = R_{^{12}CH_3{}^{12}\rightarrow{}^{13}CH_3}/\ R_{^{12}\rightarrow{}^{13}CH_3{}^{12}CH_2D}$ where $R_{^{12}\rightarrow{}^{13}CH_3{}^{12}CH_2D} = Q_{^{13}CH_3{}^{12}CH_2D}/\ Q_{^{12}CH_3{}^{12}CH_2D}$. Eq (7.13) features the same singly-substituted isotopologues as Eq. (7.12), but the two isotope substitutions are separated by an additional bond. Thus, a comparison of the equilibrium constants for Eqs. (7.12) and (7.13) implicitly assesses the strength of the ^{13}C-D clumped-isotope effect.

The fourth reaction is given by

$$^{12}CH_3{}^{12}CH_3 + {}^{12}CH_3{}^{12}CHD_2 \overset{\alpha_4}{\rightleftharpoons} 2 \cdot {}^{12}CH_3{}^{12}CH_2D. \tag{7.14}$$

The enrichment factor for this reaction is $\alpha_4 = R_{^{12}CH_3{}^{12}CH_2(H\rightarrow D)}/\ R_{^{12}CH_3{}^{12}CHD(H\rightarrow D)}$ where $R_{^{12}CH_3{}^{12}CH_2(H\rightarrow D)} = Q_{^{12}CH_3{}^{12}CH_2D}/\ Q_{^{12}CH_3{}^{12}CH_3}$ and $R_{^{12}CH_3{}^{12}CHD(H\rightarrow D)} = Q_{^{12}CH_3{}^{12}CHD_2}/Q_{^{12}CH_3{}^{12}CH_2D}$. Eq. (7.14) is expected to dominate the signature of the D-D clumped-isotope effect.

The fifth reaction is given by

$$^{12}CH_3{}^{12}CH_3 + {}^{12}CH_2D{}^{12}CH_2D \overset{\alpha_5}{\rightleftharpoons} 2 \cdot {}^{12}CH_3{}^{12}CH_2D. \tag{7.15}$$

The enrichment factor for this reaction is $\alpha_5 = R_{^{12}CH_3{}^{12}CH_2(H\rightarrow D)}/\ R_{^{12}CH_2D{}^{12}CHD(H\rightarrow D)}$ where $R_{^{12}CH_2D{}^{12}CHD(H\rightarrow D)} = Q_{^{12}CH_2D{}^{12}CH_2D}/\ Q_{^{12}CH_3{}^{12}CH_2D}$.

Similarly to Eq. (7.13) with respect to Eq. (7.12), Eq. (7.15) features the same singly-substituted isotopologues as Eq. (7.14), and a comparison of equilibrium constants for Eqs. (7.14) and (7.15) implicitly assesses the strength of the D-D clumped-isotope effect.

In Eq. (7.15), the isotopologue $^{12}CH_2D^{12}CH_2D$ has distinct *trans* and *gauche* rotamers (with respect to the positioning of the deuterium atoms) at its minimum energy configuration that exhibit different normal-mode vibrational frequencies and thus different results for Eq. (7.9).[62,76] In this case, the results for the two rotamers are presented separately rather than combined via averaging. In text, the *trans* rotamer will be referred to as *t*-$(CH_2D)_2$ and the *gauche* rotamer as *g*-$(CH_2D)_2$.

7.3.b Potential Energy Surface

All calculations employ a permutationally invariant potential energy surface obtained at the DFT-B3LYP/aug-pVTZ level of theory. The full global PES is expressed as a four-mode multinomial expansion in Morse variables. The coefficients for the expansion are obtained by least-squares fit of energies obtained on a mesh of the internal coordinates. Additional details on the PES will be provided in a future publication.

7.3.c PI Calculations

The enrichment factors for Eqs. (7.11)-(7.15) are computed from $T = 273.15$ K to 873.15 K in increments of 100 K. Each enrichment factor is computed using Eqs. (7.7) and (7.8), where the average scaled-coordinates estimator is obtained from sampling configurations of the heavy isotopologue for each partition function ratio defined in Section 7.3.a using path-integral Monte Carlo (PIMC).

All PIMC sampling trajectories are performed in Cartesian coordinates with an explicit staging transformation.[68] The staging length, j, is set such that 38-42% of all staging moves are accepted for trajectories of $^{12}CH_2D^{12}CH_2D$; that same j is used in simulations of all other isotopologues at a given temperature. Prior to any data collection, each sampling trajectory is equilibrated for 10^6 MC steps, with P/j staging moves (rounded up to the nearest integer) attempted per step. Thereafter, Eq. (7.8) is evaluated from ring-polymer configurations every 10 MC steps. In some cases, isotopologues have multiple equivalent sites for isotope exchange, i.e., $^{12}CH_2D^{12}CH_2D$ going to $^{12}CH_3{}^{12}CH_2D$, in which case Eq. (7.8) is evaluated for both equivalent exchanges at the same ring-polymer configuration. An aggregate total of 2.1×10^8 MC steps are run to compute all estimators at each temperature,

except for estimators associated with Eq. (7.15). For Eq. (7.15), two separate sets of sampling trajectories are run for $^{12}CH_2D^{12}CH_2D$, one set with configurations initialized in approximately *trans* configurations and another with configurations initialized in approximately *gauche* configurations. After this initialization, the rotamers are allowed to interconvert during the sampling trajectories. Estimators for both sets are obtained independently with each set being run for an aggregate total of 4.2×10^8 MC steps. Statistical uncertainties for the PIMC calculations are reported as the standard error of the mean obtained from bootstrap error estimation after partitioning the data into sample points where each sample point is an average of 10^4 estimator values.

To ensure that the PI calculations are sufficiently converged with respect to the number of ring-polymer beads, the equilibrium constant for Eq. (7.14) is computed at $T = 273.15$ K for $P = 8, 16, 32, 64, 96$ and 128. We choose Eq. (7.14) because it involves two H-D exchanges, and tests using the analytical expression for the primitive PI discretization of the partition function for a simple harmonic oscillator[67] suggest that it is the most stringent test for convergence based on differences in harmonic frequencies between reactant and product isotopologues.[62] Figure 7.1 illustrates the convergence of $1000(1 - \alpha_4)$ as a function of P. The figure shows that the results are statistically indistinguishable when using 32 beads compared to using 128 beads. In addition, the calculations are converged within anticipated experimental precisions for D-D clumping of about 1‰, and the calculations are likely even more accurate for the heavier isotope substitutions. Based on these tests, we employ $P = 64$ for all calculations discussed in the remainder of the text.

7.4 Results

We begin by considering the relative enrichment of the doubly-substituted isotopologues of ethane–$^{13}CH_3{}^{13}CH_3$, $^{12}CH_3{}^{13}CH_2D$, $^{13}CH_3{}^{12}CH_2D$, $^{12}CH_3{}^{12}CHD_2$, and $^{12}CH_2D^{12}CH_2D$–as functions of temperature. Figure 7.2 shows the enrichment factors $1000(1 - \alpha_i)$ for the respective double isotope-exchange reactions in Section 7.3.a as predicted by PIMC and the Urey model; detailed numerical comparisons are provided in Table 7.1. The PI calculations are the more rigorous and accurate of the two sets of calculations, and so we first discuss the results in the context of the PI calculations and later consider comparisons with the Urey model.

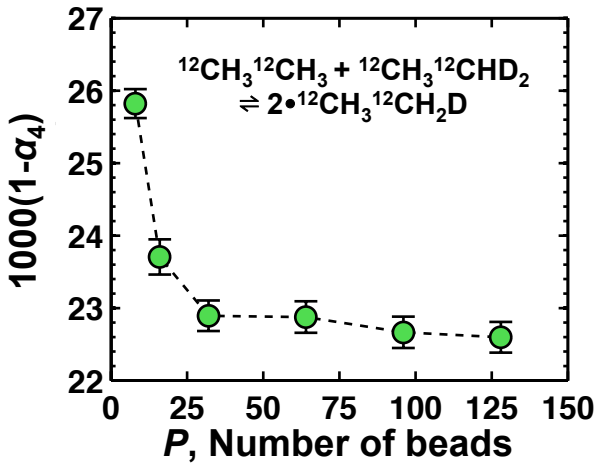

Figure 7.1: Convergence of the enrichment factor for the isotope exchange reaction given by Eq. (7.14) at $T = 273.15$ K as a function of the number of ring-polymer beads, P. Error bars indicate the standard error of the mean obtained from bootstrap error estimation.

Table 7.1: Values of $1000(1-\alpha)$ for $^{13}CH_3{}^{13}CH_3$, $^{12}CH_3{}^{13}CH_2D$, $^{13}CH_3{}^{12}CH_2D$, $^{12}CH_3{}^{12}CHD_2$, and $^{12}CH_2D{}^{12}CH_2D$. Statistical errors for PIMC calculations are in parentheses and apply to the last reported number(s) of the estimate.

T (K)	$^{13}CH_3{}^{13}CH_3$		$^{12}CH_3{}^{13}CH_2D$		$^{13}CH_3{}^{12}CH_2D$	
	PIMC	Urey	PIMC	Urey	PIMC	Urey
273.15	0.29(3)	0.295	6.46(3)	6.288	0.58(3)	0.480
373.15	0.11(2)	0.131	3.85(2)	3.741	0.28(2)	0.212
473.15	0.06(1)	0.064	2.45(1)	2.391	0.12(1)	0.101
573.15	0.039(9)	0.034	1.67(1)	1.593	0.09(1)	0.051
673.15	0.013(7)	0.020	1.148(8)	1.092	0.050(8)	0.027
773.15	0.00(1)	0.012	0.812(6)	0.766	0.022(6)	0.015
873.15	0.008(4)	0.008	0.588(4)	0.548	0.023(4)	0.008
T (K)	$^{12}CH_3{}^{12}CHD_2$		t-$(CH_2D)_2$		g-$(CH_2D)_2$	
	PIMC	Urey	PIMC	Urey	PIMC	Urey
273.15	22.9(2)	22.382	0.68(18)	1.443	0.61(20)	0.078
373.15	11.8(2)	11.335	0.31(13)	0.741	0.37(13)	0.027
473.15	6.4(1)	6.080	0.27(10)	0.394	0.24(10)	0.013
573.15	3.88(9)	3.453	0.18(8)	0.221	0.25(8)	0.006
673.15	2.24(7)	2.068	0.06(6)	0.130	0.04(6)	0.002
773.15	1.43(6)	1.299	−0.01(5)	0.081	0.00(5)	0.000
873.15	0.97(5)	0.850	0.06(4)	0.053	0.00(4)	0.001

Among the isotopologues considered, the enrichment factors most amenable to experimental measurement are those for $^{13}CH_3{}^{13}CH_3$ (gray diamonds), $^{12}CH_3{}^{13}CH_2D$ (blue squares), and possibly $^{12}CH_3{}^{12}CHD_2$ (green circles). Perhaps unsurprisingly,

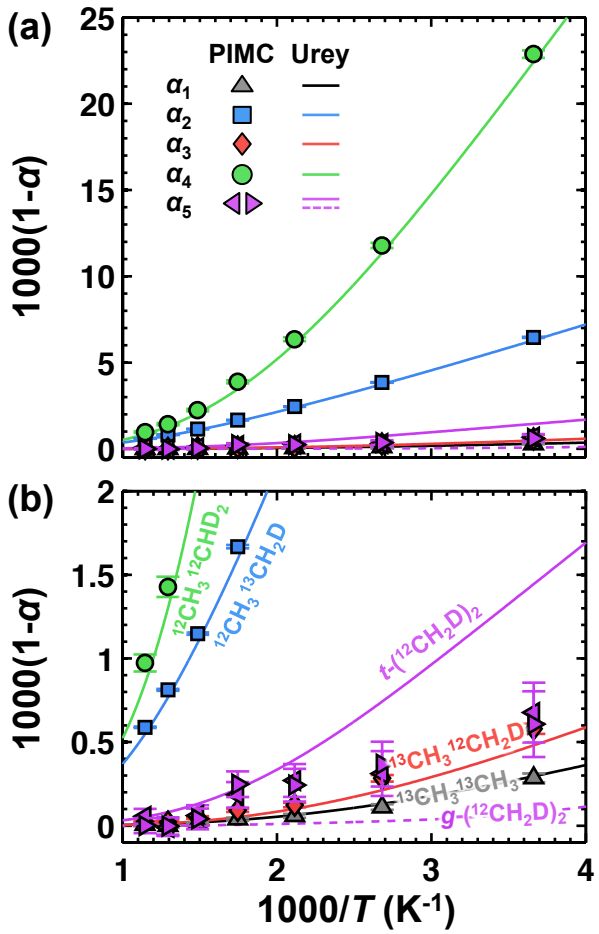

Figure 7.2: Enrichment factors of doubly-substituted isotopologues of ethane given by $1000(1-\alpha_i)$ for Eqs. (7.11)-(7.15) as a function of $1000/T$. Results from PIMC calculations are given by symbols and corresponding Urey-model calculations are given by lines. Panel (b) shows the same data as panel (a) on a different scale. For the results for Eq. (7.15), the solid line and the left-facing triangle indicate results for *t*-$(CH_2D)_2$, for which the deuterium isotopes are in a *trans* conformation; the dashed line and the right-facing triangle indicate results for *g*-$(CH_2D)_2$, for which the deuterium isotopes are in a *gauche* conformation.

Figure 7.2 indicates that the enrichment factors order according to the total relative mass difference of both isotope substitutions. The largest enrichment factor is for the doubly-deuterated $^{12}CH_3{}^{12}CHD_2$ due to the D-D clumping effect, while the the next largest enrichment is due to the ^{13}C-D clumping effect for $^{12}CH_3{}^{13}CH_2D$. At T = 273.15 K, the enrichment factor for $^{12}CH_3{}^{12}CHD_2$ is about 3.5 times larger than that of $^{12}CH_3{}^{13}CH_2D$, which is in turn larger than that of $^{13}CH_3{}^{13}CH_3$ by a factor of nearly 23. To first order, this indicates that the isotope masses are more important than their relative proximity for thermodynamic stability. However, the indirect nature of the D-D coupling in $^{12}CH_3{}^{12}CHD_2$ likely plays some role, as the difference in enrichment factor moving from ^{13}C-D to ^{13}C-^{13}C clumping is larger than from the indirect D-D to ^{13}C-D clumping. Although it is not an ideal comparison, it is interesting to note that the enrichment factor for doubly deuterated molecular hydrogen D_2 at 273.15 K,[34,61] which involves a direct D-D bond, is about 29 times larger than that of $^{12}CH_3{}^{13}CHD_2$ and remarkably similar to what we observe between $^{12}CH_3{}^{13}CHD_2$ and $^{13}CH_3{}^{13}CH_3$.

The enrichment factors for both $^{12}CH_3{}^{12}CHD_2$ and $^{12}CH_3{}^{13}CH_2D$ bear strong resemblance to their their methane analogues, $^{12}CH_2D_2$ and $^{13}CH_3D$.[9,21–23,30,37,62,77] In both cases, the enrichment factors for the ethane isotopologues are slightly smaller than those of the methane isotopologues. We suspect that this behavior will be somewhat general for comparison of enrichment factors across structurally similar molecular species. For comparison between methane and ethane, one of the methyl groups of ethane might be considered as a large pseudo-atom approximately in the position of one of the hydrogen atoms in methane. The ^{13}C-D clumping effect in methane with a large pseudo-atom should be smaller than in regular methane because the isotope substitutions are proportionally smaller perturbations. Likewise, we anticipate that the enrichment factor for $^{12}CH_3{}^{13}CH_2D{}^{12}CH_3$ (the ^{13}C-D clumped-isotope effect at the central position in propane) will be smaller than for $^{12}CH_3{}^{13}CH_2D$. This similarity in equilibrium signatures may be interesting when considering natural gas mixtures and discerning the extent to which two molecular species record different fractionation histories.

As previously noted, another factor influencing the enrichment of doubly-substituted isotopologues is the relative proximity of the two rare isotopes. Figure 7.2B shows that isotope substitution at separate methyl groups results in positive enrichment, but the effect is significantly diminished compared to isotope substitution at the same methyl group. Interestingly, enrichment factors for $^{13}CH_3{}^{13}CH_3$, $^{13}CH_3{}^{12}CH_2D$,

and $^{12}CH_2D^{12}CH_2D$ are all fairly comparable over the entire temperature range despite the variation in the isotope substitutions. This illustrates the competition between mass perturbation and isotope proximity, as the two deuteriums are separated by three bonds, the deuterium and ^{13}C separated by two, and the ^{13}C and ^{13}C directly bonded. It is expected that the clumped-isotope effect will diminish as dual isotope substitution occurs at more distal locations in the molecule, and these results provide a sense for the strength of the coupling between different dual isotope substitutions and how these will affect thermodynamic enrichment in more complex molecules. In particular, enrichment due to deuterium/deuterium substitutions separated by four bonds, deuterium/^{13}C separated by three bonds, or $^{13}C/^{13}C$ by two bonds will be virtually indistinguishable from expectations from the stochastic distribution.

Having examined the general enrichment behavior of the doubly-substituted isotopologues of ethane, we now compare the results of the Urey model to those obtained from PIMC. Figure 7.2 shows that results of the Urey model, without any additional corrections, are generally in good agreement with those obtained from PIMC. The Urey-model results for $^{13}CH_3{}^{13}CH_3$ are statistically indistinguishable from the PIMC calculations. However, there are statistically resolvable errors in the Urey-model results for the enrichment factors of both $^{13}CH_3{}^{12}CH_2D$ and $^{12}CH_2D^{12}CH_2D$. In both cases, the Urey-model predictions are systematically lower over the temperature range studied, with the largest error in the enrichment factor being about 0.5 for $^{12}CH_2D^{12}CH_2D$ at 273.15 K. A recent study on the enrichment of $^{13}CH_3D$ illustrated small systematic errors in the same direction after including various corrections to the Urey model, including an anharmonic correction for zero-point energy, anharmonic correction for vibrational excited states, rotation-vibration coupling correction for zero-point energy, rotation-vibration coupling correction for vibrational excited states, quantum mechanical correction to rotation, and centrifugal distortion correction.[37] Including perturbative corrections to these ethane isotopologues may result in similar convergence behavior with respect to the PIMC calculations.

Although the errors in Figure 7.2 are relatively small, they can manifest as somewhat large deviations in the apparent equilibrium temperature. Figure 7.3 indicates the differences in apparent equilibrium temperatures obtained from the Urey model compared to PIMC for given enrichment factors of $^{13}CH_3{}^{12}CH_2D$ and $^{12}CH_2D^{12}CH_2D$. The data show that temperature errors of about 20-30 K are feasible when using the Urey model for these isotopologues. It is interesting that the largest errors in the apparent equilibrium temperature occur at high temperatures, where the errors

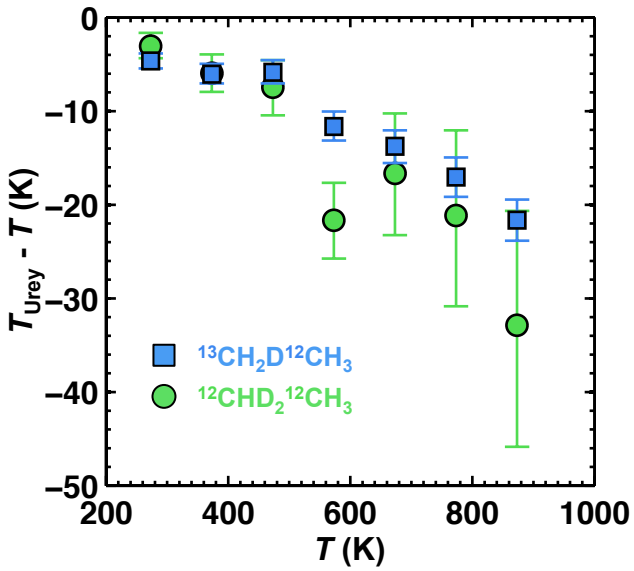

Figure 7.3: Errors in the apparent equilibrium temperature from Urey-model calculations of the enrichment factors for Eqs. (7.12) and (7.14). Taking the PIMC calculations as a reference, temperature errors are computed as the difference in temperature for a given enrichment factor.

in enrichment factors are smallest. On the other hand, such deviations may also be within the uncertainty of experimental measurements. Nonetheless, Figure 7.2 indicates that single-point or two-point temperature calibrations employing the Urey model could lead to unnecessary systematic errors.

In Figure 7.2, the most significant deviations between the Urey-model and PIMC results are for the enrichment factor of $^{12}CH_2D^{12}CH_2D$. As noted earlier, $^{12}CH_2D^{12}CH_2D$ has distinct rotamers, t-$(CH_2D)_2$ and g-$(CH_2D)_2$, with different normal-mode, harmonic frequencies that yield different Urey-model predictions of $1000(1-\alpha)$. This leads to potential ambiguities when considering the actual observed enrichment of the doubly-substituted isotopologue. While it may be possible to compute the partition function using a more sophisticated formalism[78] or obtain estimates based on some averaging scheme, it is appealing that the PIMC calculations do not require exceptional treatments and evidently converge to a common result with sufficient sampling of the proper Boltzmann-weighted ensemble of configurations.

Finally, we note that previous theoretical studies on ethane have determined absolute free-energy errors associated with harmonic approximation of ethane using rigorous PI[41,79] and vibrational configuration interaction approaches.[80] While the Urey model often benefits from a substantial cancellation of errors in its computation

of fractionation factors,[62] the small deviations observed here and in other studies of ethane may manifest as larger errors when considering more complex systems for which anharmonicity and other quantum effects may play a more substantial role.[41,43,47,79]

7.5 Conclusions

In this study, we rigorously compute enrichment factors for all doubly-substituted isotopologues of ethane using path-integral Monte Carlo and a new, high quality potential energy surface. The accuracy and precision of the PIMC calculations are practically converged with consideration of anticipated experimental precisions, and they can be appropriately used as reference data for calibrating experimental measurements or benchmarking other theoretical approaches. By consideration of all the doubly-substituted isotopologues, we quantify the the strength of the clumped-isotope effect, finding that the degree of enrichment decreases in order of deuterium/deuterium, deuterium/^{13}C, and ^{13}C/^{13}C isotope substitutions if the substitutions have similar spatial separation. However, thermodynamic enrichment due to isotopic clumping will be negligible if the isotope substitutions sites are separated by four, three, or two bonds for respectively deuterium/deuterium, deuterium/^{13}C, and ^{13}C/^{13}C dual isotope substitutions. While difficult to interrogate experimentally, these insights may have general implications for modeling behavior in more complex molecules, perhaps obviating the need to examine clumped-isotope behavior beyond a certain distance threshold. Finally, we find that Urey-model predictions for ^{13}C-^{13}C clumping are statistically indistinguishable from the PIMC calculations, but results for $^{12}CH_3{}^{13}CH_2D$ and $^{12}CH_3{}^{12}CHD_2$ systematically underestimate the enrichment. This underestimation leads to errors in the apparent equilibrium temperature as large as 30 K at higher formation temperatures. In addition, comparing the two methods reveals an inherent issue with the Urey model in predicting enrichment for isotopologues with rotamers. Whereas the PIMC calculations converge to a single result for $^{12}CH_2D{}^{12}CH_2D$, the Urey model provides distinct results for *t*-$(CH_2D)_2$ and *g*-$(CH_2D)_2$ rotamers, leading to ambiguity in predicting the relative enrichment of $^{12}CH_2D{}^{12}CH_2D$. While ethane is a simple molecule, this issue requires careful consideration for isotope studies of more complex systems, but PI methods are a tractable way forward.

References

(1) Schoell, M *Org Geochem.* **1984**, *6*, 645 –663.

(2) Whiticar, M. J. *Org Geochem.* **1990**, *16*, 531–547.

(3) Sturup, S.; Hansen, H. R.; Gammelgaard, B. *Analytical and Bioanalytical Chemistry* **2008**, *390*, 541–554.

(4) Eiler, J. M. In *Annual Review of Earth and Planetary Sciences, Vol. 41*, Jeanloz, R, Ed.; Annual Review of Earth and Planetary Sciences, Vol. 41, 2013, 411–441.

(5) Wolfsberg, M.; Hook, W. A.; Paneth, P.; Rebelo, L. P. N., *Isotope Effects in the Chemical, Geological and Bio Sciences*; Springer Netherlands.

(6) Affek, H. P.; Eiler, J. M. *Geochim. Cosmochim. Acta* **2006**, *70*, 1–12.

(7) Eiler, J. M. *Earth. Planet. Sci. Lett.* **2007**, *262*, 309–327.

(8) Dennis, K. J.; Affek, H. P.; Passey, B. H.; Schrag, D. P.; Eiler, J. M. *Geochim. Cosmochim. Acta* **2011**, *75*, 7117–7131.

(9) Ono, S.; Wang, D. T.; Gruen, D. S.; Lollar, B. S.; Zahniser, M. S.; McManus, B. J.; Nelson, D. D. *Anal. Chem.* **2014**, *86*, 6487–6494.

(10) Eiler, J. M.; Bergquist, B.; Bourg, I.; Cartigny, P.; Farquhar, J.; Gagnon, A.; Guo, W.; Halevy, I.; Hofmann, A.; Larson, T. E.; Levin, N.; Schauble, E. A.; Stolper, D. *Chem. Geol.* **2014**, *372*, 119 –143.

(11) Wang, Z. G.; Schauble, E. A.; Eiler, J. M. *Geochim. Cosmochim. Acta* **2004**, *68*, 4779–4797.

(12) Ghosh, P; Adkins, J; Affek, H; Balta, B; Guo, W.; Schauble, E.; Schrag, D; Eller, J. *GEOCHIMICA ET COSMOCHIMICA ACTA* **2006**, *70*, 1439–1456.

(13) Eiler, J. M. *Quaternary Science Reviews* **2011**, *30*, 3575–3588.

(14) Finnegan, S; Bergmann, K; Eiler, J. M.; Jones, D. S.; Fike, D. A.; Eisenman, I; Hughes, N. C.; Tripati, A. K.; Fischer, W. W. *Science* **2011**, *331*, 903–906.

(15) Grauel, A.-L.; Schmid, T. W.; Hu, B.; Bergami, C.; Capotondi, L.; Zhou, L.; Bernasconi, S. M. *Geochim. Cosmochim. Acta* **2013**, *108*, 125–140.

(16) Ghosh, P.; Garzione, C. N.; Eiler, J. M. *Science* **2006**, *311*, 511–515.

(17) Huntington, K. W.; Budd, D. A.; Wernicke, B. P.; Eiler, J. M. *Journal Of Sedimentary Research* **2011**, *81*, 656–669.

(18) Eagle, R. A.; Schauble, E. A.; Tripati, A. K.; Tütken, T.; Hulbert, R. C.; Eiler, J. M. *Proceedings of the National Academy of Sciences* **2010**, *107*, 10377–10382.

(19) Eagle, R. A.; Tütken, T.; Martin, T. S.; Tripati, A. K.; Fricke, H. C.; Connely, M.; Cifelli, R. L.; Eiler, J. M. *Science* **2011**, *333*, 443–445.

(20) Mroz, E. J. *Chemosphere* **1993**, *26*, 45–53.

(21) Stolper, D. A.; Lawson, M.; Davis, C. L.; Ferreira, A. A.; Neto, E. V. S.; Ellis, G. S.; Lewan, M. D.; Martini, A. M.; Tang, Y.; Schoell, M.; Sessions, A. L.; Eiler, J. M. *Science* **2014**, *344*, 1500–1503.

(22) Stolper, D.; Sessions, A.; Ferreira, A.; Neto, E. S.; Schimmelmann, A.; Shusta, S.; Valentine, D.; Eiler, J. *Geochim. Cosmochim. Acta* **2014**, *126*, 169 –191.

(23) Stolper, D.; Martini, A.; Clog, M.; Douglas, P.; Shusta, S.; Valentine, D.; Sessions, A.; Eiler, J. *Geochim. Cosmochim. Acta* **2015**, *161*, 219 –247.

(24) Yeung, L. Y.; Ash, J. L.; Young, E. D. *Science* **2015**, *348*, 431–434.

(25) Craig, H. *Geochim. Cosmochim. Acta* **1953**, *3*, 53 –92.

(26) Freeman, KH and Hayes, JM and Trendel, JM and Albrecht, P *Nature* **1990**, *343*, 254–256.

(27) Hayes, J.; Freeman, K. H.; Popp, B. N.; Hoham, C. H. *Org Geochem.* **1990**, *16*, 1115 –1128.

(28) Clayton, C. *Marine and Petroleum Geology* **1991**, *8*, 232 –240.

(29) Sessions, A. L.; Burgoyne, T. W.; Schimmelmann, A.; Hayes, J. M. *Org Geochem.* **1999**, *30*, 1193 –1200.

(30) Ma, Q; Wu, S; Tang, Y *Geochim. Cosmochim. Acta* **2008**, *72*, 5446–5456.

(31) Clog, M.; Ling, C.; Eiler, J. M. *AGU Fall Meeting Abstracts* **2012**.

(32) Clog, M. D.; Eiler, J. M. *AGU Fall Meeting Abstracts* **2014**.

(33) Clog, M. D.; Ferreira, A. A.; Santos Neto, E. V.; Eiler, J. M. *AGU Fall Meeting Abstracts* **2014**.

(34) Urey, H. *J. Chem. Soc.* **1947**, 562–581.

(35) Bigeleisen, J; Mayer, M. *J. Chem. Phys.* **1947**, *15*, 261–267.

(36) Cao, X; Liu, Y *Geochim. Cosmochim. Acta* **2012**, *77*, 292–303.

(37) Liu, Q.; Liu, Y. *Geochim. Cosmochim. Acta* **2016**, *175*, 252 –270.

(38) Feynman, R. P.; Hibbs, A. R., *Quantum Mechanics and Path Integrals*; McGraw-Hill Companies: 1965.

(39) Balog, E; Hughes, A. L.; Martyna, G. J. *J. Chem. Phys.* **2000**, *112*, 870–880.

(40) Bohm, M.; Schulte, J; Hernandez, E; Ramirez, R *Chemical Physics* **2001**, *264*, 371–400.

(41) Miller, T. F.; Clary, D. C. *J. Chem. Phys.* **2002**, *116*, 8262–8269.

(42) Chen, B; Ivanov, I; Klein, M.; Parrinello, M *Physical Review Letters* **2003**, *91*.

(43) Miller, T.; Clary, D. *Physical Chemistry Chemical Physics* **2004**, *6*, 2563–2571.

(44) Lynch, V. A.; Mielke, S. L.; Truhlar, D. G. *J. Chem. Phys.* **2004**, *121*, 5148–5162.

(45) De la Peña, L.; Kusalik, P. *JOURNAL OF CHEMICAL PHYSICS* **2004**, *121*, 5992–6002.

(46) Lynch, V. A.; Mielke, S. L.; Truhlar, D. G. *Journal of Physical Chemistry A* **2005**, *109*, 10092–10099.

(47) Miller, T.; Clary, D. *Journal of Physical Chemistry A* **2006**, *110*, 731–740.

(48) Paesani, F.; Iuchi, S.; Voth, G. A. *J. Chem. Phys.* **2007**, *127*.

(49) Mielke, S. L.; Truhlar, D. G. *Journal of Physical Chemistry A* **2009**, *113*, 4817–4827.

(50) Zimmermann, T; Vaníček, J *J. Chem. Phys.* **2009**, *131*.

(51) Habershon, S; Manolopoulos, D. E. *J. Chem. Phys.* **2011**, *135* 224111, 224111.

(52) Azuri, A; Engel, H; Doron, D; Major, D. T. *Journal of Chemical Theory and Computation* **2011**, *7*, 1273–1286.

(53) Pérez, A.; von Lilienfeld, O. A. *Journal of Chemical Theory and Computation* **2011**, *7*, 2358–2369.

(54) Herrero, C.; Ramirez, R *J. Chem. Phys.* **2011**, *134*.

(55) Mielke, S. L.; Truhlar, D. G. *Journal of Chemical Theory and Computation* **2012**, *8*, 1589–1596.

(56) Buchowiecki, M *Chemical Physics Letters* **2012**, *531*, 202–205.

(57) Markland, T. E.; Berne, B. J. *Proceedings of the National Academy of Sciences of the United States of America* **2012**, *109*, 7988–7991.

(58) Liu, J.; Andino, R. S.; Miller, C. M.; Chen, X.; Wilkins, D. M.; Ceriotti, M.; Manolopoulos, D. E. *Journal of Physical Chemistry C* **2013**, *117*, 2944–2951.

(59) Ceriotti, M; Markland, T. E. *J. Chem. Phys.* **2013**, *138*.

(60) Mielke, S. L.; Dinpajooh, M; Siepmann, J. I.; Truhlar, D. G. *J. Chem. Phys.* **2013**, *138* 014110, 014110.

(61) Buchowiecki, M.; Vaníček, J. *Chemical Physics Letters* **2013**, *588*, 11 –16.

(62) Webb, M. A.; Thomas F. Miller, I. *J.urnal of Physical Chemistry A* **2014**, *118*, 467–474.

(63) Cheng, B.; Ceriotti, M. *J. Chem. Phys.* **2014**, *141* 244112.

(64) Pinilla, C.; Blanchard, M.; Balan, E.; Ferlat, G.; Vuilleumier, R.; Mauri, F. *GEOCHIMICA ET COSMOCHIMICA ACTA* **2014**, *135*, 203–216.

(65) Buchowiecki, M. *Chemical Physics Letters* **2015**, *635*, 196 –200.

(66) Buchowiecki, M. *Chemical Physics Letters* **2016**, *652*, 32 –35.

(67) Schweizer, K. S.; Stratt, R. M.; Chandler, D; Wolynes, P. G. *J. Chem. Phys.* **1981**, *75*, 1347–1364.

(68) Tuckerman, M. E., *Statistical Mechanics: Theory and Molecular Simulation (Oxford Graduate Texts)*; Oxford University Press, USA: 2010.

(69) Marsalek, O.; Chen, P.-Y.; Dupuis, R.; Benoit, M.; Méheut, M.; Bačić, Z.; Tuckerman, M. E. *Journal of Chemical Theory and Computation* **2014**, *10*, 1440–1453.

(70) Marx, D; Muser, M. *Journal of Physics-Condensed Matter* **1999**, *11*, R117–R155.

(71) McQuarrie, D. A., *Statistical Mechanics*; Univ Science Books: 2000.

(72) Redlich, O *Zeitschrift Fur Physikalische Chemie-Abteilung B-Chemie Der Element Arprozesse Aufbau Der Materie* **1935**, *28*, 371–382.

(73) Richet, P; Bottinga, Y; Jayvoy, M *Annual Review of Earth and Planetary Sciences* **1977**, *5*, 65–110.

(74) Barone, V *J. Chem. Phys.* **2004**, *120*, 3059–3065.

(75) Liu, Q; Tossell, J. A.; Liu, Y *Geochim. Cosmochim. Acta* **2010**, *74*, 6965–6983.

(76) Wang, Y.; Sessions, A. L.; Nielsen, R. J.; Goddard III, W. A. *Geochim. Cosmochim. Acta* **2009**, *73*, 7060–7075.

(77) Wang, D. T. et al. *Science* **2015**, *348*, 428–431.

(78) Truhlar, D. G. *Journal of Computational Chemistry* **1991**, *12*, 266–270.

(79) Miller, T. F.; Clary, D. C. *J. Chem. Phys.* **2003**, *119*, 68–76.

(80) Chakraborty, A; Truhlar, D. G. *J. Chem. Phys.* **2006**, *124* 184310, 184310.